Periodic Travelling Wave Photodetectors with Serial and Parallel Optical Feed Based on InP

vorgelegt von
Diplom-Physiker
Andreas Beling
aus Bonn

Von der Fakultät IV - Elektrotechnik und Informatik
der Technischen Universität Berlin
zur Erlangung des akademischen Grades
Doktor der Ingenieurwissenschaften
- Dr.-Ing. -
genehmigte Dissertation

Promotionsausschuss:
Vorsitzender: Prof. Dr.-Ing. H. Henke
1. Gutachter: Prof. Dr.-Ing. K. Petermann
2. Gutachter: Prof. Dr. D. Jäger
Tag der wissenschaftlichen Aussprache: 24.11.2006

Berlin 2006
D83

Zusammenfassung

In der vorliegenden Arbeit werden monolithisch integrierte periodische Wanderwellen-Photodetektoren mit paralleler und serieller optischer Speisung für Hochgeschwindigkeits- und Hochstrom-Anwendungen bei $1.55\,\mu m$ Wellenlänge entwickelt und charakterisiert.

Die untersuchten Photodetektoren basieren auf diskreten, miniaturisierten evaneszent-gekoppelten p-i-n Photodioden, die durch eine Koplanarleitung verschaltet sind und somit eine Wanderwellenstruktur ausbilden. Im Gegensatz zu einzelnen, diskreten ("lumped element") Photodetektoren lassen sich Wanderwellen-Photodetektoren in der elektrischen Domäne als kapazitiv-belastete Leitungen oder generell als verteilte Strukturen beschreiben. Dadurch sind sie nicht an die RC-Bandbreite-Limitierung gebunden und der inhärente Kompromiß zwischen maximierter Photodiodengröße und minimierter RC-Konstante kann überwunden werden. Durch ein geeignetes Design der Koplanarleitung kann die Impedanz des Wanderwellen-Photodetektors an die der Last angepaßt werden. Liegt außerdem eine Phasenanpassung zwischen dem optischen und elektrischen Signal vor, verbleibt als Bandbreite-Begrenzung lediglich die Ladungsträgertransitzeit und das Bragg-Limit.

In Bezug auf die optische Speisung werden zwei unterschiedliche Konzepte untersucht: Im Falle der parallelen optischen Speisung wird das optische Eingangssignal in einem verlustarmen monolithisch integrierten Multimoden-Interferenz-Teiler gleichmäßig auf mehrere Photodioden aufgeteilt. Dieser Typ des Wanderwellen-Photodetektors zeichnet sich insbesondere durch seine Fähigkeit aus, auch Signale hoher optischer Leistung opto-elektronisch zu wandeln.

Der Wanderwellen-Photodetektor mit serieller optischer Speisung besteht aus einem Zuführungswellenleiter, auf dem die Photodioden hintereinander angeordnet sind. Verglichen mit einer Einzel-Photodiode läßt sich mit diesem Konzept eine gesteigerte Responsivität bei Erhaltung der Bandbreite erreichen.

Die theoretische Betrachtungen der optischen und elektrischen Eigenschaften des Wanderwellen-Photodetektors führen im Bauelementeentwurf auf ein Design, welches Impedanz- und Phasenanpassung sowie eine ausreichend hohe Bragg-Frequenz gewährleistet. Durch den Einsatz von kurzen, vielmodigen Wellenleitern im optischen Design

kann der Quantenwirkungsgrad aller betrachteten Photodetektoren gesteigert werden. Ausgehend von einem bewährten epitaktischen Schichtendesign werden erstmals Wanderwellen-Photodetektoren mit neuen Schichtenstrukturen erprobt, u.a. auch eine "dual-depleted" Struktur, welche zu kürzeren Ladungsträgertransitzeiten bzw. reduzierter pn-Kapazität führt.
Die experimentell gewonnenen Ergebnisse zeigen, daß die hergestellten Wanderwellenphotodetektoren in zwei wichtigen Parametern, der exzellenten elektrischen Impedanzanpassung an $50\,\Omega$ über einen weiten Frequenzbereich und der maximalen elektrischen Ausgangsleistung, den diskreten Photodetektoren überlegen sind. Die Bandbreiten erreichen dabei erstmalig auch im Falle des parallel-gespeisten Wanderwellen-Photodetektors Werte um $85\,GHz$ bei Responsivitäten bis $0.45\,A/W$. Insbesondere bei hohen optischen Leistungen und Signalfrequenzen im Bereich $100\,GHz$ bis $400\,GHz$ zeigt der Wanderwellen-Photodetektor deutlich bessere Frequenzgangseigenschaften als vergleichbare diskrete Detektoren. Eingesetzt als effizienter Photomischer erschließt sich dem periodischen Wanderwellen-Photodetektor damit ein neues Anwendungsgebiet bis in den Terahertz-Bereich. Hinzu kommen die vorteilhaften Eigenschaften der Pulsantwort, die sich sowohl in einer kleinen Halbwertsbreite als auch in einem vernachlässigbar kleinen Nachschwingen manifestieren. Abschließende Experimente demonstrieren die Systemtauglichkeit des Wanderwellen-Photodetektors erstmalig für Bitraten $> 80\,Gbit/s$.

Abstract

In this work, monolithically integrated, periodic travelling wave photodetectors with parallel and serial optical feed for high-speed and high-power applications at $1.55\,\mu m$ wavelength are developed and characterized.

The studied photodetectors are based on discrete, miniaturized evanescently coupled p-i-n photodiodes, which are distributed along a coplanar waveguide and thus form a travelling wave structure. In contrast to lumped element photodetectors, the travelling wave photodetector can be described in the electrical domain as a capacitively-loaded transmission line, or generally, as a fully distributed structure. Hence, the bandwidth is not bound by the overall RC-constant and the trade-off between maximized absorber area and RC-limited bandwidth can be overcome. By an appropriate design of the transmission line the characteristic impedance of the entire device can be matched to that of the external load. Assuming a phase match between the optical and electrical signals, the bandwidth is limited by the carrier transit times and Bragg-limit only.

In the thesis two types of optical feeding are studied. The parallel-fed travelling wave photodetector comprises a monolithically integrated low-loss multimode interference power splitter of which output waveguides feed the discrete photodiodes symmetrically. With this design, the maximum electrical output power can be significantly enhanced when compared to a single photodiode.

In the case of the serial optical feeding the photodiodes are arranged in series on top of one single waveguide. Here, the overall quantum efficiency ideally exceeds the one of a single photodiode at maintained bandwidth.

The theoretical investigations of the optical and electrical properties lead to a device design, which exhibits impedance and phase match, as well as a Bragg-limit at a sufficiently high frequency. By employing short multimode waveguides in the optical design, the quantum efficiency can be enhanced for all considered types of photodetectors.

Based on an established epitaxial layer stack, travelling wave photodetectors with novel layer structures, including a dual depleted structure, are evaluated in order to achieve shorter carrier transit times and a reduced pn-capacitance.

The experimental results reveal superior performance in terms of the broadband electrical impedance match and the maximum output power, when compared to lumped element photodetectors. For the first time, the bandwidth of the parallel-fed travelling wave photodetector reaches $85\,GHz$ with a responsivity of $0.45\,A/W$. In particular at high optical input powers and frequencies above $100\,GHz$, the travelling wave photodetector clearly outperforms comparable lumped element detectors, which additionally recommends the device as an efficient photomixer up to THz-frequencies. Finally, system tests demonstrate the suitability of the travelling wave photodetector for the use in optical frontends at bitrates in excess of $80\,Gbit/s$.

Contents

1. Introduction **9**

2. High-speed photodetectors **11**

2.1. The p-i-n photodiode 11

2.2. Photodetector structures 18

3. Travelling wave photodetector theory and design **23**

3.1. Principle of operation and integration concept 23

3.2. Discrete miniaturized waveguide-integrated photodiode 25

3.2.1. Simulation of the transfer function 25

3.2.2. Optical simulation 34

3.2.3. Photodiode optimization, design and characteristics 42

3.3. Capacitively-loaded coplanar transmission line 49

3.4. Phase mismatch of periodic TWPD 57

3.5. Parallel optical feed 61

3.6. Serial optical feed 65

3.7. Equivalent circuit 69

3.8. Summary 75

4. Device design and fabrication **77**

4.1. Device layout and epitaxial layer structure 77

4.2. Fabrication process 80

5. Device characterization **84**

5.1. Current-voltage, responsivity and PDL 84

5.2. Determination of the optical group velocity 89

5.3. C-V measurements 92

5.4. S-parameters 93

5.4.1. Transmission line properties 93

5.4.2. One-port measurements 96

5.5. O/E heterodyne measurements 102

5.5.1. Experimental setup . . . 102
5.5.2. Experimental results . . . 103
5.6. Pulse measurements . . . 112
5.6.1. Electrical sampling setup . . . 112
5.6.2. Experimental results . . . 113
5.7. High-power saturation effects . . . 114
5.7.1. Frequency domain . . . 114
5.7.2. Time domain . . . 118
5.8. Chip packaging and system tests . . . 120

6. Conclusion **125**

7. Appendix **129**
7.1. Epitaxial layer stack . . . 129
7.2. Two-layered coplanar waveguide . . . 130
7.3. Derivation of the Bragg-frequency f_{bragg} . . . 131
7.4. Transmission matrix of a lossy transmission line . . . 134
7.5. Process steps . . . 136
7.6. Optical heterodyne microwave generation . . . 138
7.7. List of symbols . . . 140
7.8. List of abbreviations . . . 144

8. References **147**

A. List of publications **158**

B. Danksagung **161**

1. Introduction

Over the years the demand in the speed and capacity of telecommunication systems has been increasing due to the massive growth in internet usage. Optical networks will be employed to cope with a high capacity of data transmission. In optical fibre-based transmission systems, aggregated bit rates with Tera-bits/s have been demonstrated by using wavelength division multiplexing (WDM) and time division multiplexing (TDM) techniques with single channel bit rates up to 160 Gb/s [1, 2, 3, 4]. These ultra fast communication links require photodetectors, which convert the modulated light signal to an electrical current at high modulation frequencies in excess of 100 GHz. High-speed photodetectors with high quantum efficiency and high-power handling capability are key elements in these systems. Employed in a digital optical frontend they are required to provide a distortion-free electrical output signal with high sensitivity over a large dynamic range and make electrical post-amplification redundant. Apart from a large bandwidth-efficiency product, an excellent pulse response revealed by a short pulse width and small ringing, low polarization dependence and high electrical return loss are significant standards when evaluating photodetectors for high bit-rate systems. Another recent application of high performance opto-electronic (O/E) converters is the generation of mm and submm-waves by photomixing. Here a large bandwidth-output-power-product is necessary when being employed e.g. as a broadband THz-transmitter [5] or photonic local oscillator [6].

This dissertation focuses on novel 1.55 μm periodic travelling wave photodetectors based on miniaturized high-speed waveguide-integrated p-i-n photodiodes for ultra-broadband high-power applications. The work covers the theoretical aspects, the design, and the analysis of the travelling wave and the miniaturized lumped element photodetector. In chapter two basic considerations about efficiency, bandwidth and saturation effects of the p-i-n photodiode are carried out. The design approaches of common detector structures are compared. Chapter three presents the miniaturized responsivity-enhanced low-capacitance waveguide-integrated photodiode, which is a basic building block of the travelling wave photodetector (TWPD). Besides simulations of the optical properties, an expression for the transfer function of the lumped element photodetector including RLC-effects and carrier-transit effects is derived. The

concept, theory and the simulation results of the travelling wave photodetector with serial or parallel optical feed are followed. Chapter four summarizes the device layout and fabrication of the TWPD. Chapter five presents the measurement results, including static, high frequency electrical and optical heterodyne experiments comparing the different detector designs and vertical layer structures. Furthermore, the pulse response is studied and high power and saturation effects of the devices are discussed. In view of the operation in high-bitrate transmission systems, a fully packaged TWPD module is employed in a system experiment with bitrates up to $160\,Gbit/s$. Finally the different design approaches are compared and evaluated, with particular regard to practical use in high-speed long-haul fibre systems.

2. High-speed photodetectors

2.1. The p-i-n photodiode

A photodiode (PD) is essentially a solid-state sensor that converts an optical power into an electrical current. The light absorption process in a PD for photogeneration of electron-hole-pairs requires the photon energy to be at least equal to the bandgap energy E_g of the absorber material. Only then, the available energy of one photon is sufficient to excite an electron from the valence band (v.b.) to the conduction band (c.b.) For this band-to-band transition, the upper wavelength limit for photon absorption is given by:

$$\lambda_g\,[\mu m] = \frac{1.24}{E_g\,[eV]} \tag{1}$$

Once an electron-hole-pair is created, the electron and hole drift in opposite directions and give rise to an induced current as long as an electric field exists [7].
The fabrication of photodetectors for the "long-wavelength-regime" between $\lambda = 1.3\,\mu m$ and $1.6\,\mu m$ for telecom fibre applications demands a semiconductor material system which allows a composition of highly absorbing and transparent layers. The compound semiconductor system InGaAsP, grown lattice matched on InP sub-

	InP	$In_{0.53}Ga_{0.47}As$	ref.
bandgap E_g	$1.35\,eV$	$0.75\,eV$	[8]
refractive index n @ $1.55\,\mu m$	3.18	3.56	[9]
static dielectric constant ε_r	12.5	13.8	[10]
absorption constant α @ $1.55\,\mu m$	$\rightarrow 0$	$7000\,cm^{-1}$	[11]
electron saturation velocity v_e^{sat}	$0.75 \cdot 10^7\,cm/s$	$0.65 \cdot 10^7\,cm/s$	[11, 12]
hole saturation velocity v_h^{sat}		$0.48 \cdot 10^7\,cm/s$	[11]
electron mobility μ_e	$3500\,cm^2/V\,s$	$8000\,cm^2/V\,s$	[12]
hole mobility μ_h	$150\,cm^2/V\,s$	$300\,cm^2/V\,s$	[12]
max. electric field E_{max}	$> 400\,kV/cm$	$250\,kV/cm$	[12, 13]

Table 1: Material properties of InP and lattice matched InGaAs.

strate, fulfills these requirements. Varying compositions of the alloys allow a bandgap variation between $0.75\,eV$ ($\lambda_g = 1.65\,\mu m$) and $1.35\,eV$ ($\lambda_g = 0.92\,\mu m$). The composition of the quaternary material is commonly denoted by $In_{1-x}Ga_xAs_yP_{1-y}$. The relevant lattice matched ternary composite is $In_{0.53}Ga_{0.47}As$, which shows an absorption constant α of $7000\,cm^{-1}$ at $1.55\,\mu m$ wavelength. In table 1 some of the material properties and constants of InP and InGaAs which were used throughout this work are summarized. In order to achieve a high opto-electronic conversion efficiency and high bandwidth the p-i-n photodiode is widely used. It consists of an intrinsic absorber, sandwiched between a highly doped n^+- and p^+-layer which give rise to a space charge region. Figure 1a depicts the energy band structure of an anisotype heterostructure employing an InGaAs absorber and InGaAsP contact layers with illumination through the n-layer. The contact layers exhibit bandgap energies higher than the photon energy and are consequently transparent at the operation wavelength. At the p-InGaAsP/i-InGaAs heterojunction a thin graded bandgap layer (grading) is inserted for smoothing valence band discontinuities in order to avoid slow hole trapping effects at the heterobarrier. Due to the electric field in the absorber the photogenerated carriers are accelerated towards the electrodes and contribute to

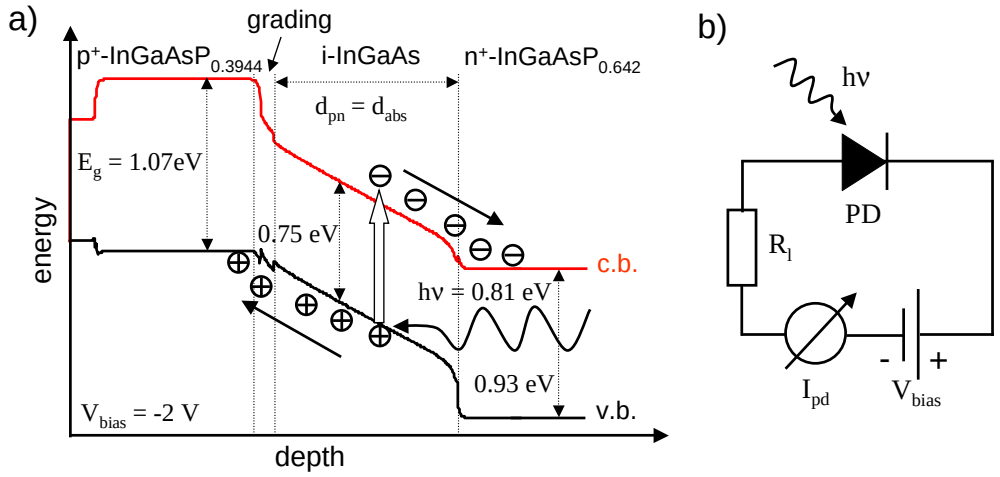

Figure 1: a) Energy band structure of a p-i-n heterostructure photodiode at $-2\,V$ bias, b) p-i-n photodiode at reverse bias with external load R_l.

the photocurrent. Compared to a simple pn-junction, this design exhibits a lower junction capacitance and avoids slow diffusion photocurrents since the carriers are solely generated in depleted high-field regions. For high-speed operation the device is reverse biased by an externally applied voltage to deplete the absorber completely and enhance the electric field (fig. 1b). Then, without illumination, a dark current due to thermal generation and -at higher electrical fields- tunnelling is measurable in an external circuit. The dark current causes shot noise which, together with thermal noise, limits the sensitivity of the photodiode.

The external quantum efficiency η_{ext} quantifies the ability of the photodiode to transform light into an electrical current and is defined as the number of charge carrier pairs generated per incident photon [8]:

$$\eta_{ext} = \frac{I_{pd}}{q} \cdot \frac{h\nu}{P_{opt}} \tag{2}$$

where I_{pd} is the photogenerated current by the absorption of the optical input power P_{opt} at a frequency ν. A common figure of merit is the external responsivity R, defined as the ratio of photocurrent to the input optical power:

$$R = \frac{I_{pd}}{P_{opt}} = \frac{\eta_{ext}\,\lambda\,[\mu m]}{1.24}\,A/W \tag{3}$$

Therefore, for an ideal photodiode with $\eta_{ext} = 1$ at $\lambda = 1.55\,\mu m$ the responsivity is $R_{ideal} = 1.25\,A/W$. Considering a vertically illuminated absorber with an absorption constant α, thickness d_{abs} and a reflectance R_o at the air-semiconductor interface, the responsivity is

$$R = \eta_{ext} \cdot R_{ideal} = R_{ideal}(1 - R_o)\Big(1 - e^{-\alpha\, d_{abs}}\Big) \tag{4}$$

Usually a real photodiode exhibits $R < R_{ideal}$, because of a finite absorber thickness d_{abs}, an optical reflectance $R_o > 0$ and other constraints such as loss due to fibre-chip coupling or carrier recombination. Whenever R depends on the state of polarization of the incoming light, the definition of the polarization dependent loss is useful:

$$PDL = 10 \cdot \log\Big(\frac{R_{max}}{R_{min}}\Big) \cdot dB \tag{5}$$

Here, R_{max} and R_{min} are the maximum and minimum responsivities for all states of polarization.

In addition to the responsivity, the electrical 3 dB bandwidth is an important figure, when evaluating high-speed photodiodes. It specifies the frequency range from DC to the cut-off frequency f_{3dB}. The latter is defined as the frequency at which the electrical output power has dropped by 3 dB below the power value at DC.

The bandwidth of a lumped element photodiode, at which the device length is much shorter than the electrical signal wavelength, might be limited mainly by the RC-time constant and the carrier drift times in the depletion region. These bandwidth constraints lead to a 3 dB bandwidth which can be approximated by [11],

$$f_{3dB} \approx \sqrt{\frac{1}{\frac{1}{f_{RC}^2} + \frac{1}{f_t^2}}} \tag{6}$$

with the RC-limited bandwidth,

$$f_{RC} = \frac{1}{2\,\pi\,R_{tot}\,C_{pd}} \tag{7}$$

and the carrier transit time-limited bandwidth:

$$f_t \approx \frac{3.5\,\bar{v}}{2\pi\,d_{abs}} \tag{8}$$

In the above equations R_{tot} stands for the photodiodes's total resistance including series and load resistances, C_{pd} is the junction capacitance and $\bar{v} = \sqrt[4]{2\,(1/v_e^4 + 1/v_h^4)^{-1}}$ is the averaged carrier drift velocity [11] with the electron and hole velocities v_e and v_h. In order to maximize f_{3dB}, the RC-time constant $(R_{tot} \cdot C_{pd})$ as well as the absorber thickness d_{abs} should be minimized. However, since $C_{pd} \propto 1/d_{abs}$, a tradeoff between a low RC-time constant and short transit time exists which generally limits the bandwidth. Equation 6 gives a good approximation as long as gaussian responses are assumed. A more detailed description of the frequency response will be given in section 3.2.1. The electron and hole drift velocities $v_{e,h}$ can be estimated by the following empirical formulas [14]:

$$v_e(E) \;=\; \frac{\mu_e\,E + \beta\,v_e^{sat}\,E^\gamma}{1 + \beta E^\gamma} \tag{9}$$

$$v_h(E) \quad = \quad v_h^{sat} \, \tanh\Big(\frac{\mu_h \, E}{v_h^{sat}}\Big) \tag{10}$$

with the electrical field E, the saturated drift velocities v_e^{sat} and v_h^{sat}, the parameters $\beta = 7.4 \cdot 10^{-10}$, $\gamma = 2.5$. Using the values for InGaAs in table 1 the field-dependent drift velocities are visualized in fig. 2. At low electric fields the drift velocities of electrons and holes increase linearly with the field. While the hole velocity saturates as the field further increases, the electron velocity shows a maximum at around $5\,kV/cm$ and decreases before saturation. This behavior is due to the transferred-electron effect [8], whereby the electrons transfer from a high-mobility energy-valley to a low-mobility satellite valley located at a higher energy above a certain threshold field. However, at high electrical fields both carriers reach their saturatation velocities whereby the electrons travel about 35 % faster than the holes. Thus the carrier transit time is defined mainly by the slow holes.

In a practical high-speed p-i-n photodiode a moderate reverse bias voltage $(1..5\,V)$ is sufficient to accelerate the carriers to their saturated drift velocities. However, at high photocurrents the electric field can be significantly weakened due to a screening effect induced by the space-charge of photogenerated holes and electrons. This gives

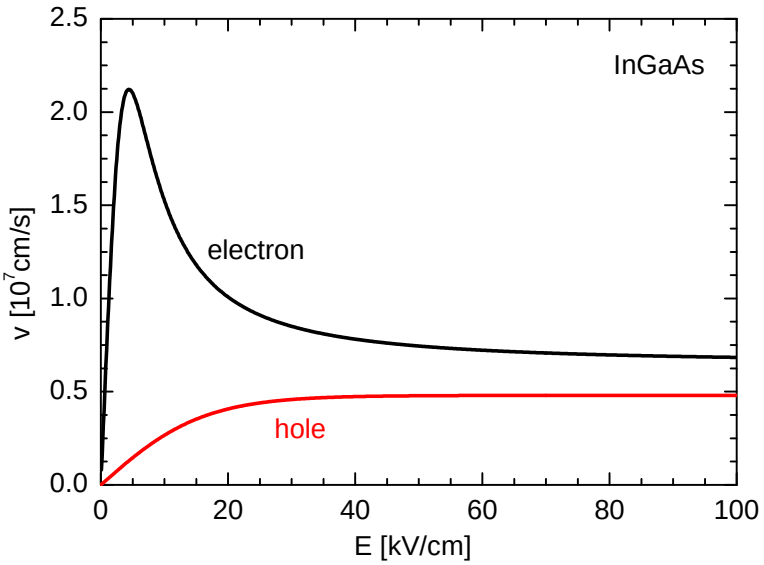

Figure 2: Electron and hole drift velocities vs. electrical field in InGaAs.

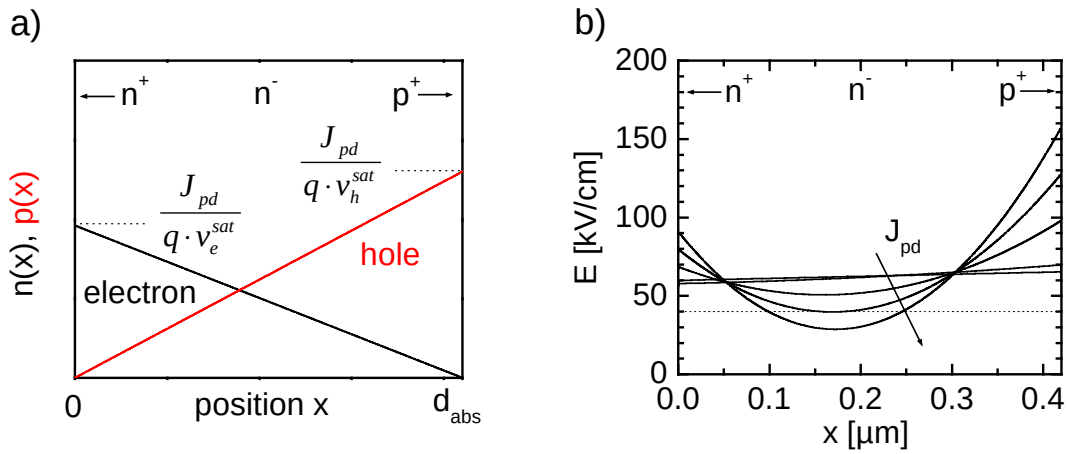

Figure 3: a) Carrier densities over position in the intrinsic absorber, b) electrical field at photocurrent densities $J_{pd} = (0,\ 1.1,\ 20,\ 40,\ 60)\frac{kA}{cm^2}$.

rise to a lower hole drift velocity and longer transit times resulting in a saturated RF (radio frequency) output power.

The electrical field can be estimated roughly by using a steady-state condition for the hole and electron densities [13]. Assuming saturated carrier velocities and a uniform illumination in the absorber, fig. 3a illustrates the instantaneous electron and hole densities $n(x)$ and $p(x)$ in the intrinsic absorber with thickness d_{abs} at a photocurrent density J_{pd}. The maximum electron density of $(J_{pd}/q\, v_e^{sat})$ occurs at the n-side of the absorber $(x = 0)$, while the maximum hole density is $(J_{pd}/q\, v_h^{sat})$ at the p-side $(x = d_{abs})$. The resulting electrical field $E(x)$ can be computed by

$$E(x) = \frac{q}{\varepsilon_0\, \varepsilon_r} \int_0^{d_{abs}} (-n(x) + p(x) + N_D)\, dx + \frac{V_{bias} + V_b}{d_{abs}} \qquad (11)$$

taking also the background doping level in the absorber N_D, the built-in voltage V_b and the external bias voltage V_{bias} into account. In eq. 11, q stands for the elementary charge, ε_0 and ε_r are the free-space permittivity and the dielectric constant of the absorber, respectively. When solving the integral, the integration constant is chosen to satisfy the requirement, that the integral over $E(x)$ equals $(V_{bias} + V_b)$. In figure 3b the electric field in the depleted absorber is plotted for various photocurrent densities J_{pd}. In this example d_{abs} is $430\,nm$, N_D is $5 \cdot 10^{11}\,cm^{-3}$ and $(V_{bias} + V_b)$

amounts to $-2.6\,V$. As for small currents the electric field is almost undisturbed, a local minimum develops for growing J_{pd}. At the same time, high field regions occur at the p-side of the absorber. Regarding the RF current one expects linear operation as long as the field is high enough at any point in the absorber to accelerate electrons and holes to their saturated drift velocities. For electric fields $< 40\,kV/cm$ the hole velocity starts to decrease (see fig. 2) which should lead to an extended transit time and a lower RF output power.

Apart from the conventional p-i-n PD, where the absorber is mostly depleted and in turn both electrons and holes contribute to the photogenerated space charge, the uni-travelling-carrier photodiode (UTC-PD) becomes increasingly interesting for high-power and high-speed operation [15, 16]. This structure employs a p-doped absorber in conjunction with a transparent intrinsic collection layer. Since the optically generated holes are majority carriers and relax with their ultra-short relaxation time constant, the bandwidth limited by carrier transit time effects is determined by the electron diffusion and drift times only. However, in order to accelerate the electron diffusion process, a built-in field has to be generated in the p-doped absorber by well-controlled bandgap- or doping-grading.

Another high-speed detector type is the metal-semiconductor-metal (MSM) photodiode on semi-insulating material, which is basically formed by two Schottky-diodes connected in series in opposite direction. While here a planar design of the interdigitated electrodes may offer a relatively low capacitance, the carrier transit times tend to be higher, due to a non-uniform and partly lower electrical field in the absorber [17]. This leads to considerable bandwidth degradations, especially at high optical input powers.

Compared to the p-i-n and MSM, the avalanche photodiode (APD) can exhibit substantially more O/E efficiency due to an internal gain mechanism. However, APDs suffer from an excess noise factor and the buildup time, which have excluded them from operation above $40\,GHz$ till now [18].

In the present work, the p-i-n structure has been chosen owing to its distinct advantages in high-speed and high-power performance and its less complex epitaxial layer structure when compared to the MSM- or APD-, and UTC-types.

2.2. Photodetector structures

Figure 4 summarizes various types of high-speed detectors. The vertically illuminated photodetector (VPD) in fig. 4a is one of the simplest structures. According to eq. 4 and 8, a tradeoff has to be made with respect to the absorber thickness between high responsivity and short carrier transit times. Therefore, the bandwidth-efficiency-product ($f_{3dB} \cdot \eta_{ext}$) is limited to 20 GHz [13] which is why the VPD is predominantly applied at moderate bit-rates up to 40 Gbit/s. Nevertheless, even when a thin absorber is used the responsivity of the VPD can be enhanced when applying rear side illumination and exploiting the return light reflected by the top electrode. With this method a bandwidth-efficiency-product of 35 GHz has been achieved by Wey et al. [19]. If a reduced spectral width can be accepted, the resonant cavity enhanced (RCE) photodetector represents another solution. With the integration of mirrors at the top and bottom of the structure multi-pass absorption can be achieved, leading to a tripled quantum efficiency in [20].
The side-illuminated waveguide photodetector (WG-PD) shown in b) overcomes the bandwidth-efficiency limitation and high efficiency and short carrier transit times can be achieved at the same time. Kato et al. presented a WG-PD with a record

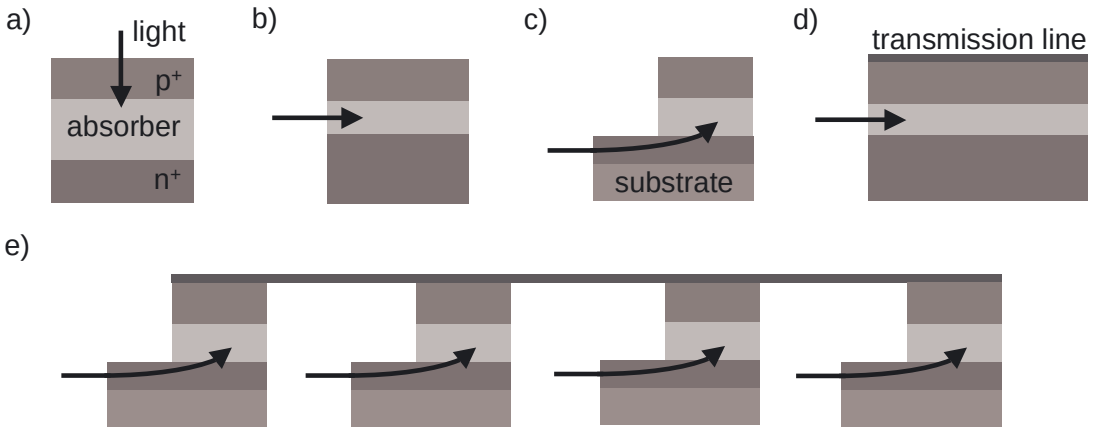

Figure 4: High speed photodiodes: a) Vertically illuminated PD, b) waveguide PD, c) waveguide-integrated PD, d) TWPD with continuous absorption, e) periodic waveguide-integrated TWPD.

bandwidth-efficiency product of $55\,GHz$ in 1994 [21]. In a WG-PD the optical absorption path is oriented perpendicular to the electric field of the p-i-n junction, since the light is injected laterally into the thin absorption layer. Hence, the responsivity is primarily controlled by the length of the detector and less by the thickness of the absorber. Similar to the VPD, this design implies the use of further optics or a tapered fibre for illumination, which makes the fibre-chip coupling more crucial and complex. The waveguide-integrated photodetector c) offers the same benefits as the WG-PD but in addition various advantages under integration aspects. Here the light couples evanescently from a waveguide to the photodiode mesa which ensures a more uniform absorption along the device length and leads to an improved high-power capability [22]. By integrating a short planar multimode waveguide a high responsivity of $1.02\,A/W$ and $48\,GHz$ bandwidth have been achieved [23]. Furthermore, independent of the active device, a mode field transformer (taper) can be easily integrated in order to improve the fibre-chip coupling efficiency; enabling the use of a cleaved fibre instead of a tapered fibre which exhibits better coupling efficiency and large alignment tolerances [24]. The waveguide-integrated PD is well-suited for the monolithic integration with further components, such as waveguides and power splitters resulting in advanced detector structures and photonic integrated circuits with increased functionality as twin- or balanced-detectors [25, 26].
As the devices a)-c) are lumped element photodetectors, the bandwidth is limited by both, the carrier drift times and RC limitation. Obviously, for highest bandwidths a small absorber volume is necessary, which leads inevitably to a compromise between available output power and speed. In contrast, 4d) displays a travelling wave photodetector with continuous absorption, where the signal wavelength is in the order of the device length. By integrating the RC elements into a transmission line (TL) and providing an impedance match to the external circuit, the device can be described as a distributed structure and overcomes the inherent RC limitation [27, 28]. However, due to the large difference in the propagation constants a phase match between the optical and electrical signals is barely achieved which can lead to bandwidth degradation in a long TWPD. Regarding the high-power capability it is comparable to the WG-PD and VPD, where the optical intensity follows an exponential decay in the absorber and saturation primarily occurs at an early stage at the optical input side. In

table 2 the characteristics of various different integration types of recently published wide-bandwidth TWPDs are summarized. Giboney et al. demonstrated a $7\,\mu m$-long TWPD with a bandwidth-efficiency product of $76\,GHz$ at $0.82\,\mu m$ wavelength [29]. The highest reported bandwidth of $560\,GHz$ together with a bandwidth-efficiency product of $45\,GHz$ have been achieved at $\lambda = 0.8\,\mu m$ with a TWPD employing an absorber based on low-temperature grown GaAs (LT-GaAs) [30]. Since this material exhibits an ultra-short carrier lifetime, most of the photogenerated carriers are trapped and recombine before they reach the electrodes. Hence, the response time of a LT-GaAs TWPD is not limited by the carrier transit times. Although it has been shown that LT-GaAs can absorb light with photon energies below the bandgap, the low absorption constant and the high trapping rate led to quantum efficiencies of only 1 % at $\lambda = 1.55\,\mu m$ [31]. Therefore, LT-GaAs based devices are unsuitable for the operation at the long telecommunication wavelengths.

The periodic TWPD in figure 4e) is the most promising candidate for high-speed and high-power operation and is the subject of this work. In this design several discrete photodiodes are combined by a transmission line to a travelling wave structure [32, 33]. In the following we distinguish between periodic travelling wave photodetectors with serial and parallel optical feed. In the TWPD with serial optical feed (S-TWPD) the photodiodes are arranged in series on one optical waveguide (fig. 5a). Compared to a single photodiode the responsivity and the linear photocurrent of a S-TWPD can be enhanced due to the increased absorber volume while maintaining

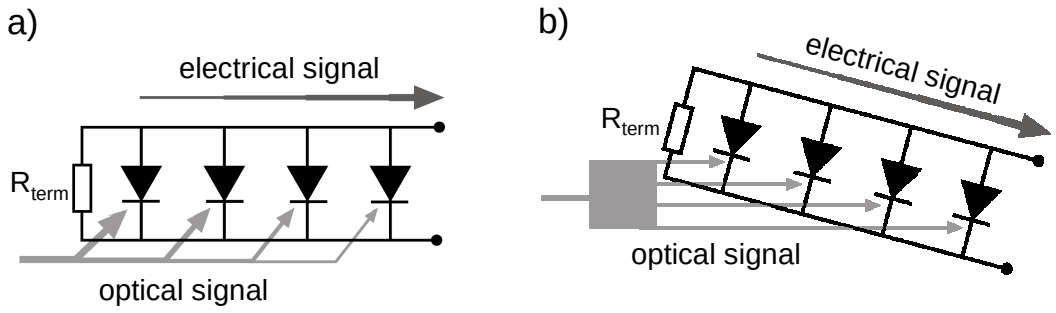

Figure 5: Schematic of travelling wave photodetector with serial (a) and parallel (b) optical feeding with termination resistor R_{term}.

year/ref.	type	material	λ $[\mu m]$	f_{3dB} $[GHz]$	R $[A/W]$	$f_{3dB} \cdot \eta$ $[GHz]$	PDL $[dB]$
2003/[35] UCLA	S-TWPD 3 p-i-n tapered TL	InGaAs-InGaAsP	1.55	38	0.24	7	
2002/[37] UCLA	P-TWPD 4 p-i-n	InGaAs-InAlAs	1.55	9	0.21	2	
2001/[42] UCLA	S-TWPD 4 p-i-n	InGaAs-InAlGaAs	1.55	35	0.42	12	
2001/[34] NTT	S-TWPD 3 UTC 50 Ω term.	InGaAs-InGaAsP	1.55	115	0.15	14	
2001/[52] UDE	cont. TWPD p-i-n	InGaAs-InGaAsP MQW	1.55	<75	0.2	<12	1.3
1998/[32] TUB	S-TWPD 4 MSM	InGaAs-InAlGaAs	1.55	78	0.1	5.9	2
1998/[30] UCSB	cont. TWPD p-i-n	LTG GaAs	0.8	560	0.05	45	
1997/[41] UCLA	S-TWPD 3 MSM	LTG GaAs	0.86	49*	0.31	22*	
1995/[29] UCSB	cont. TWPD p-i-n	AlGaAs-GaAs	0.83	172	0.3	76	0.2

Table 2: Travelling wave photodetectors, state of the art. The stars indicate that the measured bandwidth was instrument-limited.

bandwidth at the same time. A periodic TWPD with serial optical feed with 115 GHz bandwidth and 0.15 A/W responsivity has already been demonstrated [34]. In order to suppress the reflected backward propagating electrical wave this device comprised an integrated termination resistor R_{term} at the optical input side of the TL. Another

method employing a tapered TL is proposed in [35] and led to a bandwidth of $38\,GHz$ (table 2).

The periodic TWPD with parallel optical feed (P-TWPD) is auspicious for high-power operation due to the uniform optical power distribution [36]. In this case, the optical signal is split by a power divider and fed into several discrete photodiodes, which are interconnected by a transmission line (fig. 5b). A P-TWPD consisting of four PDs has been proposed by Murthy et al. [38]. They reported a responsivity of 0.21 A/W and an unsaturated RF power at 10 GHz signal frequency of $+9$ dBm [37]. However, the 3 dB bandwidth reached only 9 GHz, which was partly attributed by the authors to the RC-limit of the employed single large-area PDs.

3. Travelling wave photodetector theory and design

3.1. Principle of operation and integration concept

In the present work the periodic travelling wave photodetector is based on evanescently coupled miniaturized waveguide-integrated p-i-n photodiodes (μ-PD). It will be shown below, that by distributing the discrete photodiodes on a transmission line the TWPD can be described as a fully distributed structure within the Bragg-limit. The characteristic impedance of the entire device can be matched to that of the external circuit ($50\,\Omega$) by integrating the RC elements into a coplanar waveguide. Hence, the bandwidth is not bound by the overall RC constant and the tradeoff between maximized absorber area and RC-limited bandwidth can be overcome. The variation of the distance between the discrete photodiodes offers an additional degree of freedom in the device design and therefore allows a phase match of the optical and electrical signals avoiding walk-off effects and bandwidth degradations. In order to eliminate electrical reflections at the input of the transmission line a matching resistor R_{term} has to be integrated. Hence, unintended signal reflection can be suppressed at the expense of half of the available output photocurrent being lost. Then, without considering the material response and transmission line losses, the frequency response of a perfectly impedance-matched periodic TWPD is ultimately limited by its Bragg-frequency caused by the periodic nature of the device. In the following two types of periodic TWPDs are studied: the TWPD with serial and parallel optical feed. These structures differ in the way the optical signal is fed into the active absorber of the discrete PDs. In the case of the S-TWPD the photodiodes are arranged in series on top of a single optical waveguide (see fig. 5a). In the first detector region a fraction of the photons in the waveguide is absorbed. The portion of light which is remaining in the waveguide couples to the second detector region, and so on. With this design the overall responsivity exceeds the one of a single photodiode and ideally, the optical energy is completely absorbed at the end of the device. Hereby, the design of each single PD is optimized in terms of low radiation loss at its rear side.

The travelling wave photodetector with parallel optical feed comprises a multimode interference (MMI) power splitter of which output waveguides feed the waveguide-

integrated photodiodes symmetrically (fig. 5b). In this design the PDs are required to absorb all of the light available in the waveguide. A high-impedance coplanar waveguide (CPW) transmission line is utilized which connects the PDs in parallel and collects the electrical output signal in phase with the optical feeding. In both designs the output electrode configuration is very similar, which allows a direct comparison between the two fabricated structures.

The discrete waveguide-integrated photodiode in its particular variant is an essential basic building block of both types of TWPD and provides important insight into more fundamental limits. A schematic view of this lumped element device is shown in fig. 6a. The p-i-n mesa shown in 6b is located on top of an optical singlemode waveguide and the absorber is illuminated by evanescent optical field coupling. While the length of the intrinsic absorption layer l_{pd} determines mainly the responsivity, the carrier transit time limitation is given by the thickness of the absorber d_{abs}. The

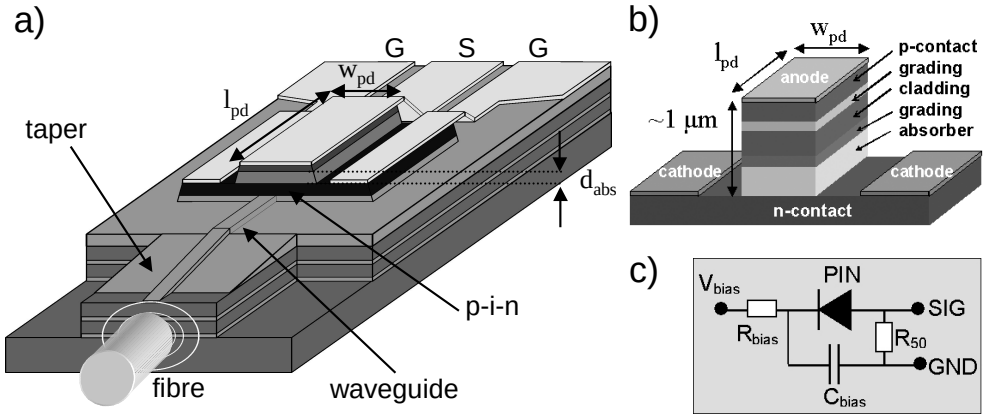

Figure 6: a) Stand-alone lumped element waveguide-integrated photodetector with mode field converter: the absorber is quasi-laterally illuminated by evanescent coupling, b) p-i-n mesa, for details on the layer structure see table 13 in appendix 7.1, c) monolithically integrated bias-circuit consisting of a bias resistor R_{bias} and a blocking capacitor C_{bias} for convenient biasing of the photodetector. Optionally a $50\,\Omega$ matching resistor R_{50} can be integrated at the RF output for best signal integrity, robustness to back reflections and expanded RC-limitation.

picture also illustrates the metallization layer forming the contacts and output pads in ground-signal-ground (GSG) configuration and the tapered mode field converter for effective fibre-chip coupling [24] which complete the photodiode to a stand-alone photodetector. The complete circuit, which is integrated monolithically on chip is sketched in fig. 6 c.

Previous work using similar concepts had already demonstrated a transit time-limited bandwidth of $70\,GHz$ [43] and $30\,GHz$ bandwidth-efficiency product of devices with $20\,\mu m$-long active area [24]. A notably higher bandwidth-efficiency product can be reached by exploiting the RLC-effects described in section 3.2.1, resulting in an increased 3 dB bandwidth at maintained responsivity. Recently, we reported a waveguide-integrated PD with an active area $(w_{pd} \times l_{pd})$ of $5 \times 20\,\mu m^2$ revealing a 3 dB bandwidth of $100\,GHz$ and a responsivity of $0.7\,A/W$ [44].

The properties of the discrete PD in terms of efficiency, PDL, capacitance, and bandwidth define to a great extent the performance of the TWPD and will be illustrated in the following sections. Moreover, used as a stand-alone photodetector its overall performance will be evaluated to allow a comprehensive comparison with the TWPD.

3.2. Discrete miniaturized waveguide-integrated photodiode

3.2.1. Simulation of the transfer function

Generally, the bandwidth of a lumped element photodiode might be limited by the RC-time constant, the carrier drift times in the depletion region, charge trapping at energy band discontinuities and the diffusion of photogenerated carriers. Carriers which are generated outside the depletion region are required to diffuse to the junction in order to contribute to the photocurrent. As the diffusion velocity is generally smaller than the drift velocity, this gives rise to an extended transit time. To minimize the diffusion effect, the light should be absorbed solely in the depleted high-field region. In a p-i-n heterostructure photodiode this could be achieved by low background doping concentration in the intrinsic absorbtion layer and a medially doped transparent spacer region between the highly doped contacts and the absorption region in order to prevent dopants from diffusing into the i-layer during the fabrication process. In addition, by employing appropriate graded bandgap layers at the heterojunctions (see fig. 1a) the

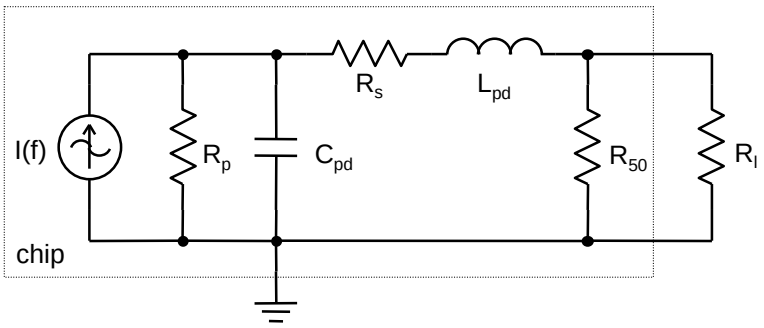

Figure 7: Equivalent circuit of a lumped element photodetector.

trapping effect at heterobarriers can be reduced [19].

Considering the RC-effect, fig. 7 shows a simple equivalent circuit of a lumped element photodetector. A photodiode is basically a current source $I(f)$ in parallel with a capacitance C_{pd} and a resistance R_p, a series resistance R_s, and an inductance L_{pd}. In order to achieve a matched transition to the external load impedance R_l ($= 50\,\Omega$), an optional termination (or matching) resistor R_{50} ($= 50\,\Omega$) may be integrated on the chip. C_{pd} is determined by the thickness d_{pn} and the area of the depleted region $A = l_{pd} \cdot w_{pd}$ and can contain a parasitic stray capacitance C_{st},

$$C_{pd} = C_{pn} + C_{st} = \frac{\varepsilon_0\,\varepsilon_r\,A}{d_{pn}} + C_{st} \tag{12}$$

with ε_r the dielectric constant of the depleted layer. The inductance L_{pd} may originate from electrical interconnections or air bridges of length l and radius r in the signal path and can be approximated with a wire model [47]:

$$L_{pd} = \frac{\mu_0}{2\pi}\,l\,(\ln(2\,\frac{l}{r} - \frac{3}{4})) \tag{13}$$

In most cases a parallel leakage current is in the nA-scale and therefore R_p becomes very high. Omitting this element in the equivalent circuit leads to the frequency dependant current I_{RLC} flowing through the load which can be written as a current-related relative transfer function:

$$\mathcal{H}_{RLC}(\omega) = \frac{I_{RLC}(\omega)}{I_{RLC}(0)} = \frac{1}{1 - \omega^2\,L_{pd}\,C_{pd} + i\,\omega\,C_{pd}\,R_{tot}} \tag{14}$$

with the total resistance:

$$R_{tot} = R_s + \frac{R_l\, R_{50}}{R_l + R_{50}} \tag{15}$$

By integrating a matching resistor, R_{tot} is reduced to $(R_s + 25\,\Omega)$. Therefore the RC limit can be expanded, but at the expense of half of the RF output current being lost. Commonly the amplitude of eq. 14 is visualized as a power-related frequency response on a logarithmic scale which is calculated by:

$$H_{RLC}(f)\ [dB] = 20{\cdot}\log(|\mathcal{H}_{RLC}(f)|) \tag{16}$$

with $f = \omega/2\pi$.

Figure 8 shows the influence of the inductance L_{pd} on the relative frequency response $H_{RLC}(f)$. In the calculation C_{pd} and R_{tot} amount to $25\,fF$ and $40\,\Omega$, respectively, corresponding to a photodiode including an R_{50}-termination with e.g. an active area A of $28\,\mu m^2$, a depletion width of $200\,nm$ (InGaAs), a stray capacitance of $8\,fF$, and a series resistance of $15\,\Omega$. In the diagram it can be clearly observed that with growing L_{pd} the response increases at a certain frequency f_r. From the derivative of eq. 16 one finds $H'_{RLC}(f_r) = 0$ with the resonance frequency $f_r = 1/(\sqrt{L_{pd}\, C_{pd}})$. This effect is called "inductive peaking" [11] and can be used to significantly enhance the 3 dB bandwidth. In the example a 3 dB bandwidth of $223\,GHz$ is reached with $L_{pd} = 20\,pH$, which corresponds to a bandwidth improvement by a factor of $\sqrt{2}$. However, at higher frequencies the increase in inductance generally leads to a higher slope and therefore to a decrease in the response when compared to $L_{pd} = 1\,pH$.

An expression for the 3 dB bandwidth due to RLC-effects can be determined by solving for the frequency f_{RLC} at which the magnitude of eq.(14) is equal to $1/\sqrt{2}$:

$$f_{RLC} = \frac{1}{2\,\pi} \cdot \sqrt{\frac{2\,L_{pd}\,C_{pd} - C_{pd}^2\,R_{tot}^2 + \sqrt{(2\,L_{pd}\,C_{pd} - C_{pd}^2\,R_{tot}^2)^2 + 4\,L_{pd}^2\,C_{pd}^2}}{2\,L_{pd}^2\,C_{pd}^2}} \tag{17}$$

For fixed C_{pd} and R_{tot}, eq. 17 exhibits a maximum at

$$L_{pd} = \frac{C_{pd}\,R_{tot}^2}{2} \tag{18}$$

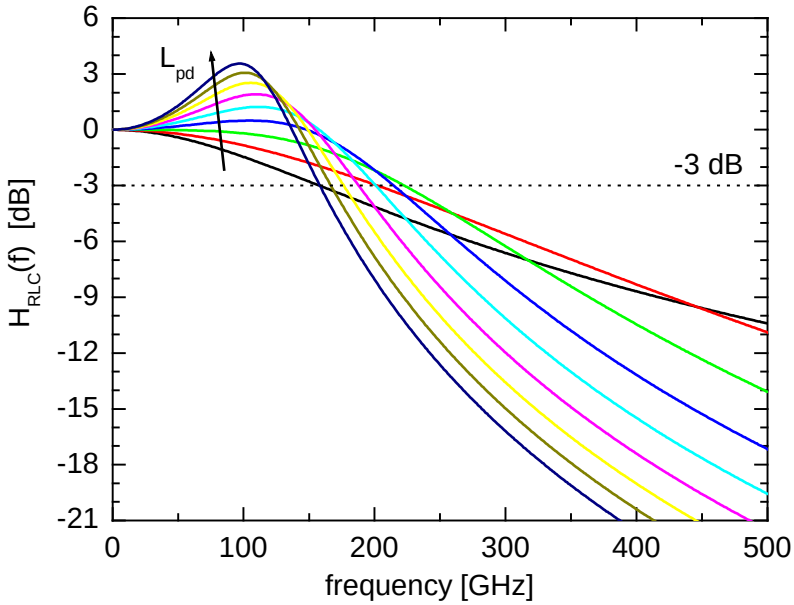

Figure 8: Relative frequency response $H_{RLC}(f)$ *for* $L_{pd} = (1, 10, 20, 30, 40, 50, 60, 70)\,pH$, $C_{pd} = 25\,fF$ *and* $R_{tot} = 40\,\Omega$.

which represents the optimum inductance to achieve a maximized RLC-limited 3 dB bandwidth.

The intrinsic frequency response caused by carrier transit-time effects has been described by several authors in the literature. While in [8] only one type of carrier is considered, Sibley et al. take electron and holes into account under the assumption of an exponential decay of the optical intensity in the absorber [45], which does not hold for evanescent optical coupling. The following approach is similar to [45], but uses an arbitrary optical power distribution $P(x,t)$ in the absorber, expressed by $P(x,t) = P_0(x) + P_1(x)\,e^{i\omega t}$. Regarding carrier transit time effects only the alternating part $(P_1(x)\,e^{i\omega\,t})$ with the modulation frequency ω is of interest, while the constant component $P_0(x)$ can be neglected. Figure 9 illustrates the considered p-i-n structure with a depleted absorber thickness d_{abs}. The absorbed power in an infinitesimal slab dx at position x with the absorption constant α amounts to

$$dP(x,t) = \alpha\,P_1(x)\,e^{i\omega t}\,dx \tag{19}$$

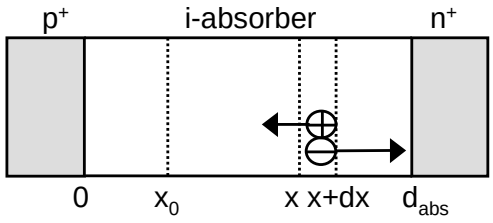

Figure 9: p-i-n structure with electron-hole-pair, reference plane at x_0 and infinitesimal slab dx at x.

and leads to an electron-hole pair generation. Assuming that every photon produces a charge carrier pair, the generation rate in the slab dx is

$$g(x,t)\,dx = \alpha\,\frac{P_1(x)}{A\,h\,\nu}\,e^{i\omega t}\,dx \tag{20}$$

whereby A stands for the cross-sectional area of the absorber, and $(h\,\nu)$ is the photon energy. Due to the electric field the photogenerated electrons and holes drift with their saturation velocities towards the n-type and p-type layer, respectively. Considering the holes first, the incremental drift current density flowing through a reference plane at x_0 (see fig. 9) at time t due to hole generation is

$$dj_h(x,t)_{x_0} = q\,\alpha\,\frac{P_1(x)}{A\,h\,\nu}\,e^{i\omega(t-t_h(x,x_0))}\,dx \tag{21}$$

taking into account that holes generated in the elemental region dx at position x arrive at the plane x_0 after a time delay t_h, given by

$$t_h(x,x_0) = \frac{x-x_0}{v_h^{sat}} \tag{22}$$

In order to find the hole current density at x_0, caused by all holes generated to the right of x_0, eq. 21 is integrated from $x = x_0$ to $x = x_{abs}$:

$$dj_h(x_0,t) = \frac{q\,\alpha}{A\,h\,\nu}\int_{x_0}^{d_{abs}} P_1(x)\,e^{i\omega(t-t_h(x,x_0))}\,dx \tag{23}$$

The integration of the above equation over the entire absorber with respect to x_0 gives the total hole photocurrent density:

$$J_h(t) = \frac{1}{d_{abs}} \int_0^{d_{abs}} dj_h(x_0, t)\, dx_0 = \frac{q\,\alpha}{A\,h\,\nu\,d_{abs}} \int_0^{d_{abs}} \int_{x_0}^{d_{abs}} P_1(x)\, e^{i\omega(t-t_h(x,x_0))}\, dx\, dx_0 \tag{24}$$

As will be shown below in section 3.2.3, especially for short PDs with $l_{pd} < 10\,\mu m$ and thin evanescently coupled absorber volumes a uniform illumination represents a reasonable approximation. By setting $P_1(x) = P$, the integrals in eq. 24 can be calculated. Taking also the current due to photogenerated electrons into account and dropping the time-dependency, the overall frequency-dependant photocurrent density is

$$J(\omega) = J_h(\omega) + J_e(\omega) \tag{25}$$

whereby $J_e(\omega)$ can be found by replacing $t_h(x, x_0)$ by $t_e(x, x_0) = (x - x_0)/v_e^{sat}$ in eq. 24. The division by $J(\omega = 0)$ of eq. 25 for normalization yields the relative frequency response due to transit effects:

$$\mathcal{H}_t(\omega) = \frac{J(\omega)}{J(0)} = \frac{1}{\omega^2\tau_h^2}\left[1 - i\omega\tau_h - e^{-i\omega\tau_h}\right] + \frac{1}{\omega^2\tau_e^2}\left[1 - i\omega\tau_e - e^{-i\omega\tau_e}\right] \tag{26}$$

Here, τ_e and τ_h stand for the electron and hole transit times through the depleted layer to the contacts and are calculated by $\tau_{e,h} = d_{abs}/v_{e,h}^{sat}$, respectively.
The corresponding power-related frequency response is designated as $H_t(f)$ following a similar definition as in eq. 16.
The relative frequency response given by eq. 26 coincides in magnitude and phase with the results from [45] where an exponential optical intensity distribution is used, as long as the penetration depth is large compared to the absorber thickness: $\alpha^{-1} \geq 2 \cdot d_{abs}$. Further comparisons with Kato et al. [11] showed good agreement in magnitude and phase response.
The total relative frequency response including RLC- and transit-time effects is the product of equations (14) and (26):

$$\mathcal{H}_{pd}(\omega) = \mathcal{H}_{RLC}(\omega) \cdot \mathcal{H}_t(\omega) \tag{27}$$

with the power-related frequency-dependant amplitude in $[dB]$:

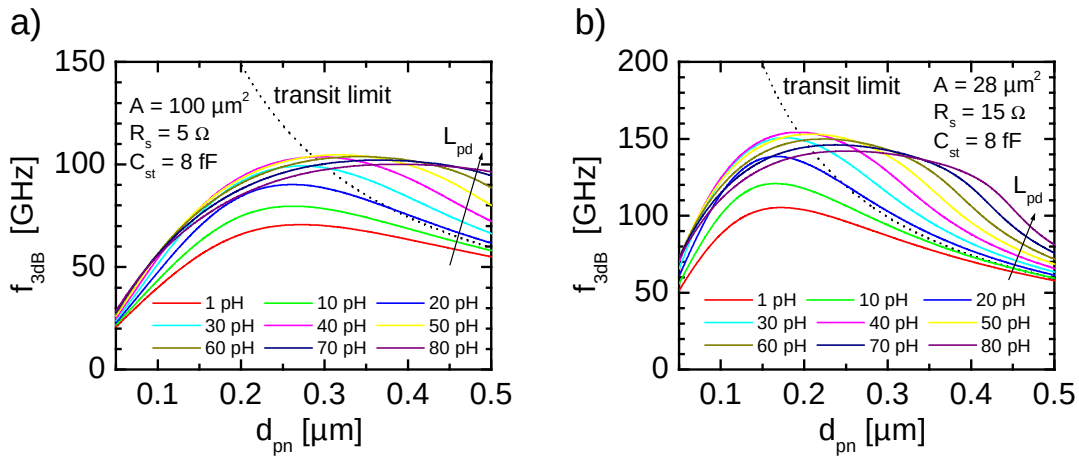

Figure 10: Bandwidth vs. d_{pn} for $A = 100\,\mu m^2$ (a), and $A = 28\,\mu m^2$ (b) for various L_{pd}. Transit- and RLC-effects are considered. The series (contact-)resistance is estimated with $5\,\Omega$ and $15\,\Omega$, accounting for the different contact areas. The dotted lines show f_{3dB} solely due to transit effects.

$$H_{pd}(f) = H_{RLC}(f) + H_t(f) \tag{28}$$

From eq. 27 the resulting 3 dB bandwidth is found numerically by the determination of f_{3dB} which satisfies $|H_{pd}(f_{3dB})| = 1/\sqrt{2}$.

In figure 10, f_{3dB} is plotted in dependance of d_{pn} for two InGaAs p-i-n PDs with $A = (5 \times 20)\,\mu m^2$ (a) and $A = (4 \times 7)\,\mu m^2$ (b) with termination resistor. Different line colors correspond to different values of L_{pd}. As expected, for thin absorbers ($d_{pn} < 0.31\,\mu m$ in fig. 10a), f_{3dB} increases linearly with d_{pn} which suggests that the 3 dB bandwidth is limited mainly by the RC-effect. For larger d_{pn} the transit limit predominates, which gives rise to $f_{3dB} \propto 1/d_{pn}$.

An inductance of $50\,pH$ and an optimum thickness of $d_{pn} = 0.31\,\mu m$ lead to a maximum f_{3dB} of $105\,GHz$ of a $100\,\mu m^2$-device. For even higher values of L_{pd}, the bandwidth starts to decrease again. When assuming the ideal case with a series resistance $< 5\,\Omega$, the bandwidth is slightly increased up to $115\,GHz$. In order to achieve bandwidths higher than $115\,GHz$ the active area and the depletion width have to be substantially smaller. As fig. 10b illustrates, a bandwidth of $154\,GHz$

seems feasible with $d_{pn} = 200\,nm$, $L_{pd} = 40\,pH$ and $A = 28\,\mu m^2$. In general, in order to determine the optimum inductance for a maximized bandwidth eq. 28 has to be evaluated numerically. While in the RC-limited regime the optimum inductance for a given PD area behaves like $\propto 1/d_{pn}$ (see eq. 18), in the transit time-limited regime $L_{pd} \propto d_{pn}$ is applied. Apparently, with a correct choice of inductance the overall bandwidth may even exceed the transit time limited bandwidth due to the resonance effect.

However, it should be noted that the inductive peaking effect should not lead to a 3 dB bandwidth in substantial excess to the transit time-limited bandwidth in order to avoid a deterioration of the signal integrity. The effect can be described by the relative group delay scatter, defined as

$$gd(\omega) = -\frac{d}{d\omega}\phi(\omega) \tag{29}$$

and becomes visible e.g. in the time domain, when investigating undershoot and ringing of the pulse response. In eq. 29, $\phi(\omega)$ denotes the phase response of the transfer function in eq. 27.

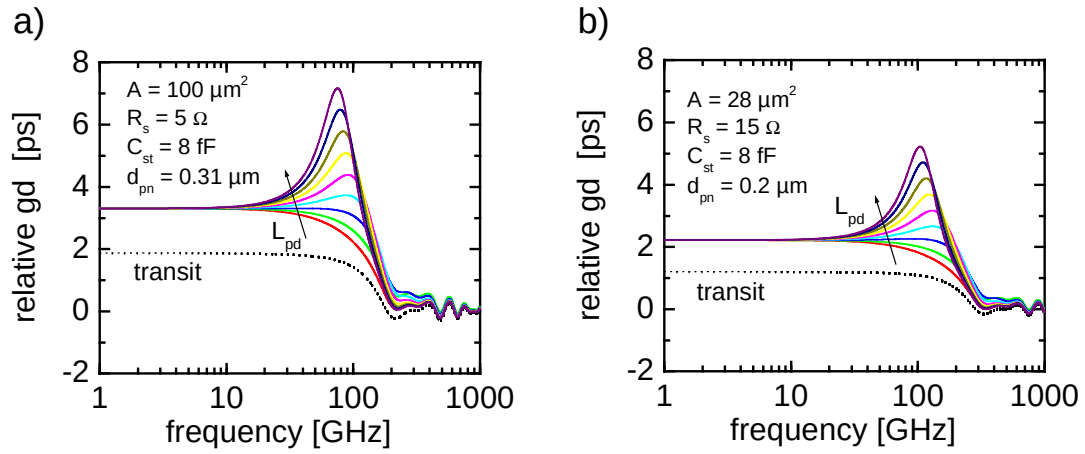

Figure 11: Relative group delay for $A = 100\,\mu m^2$ (a) and $A = 28\,\mu m^2$ (b) with $L_{pd} = (1, 10, 20, .., 80)\,pH$ determined from eq. 29. The dotted lines show $gd(f)$ due to pure transit effects using eq. 26.

Figure 11a shows $gd(f)$ of a PD with $A = 100\,\mu m^2$ and $d_{pn} = 0.31\,\mu m$. With growing inductance, the maximum group delay at f_r increases significantly, while f_r itself moves slightly to lower frequencies. In practice, the maximum differential group delay within the 3 dB bandwidth defined as $max(gd(f)) - min(gd(f))$ with $0 < f < f_{3dB}$ is of special interest. With view to a PD with $L_{pd} = 50\,pH$ and $f_{3dB} = 105\,GHz$, the differential group delay amounts to $2\,ps$. In comparison, the relative group delay due to pure transit effects is almost flat up to $100\,GHz$. In the case of the $28\,\mu m^2$-device shown in 11b, the peaking effect is somewhat less pronounced.

Together with the miniaturization of the device the use of a dual depletion region (DDR) is a potential method to further expand the bandwidth of a p-i-n PD. In this vertical layer design the higher saturated drift velocity of the electrons compared to the holes is exploited [46]. To this point we presupposed a depleted absorber region $(d_{pn} = d_{abs})$, of which thickness determines transit times and device capacitance at the same time. By adding a transparent and depleted drift layer d_{drift} between the absorber and the n-type contact as depicted in fig. 12, the junction capacitance can be reduced reasonably $(C_{pn} \propto (d_{abs} + d_{drift})^{-1})$. Even though the total transit time of the electrons is now higher, the overall bandwidth can be increased. Bandwidth-improvements of up to 100% might be possible when exploiting the higher electron saturation velocity in a PD with dual depletion region.

Figure 13 shows the calculated 3 dB bandwidth of a DDR PD versus depleted absorbtion layer d_{abs}. In the figure the parameter x is defined as $d_{drift}/d_{abs} = x$. In the calculation, eq. 27 is used with $d_{pn} = d_{abs} + d_{drift}$ and, in order to estimate

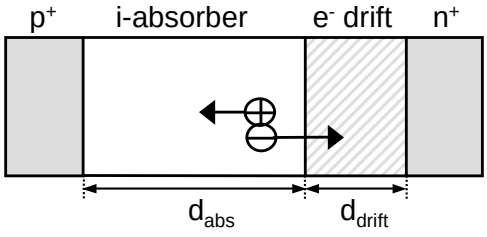

Figure 12: p-i-n PD with dual depletion region (DDR) consisting of an intrinsic absorber d_{abs} and transparent wider band gap drift layer d_{drift}.

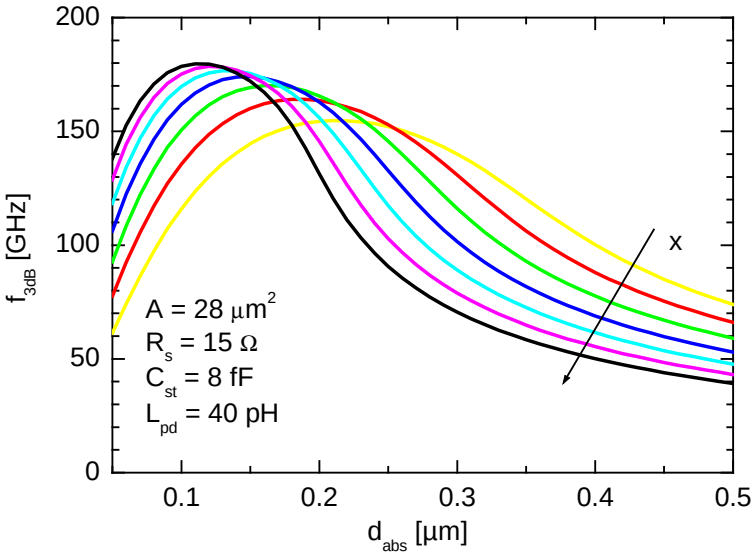

Figure 13: 3 dB bandwidth for $A = 28\,\mu m^2$, $L_{pd} = 40\,pH$ and $x = 0, 0.25, ..., 1.5$ of a DDR PD. For the saturated drift velocities of the electrons and holes apply: $v_e^{sat} = 1.4 \cdot v_h^{sat}$. The curve for $x = 0$ represents a PD without drift layer.

the electron's longer drift path, $\tau_e = (d_{abs} + d_{drift})/v_e$. Especially for small d_{abs}, the introduction of a drift layer increases the bandwidth significantly, as here the predominating RC-limitation can be suspended. For $x = 1.5$ and $d_{abs} = 0.1\,\mu m$ the bandwidth can be pushed to $180\,GHz$. As expected, in the transit time-limited regime for $d_{abs} > 200\,nm$ an implementation of the drift layer leads to a deterioration of the bandwidth. In a TWPD the DDR PD can be utilized to lower the capacitively loading significantly when at the same time only a slight increase in transit time can be accepted. The use of the DDR offers an additional design parameter and could be used to expand the Bragg-limit, by reducing the spacing of neighboring μ-PDs.

3.2.2. Optical simulation

The optical fields in a waveguide structure, which is invariant in the direction of field propagation z, can be expressed as a superposition of the radiation modes and guided modes. Hence, the confined fields are a linear combination of M forward and backward propagating 2D modes determined by the mode profiles $\vec{E}_k(x, y)$ and

$\vec{H}_k(x,y)$, and the forward and backward amplitude a_k and b_k. Disregarding the time dependance $\exp(i\omega t)$ and considering only the guided components, the fields can be expressed by (e.g. [48])

$$\begin{aligned} \vec{E}(x,y,z) &= \sum_{k=1}^{M}(a_k e^{-i\beta_k z} + b_k e^{i\beta_k z})\vec{E}_k(x,y) \\ \vec{H}(x,y,z) &= \sum_{k=1}^{M}(a_k e^{-i\beta_k z} - b_k e^{i\beta_k z})\vec{H}_k(x,y) \end{aligned} \tag{30}$$

The complex propagation constant β_k is related to the effective refractive index of a mode $n_{eff,k}$ by

$$n_{eff,k} = \frac{\beta_k \lambda}{2\pi} \tag{31}$$

The time-averaged energy flux of the fields propagating in the direction $\vec{z}$ is given by the z-component of the Poynting vector $[\frac{J}{s\,m^2}]$:

$$S_z(x,y,z) = \frac{1}{2} Re((\vec{E}(x,y,z) \times \vec{H}^*(x,y,z))_z) \tag{32}$$

The magnitude of $S_z(x,y,z)$ represents a measure of the optical power per unit area and unit time carried by the field in direction of $\vec{z}$ and is equivalent to the field intensity $I(x,y,z)$.

The total power $P(z)$ is found by integrating the latter over the entire transverse cross section of the waveguide: $P(z) = \int\int I(x,y,z)\,dxdy$.

In a three-dimensional structure consisting of a series of waveguides with different 2D cross sections, the modes have to be found for each waveguide individually. The coupling between the modes of two adjacent waveguides 1 and 2 can be described by the mode excitation coefficient η_k, which is determined by the coupling efficiencies between the M modes in waveguide 1 and the mode k in waveguide 2.

In a lossy media, the imaginary part of the complex index of refraction $n = n' - ik$ provides information about the absorption constant α of the material:

$$\alpha = -\frac{4\pi\, Im(n)}{\lambda} \tag{33}$$

Apart from α, the confinement or filling factor is an important measure in order to quantify the absorption process in a waveguide. The confinement factor Γ_{xy} describes the fraction of power confined in a defined absorber cross section A_{abs}:

$$\Gamma_{xy}(z) = \frac{\int^{A_{abs}} I(x,y,z)\,dA}{\int_{-\infty}^{\infty} I(x,y,z)\,dA} \tag{34}$$

Using this definition, the effective absorption constant is

$$\alpha_{eff}(z) = \alpha\,\Gamma_{xy}(z) \tag{35}$$

and determines the damping of the propagating light. The conversion to a logarithmic scale is given by

$$\alpha_{eff}(z)\ [dB/\mu m] = 4.343 \cdot \alpha_{eff}(z)\ [1/\mu m] \tag{36}$$

Since $\alpha_{eff}(z)$ is a function of z in eq. 35, this approach takes possible beating effects in multimode waveguides into account.
Apart from the desired absorption which leads to the photogeneration of charge carriers in the photodiode, other loss mechanisms, e.g. due to attenuation of the optical wave in the metallic top electrode, can be taken into account by introducing the absorption constant $\alpha_m(z)$. The infinitesimal change of the optical power dP over a distance dz is then proportional to the power $P(z)$, the effective absorption constant $\alpha_{eff}(z)$, and $\alpha_m(z)$:

$$dP = -P(z)\,(\alpha_{eff}(z) + \alpha_m(z))\,dz \tag{37}$$

The integration from $z = 0$ to z and resolving for $P(z)$ yields the optical power in the waveguide at position z:

$$P(z) = P(0)\ \exp\Big(-\int_0^z (\alpha_{eff}(z) + \alpha_m(z))\,dz\Big) \tag{38}$$

In the case of a straight singlemode waveguide, the confinement factor is independent of the position z, resulting in $\alpha_{eff}(z) = \alpha_{eff}$. Assuming additionally $\alpha_m(z) = 0$, the integration of eq. 37 leads to the absorption law: $P(z) = P(0)\,e^{-\alpha_{eff}\cdot z}$.

In order to predict and simulate quantitatively the optical properties of the waveguide-integrated photodiode the commercially available software *FIMMWAVE* by photon design [49] has been used. This tool is based around a complex, vectorial 2D waveguide solver using the film mode matching (FMM) method due to [50]. Here, the 2D modes are found solving semi-analytically a discrete eigenproblem by scanning over a range of values of the propagation constant β. The overall field distribution is modelled by propagating the modes of each section and calculating their coupling efficiencies at the joints.

In *FIMMWAVE*, the time-averaged energy density $[\frac{nJ}{m^3}]$, defined as,

$$u(x,y,z) = \frac{Re[\varepsilon(x,y,z)]\,\vec{E}(x,y,z)\,\vec{E}^*(x,y,z)}{4} + \frac{\mu_0\,\vec{H}(x,y,z)\,\vec{H}^*(x,y,z)}{4} \quad (39)$$

is used to visualize the field's intensity distribution. As long as the longitudinal field component is small compared to the transversal component, $I(x,y,z) \propto u(x,y,z)$ is a valid approximation, as the energy density is related to the intensity by: |power flux| = group velocity · energy density. The present work makes use of the above relation as the longitudinal field components in the investigated waveguides are considerably smaller than the transversal components.

Figure 14 presents the simulation results of the 2D mode intensity profiles for TE polarization supported in a rib waveguide (a) and PD mesa (b). The underlying vertical layer stack was adopted from [44] and is given in table 3. The refractive indices n used in the simulation were deduced from the material compositions utilizing the expressions in [65, 66]. The feeding waveguide with a rib of $2\,\mu m$ width and $0.2\,\mu m$ height is located on top of a diluted waveguide (only partly shown in fig. 14a) which is utilized by the spot-size converter [24]. Around $1.55\,\mu m$ wavelength, the waveguide supports one mode with an effective index of $n_{eff} = 3.21$.

As shown in fig. 14b, the PD mesa with $w_{pd} = 5\,\mu m$ is located on top of the waveguide layers and is formed basically by the top metal layers (anode), the p-contact layer, the cladding which is embedded between the grading layers, the absorber and the n-contact. Since the refractive indices of the waveguide, the n-contact layer and the absorber fulfill the inequation: $n_{waveguide} < n_{n-contact} < n_{absorber}$, a vertical coupling is ensured. In contrast, the cladding exhibits $n_{cladding} < n_{absorber}$, preventing

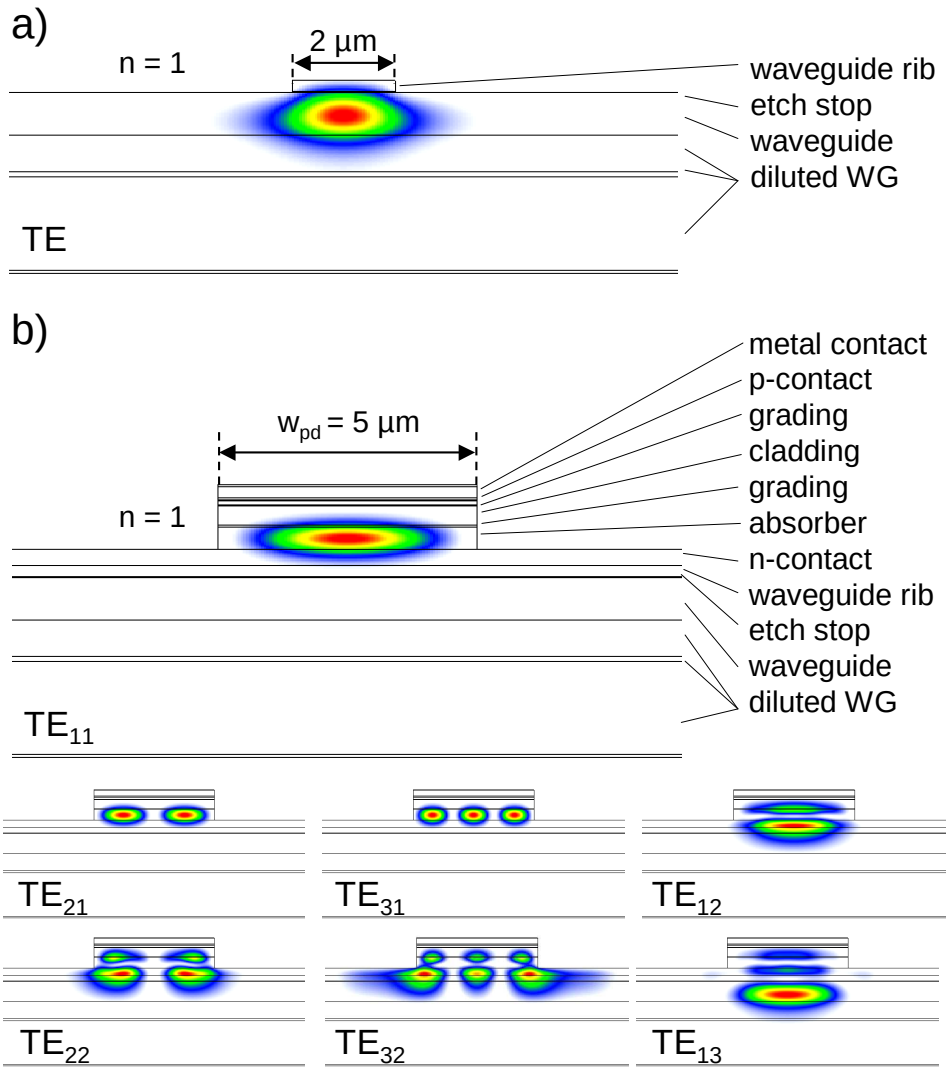

Figure 14: Calculated TE xy-intensity profiles (a) in the singlemode feeding waveguide, (b) in the PD mesa (lowest order modes). The numbering of the modes reflects their horizontal and vertical orders. The metal contact on top with $n = 0.56 - i9.8$ *and* $d = 0.32\,\mu m$ *forms the anode. The layer sequence used in the simulation refers to table 3.*

the light from getting attenuated by the metal contact. As can be seen from fig. 14b, the active region supports modes of horizontal and vertical higher order. Corresponding to their vertical order, primarily two types of guided modes can be distinguished: modes of vertical order one, which are confined in the mesa, and modes of higher order, which also reveal overlap to the waveguide layer beneath (evanescent modes). The real part of the effective index and the mode confinement Γ_{xy}^{k} of the modes shown in fig. 14b are listed in table 4. One finds that the first three modes exhibit large confinement factors as their fields are well-confined in the PD mesa, which consequently leads to a very effective absorption of the modes. However, in the waveguide-integrated PD they were up to now mainly irrelevant, since they provide only small overlap with the field distribution of the feeding waveguide and are barely excited. The same is true for any mode with even vertical order, since excitation occurs in the centre of the PD mesa. This can be seen when calculating the mode excitation coefficients due to mode coupling between the passive feeding waveguide and the PD mesa. Figure 15 gives an example for a simulated structure, consisting

function	compound	$d\,[nm]$	n
p-contact	p^+-$In_{0.53}Ga_{0.47}As$	80	3.56-i 0.086
grading	p-$InGa_{0.3}As_{0.64}P$	5	3.41
cladding	p-$InGa_{0.18}As_{0.39}P$	380	3.31
grading	p-$InGa_{0.34}As_{0.73}P$	30	3.44
absorption	n.i.d $In_{0.53}Ga_{0.47}As$	430	3.56-i 0.086
n-contact	n^+-$InGa_{0.3}As_{0.64}P$	320	3.41
waveguide rib	s.i. $InGa_{0.11}As_{0.25}P$	200	3.26
etch stop	s.i. InP	20	3.18
waveguide	s.i. $InGa_{0.11}As_{0.25}P$	820	3.26
diluted waveguide	s.i. InP/InGaAsP	4500	
substrate	s.i. InP	500000	3.18

Table 3: Vertical layer stack with layer thicknesses d and refractive indices n used in the simulation (coincident with wafer TWPD#2).

	TE_{11}	TE_{21}	TE_{31}	TE_{12}	TE_{22}	TE_{32}	TE_{13}
$n_{eff,k}$	3.44	3.43	3.41	3.26	3.26	3.24	3.21
Γ_{xy}^{k}	0.69	0.69	0.69	0.12	0.11	0.08	0.05

Table 4: Real part of the effective index and confinement factor of the TE modes depicted in fig. 14b.

of the singlemode rib waveguide and the multimode PD mesa from fig. 14. The light, propagating from left, couples mainly via the modes TE_{12} (49%) and TE_{13} (36%) into the active region.

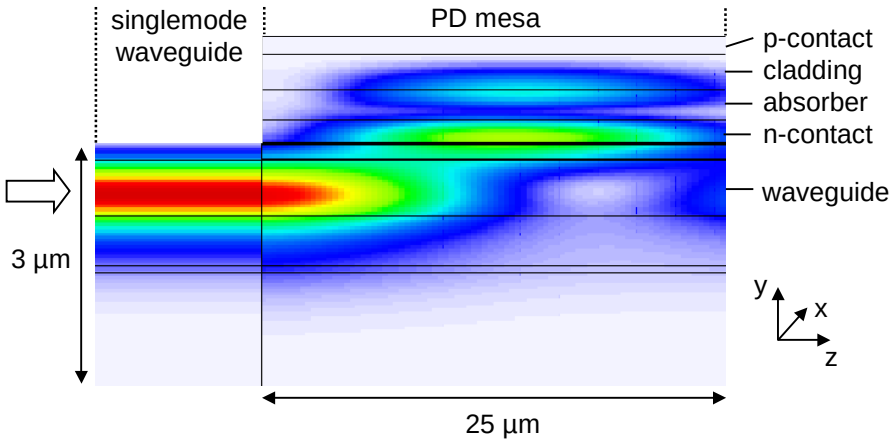

Figure 15: Side view of the calculated optical intensity distribution for TE polarization in a waveguide-integrated photodiode consisting of a singlemode waveguide and a PD mesa. The intensity is averaged over the x-direction. The cross-sectional structure corresponds to fig. 14.

The photodiode's responsivity and polarization dependent loss can be determined from the simulated 3D field distribution. The practical calculation of R and PDL starts with

1. Finding the guided modes in the considered waveguide cross sections.
2. Calculation of the time-averaged intensity field distribution by using eq. 39 and $I(x_i, y_j, z_k) \propto u(x_i, y_j, z_k)$ at the grid points x_i, y_j, z_k in the 3 D structure.
3. The summation of the intensity distribution over the entire calculational window gives the normalized z-dependant total optical power at z_k:

$$P(z_k) = p \sum_{x_i} \sum_{y_j} I(x_i, y_j, z_k)\, dA_{xy} \tag{40}$$

   Here, dA_{xy} is the area per grid point. The normalization factor p is chosen, so that $P(z_k = 0) \equiv 1$ at the input of the device.
4. Summation of the intensity distribution over the cross section of the absorber leads to the optical power confined in the absorber:

$$P_{abs}(z_k) = p \sum_{x_i=x_{min}}^{x_{max}} \sum_{y_j=y_{min}}^{y_{max}} I(x_i, y_j, z_k)\, dA_{xy} \tag{41}$$

   with x_{min}, x_{max} and y_{min}, y_{max} defining the absorber cross-sectional area $A_{abs} = (x_{max} - x_{min}) \cdot (y_{max} - y_{min})$.
5. Definition of the optical confinement factor $\Gamma_{xy}(z_k)$ and effective absorption constant $\alpha_{eff}(z_k)$ according to eq. 34 and 35.
6. Evaluating the fraction of power absorbed within the absorber in the slice dz_k:

$$dP_{abs}(z_k) = P(z_k)\, \alpha_{eff}(z_k)\, dz_k \tag{42}$$

   and assuming that every photon generates an electron-hole pair, the responsivity in dependance of the photodiode's length l_{pd} is calculated with:

$$R = R_{ideal} \cdot \int_0^{l_{pd}} dP_{abs}(z) \approx R_{ideal} \cdot \sum_{z_k=0}^{l_{pd}} dP_{abs}(z_k) \tag{43}$$

7. Accomplishing the above procedure for the orthogonal state of polarization and using eq. 5 leads to the polarization dependent loss.

All simulations have been carried out at $1.55\mu m$ wavelength.

3.2.3. Photodiode optimization, design and characteristics

An extension of the bandwidth beyond 110 GHz requires a considerable thin absorber ($< 300\,nm$) and a reduction in device capacitance ($< 25\,fF$), even when RLC-effects are exploited, as figure 10 confirms. These requirements are also valid for the use of the PD in a TWPD. As will be shown below, a low capacitance of the discrete PD is mandatory for the TWPD, as otherwise an impedance match in conjunction with a large Bragg-frequency can hardly be achieved.
Generally, a thin absorber gives rise to an increased device capacitance which results in case of a lumped element PD in a reduced RC-limit. Since the thickness of the depleted layer is defined by carrier transit time considerations, a reduced capacitance can be realised by minimizing the width and the length of the active area (see eq. 12). For a PD with a width of $5\,\mu m$, the above requirement results in a PD length of less than $10\,\mu m$. However, a reduction in absorber length generally leads to a decrease in responsivity. Therefore, the objective was the design of a highly efficient miniaturized p-i-n photodiode suitable for the use as a stand-alone photodetector or in a TWPD, provided that the optical integration concept based on singlemode feeding waveguides can be maintained.
In a waveguide-integrated photodiode, the evanescent wave coupling leads to gradual optical feeding of the absorber. Especially the first few microns of the absorber suffer from a reduced illumination (see fig. 15), which affects adversely the performance of devices with short absorber lengths. Even though this part of the active region contributes fully to the pn-capacitance, it has only a small effect on the overall responsivity.
It has been shown previously that by exploiting mode beating effects in multimode waveguides, either by implementation of an optical matching layer [63, 64] or by using exclusively a planar multimode waveguide [23], an enhanced responsivity of waveguide-integrated photodiodes can be achieved. This effect was firstly observed

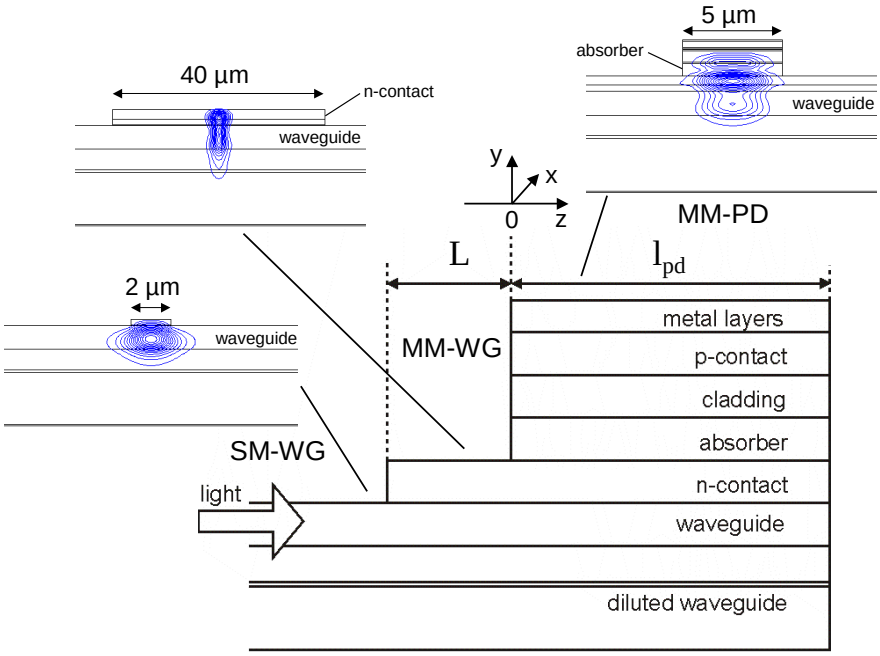

Figure 16: Side view of the photodiode. The light is injected from the left into the mode field transformer (not shown) and couples evanescently from the waveguide into the p-i-n mesa. The insets depict the optical 2D intensity profiles in the xy-plane present in the singlemode waveguide (SM-WG), multimode waveguide (MM-WG) and multimode PD mesa (MM-PD) for $L = 7\,\mu m$ and $l_{pd} = 5\,\mu m$, note the different x-scales.

at photodiodes with lengths $> 40\,\mu m$ by R. J. Deri et al., introducing the "vertical impedance matching" (VIM) structure.

In the present work a multimode waveguide inserted between the feeding waveguide and the PD-mesa is utilized in order to enhance the absorption process in the PD. Figure 16 depicts a schematic side view of the most relevant layers of the proposed photodiode. The cross-sectional structures of the singlemode waveguide (SM-WG), the multimode PD mesa (MM-PD) and the layer stack correspond to figure 14a,b and table 3, respectively. Between the singlemode waveguide and the PD-mesa the n-type contact layer is extended by a certain well-defined length L and forms a multimode waveguide (MM-WG); a cross-sectional structure is depicted in fig. 17. Due to its

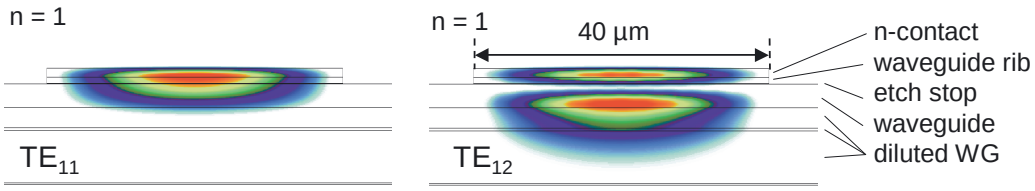

Figure 17: Calculated xy-intensity profiles (TE) in the multimode waveguide (MM-WG) of the mode TE_{11} (left) and TE_{12} (right). For clarification, the y-axes are stretched. Vertical layer structure as in table 3.

large width of $40\,\mu m$ the multimode waveguide MM-WG supports a great number of TE and TM modes of order $i1$ and $j2$, whereas in fig. 17 only the intensity profiles of the two lowest order modes TE_{11} with $n_{eff} = 3.25$ (left) and TE_{12} with $n_{eff} = 3.19$ (right) are presented. Provided that at least these two modes are sufficiently excited by the incident field of the singlemode waveguide, mode beating effects in the vertical direction occur, which can be exploited for an early coupling upwards from the waveguide. By this design, the n-contact layer serves as an optical matching layer by providing a refractive index match between the waveguide and absorber and controlling the optical intensity distribution in the active device in dependance of the length L. In order to study the effect of the multimode waveguide length L on the responsivity, simulations were carried out following the approach described in section 3.2.2. Using the layer structure with $d_{abs} = 430\,nm$ given in table 3, the simulation covers the singlemode waveguide (see fig. 14a), the multimode waveguide (fig. 17) and the PD-mesa (fig. 14b), whereby the multimode sections were modelled with 40 and 8 modes, respectively. The curves in fig. 18a show the calculated responsivities versus PD length l_{pd} for the MM-WG lengths $L = (2, 7, 13)\,\mu m$. The fibre-chip coupling efficiency and the influence of the integrated spot-size converter were taken into account by applying a constant factor of 0.7 to all calculated responsivities which led to an excellent match with the characteristics of the experimental data (circles in fig. 18) derived from photodiodes with $L = 2\,\mu m$. A similar good agreement between calculation and experiment was found for the orthogonal state of polarization (see fig. 18b). In the case of $L = 2\,\mu m$, the simulation as well as the measurements reveal

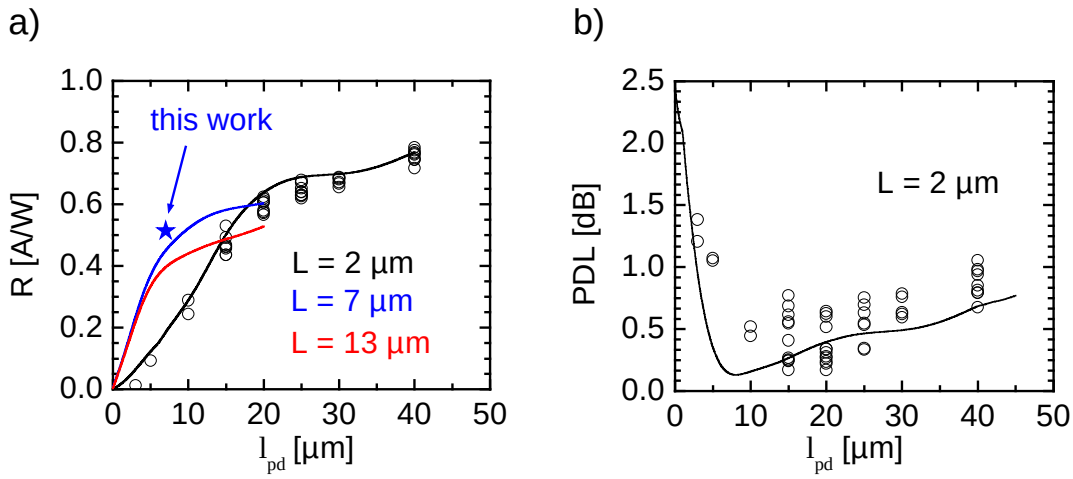

Figure 18: a) Simulated responsivities for $L = (2, 7, 13)\,\mu m$ (curves) and experimental data (circles) of photodiodes with $L = 2\,\mu m$. The measurement conditions are described in section 5.1. The blue star indicates the experimental result of the optimization of the present work with $L = 7\,\mu m$. b) Calculated and measured PDL of the devices with $L = 2\,\mu m$. For all results applies $w_{pd} = 5\,\mu m$ and the structure in table 3.

a non-exponential relation of the responsivity to the photodiode length, indicating that the responsivity decreases for low-capacitance photodiodes with the required PD lengths $l_{pd} < 10\,\mu m$ to less than $0.3\,A/W$. By extending L to $7\,\mu m$, the simulation shows that the responsivity can be considerably enhanced. Especially for $l_{pd} < 15\,\mu m$ an increase in responsivity by a factor of more than two seems feasible. In contrast, an extension to $L = 13\,\mu m$ does not lead to further improvement.

The insets in fig. 16 visualize the TE intensity distributions in the xy-plane in each of the three cross sections for $L = 7\,\mu m$ and $l_{pd} = 5\,\mu m$. The intensity distribution in the SM-WG is z-invariant, whereas the intensity profiles in the multimode sections are z-dependent. In the figure, the intensity plots of the MM-WG and MM-PD refer to the relative z-positions $-1\,\mu m$ and $2\,\mu m$, respectively. While in the SM-WG the light is well-confined in the waveguide layer, the MM-WG exhibits vertical mode beating effects which provide a coupling from the waveguide into the n-layer at an optimum

length L. As a consequence, this leads to an efficient illumination of the absorption layer in the MM-PD. In particular the first few microns of the absorber are illuminated now and contribute to the absorption process.
In the following, the responsivity enhancement effect is investigated in more detail.
In order to determine the actual relevance of the modes supported in the MM-PD for the light propagation, the mode excitation coefficients η_k were calculated at the interface MM-WG/MM-PD. Moreover, the product of η_k and the modes' confinement factor Γ_{xy}^k gives information about the individual mode's importance for the absorption process. In fig. 19a, $(\eta_k \cdot \Gamma_{xy}^k)$ of the modes listed in table 4 is shown in dependance of L. In the considered range of L, only the modes TE_{11} TE_{12} and TE_{13} are sufficiently excited and have to be taken into account. Due to mode beating effects in the MM-WG, these curves exhibit strong oscillations with similar periodicities. As for $L < 5\,\mu m$ the modes TE_{12} and TE_{13} are of equal relevance, the highly confined mode TE_{11} gains of importance with increasing L showing a maximum $(\eta_k \cdot \Gamma_{xy}^k)$ at $L = 13\,\mu m$.
A quantitative explanation of the observed responsivity enhancement can be given by analysing the characteristics of the effective absorption constant. As $\alpha_{eff}(z)$ is deduced from the total intensity distribution according to eq. 35, it takes mode beating effects in the MM-PD into account. Figure 19a illustrates the effective absorption constant in dependence of the position z for $L = (2, 7, 13)\,\mu m$.
In the case of $L = 2\,\mu m$ one observes, that the curve slowly increases up to a maximum value of $0.35\,dB/\mu m$ at $z = 14\,\mu m$, which reflects a continuous evanescent coupling from the waveguide into the absorber. As expected, specially for short absorber lengths $< 10\,\mu m$, this design is less effective as the average α_{eff} decreases to less than $0.17\,dB/\mu m$. In contrast, extending L to $7\,\mu m$ leads to considerable improvement at short PD lengths. Now the light couples advantageously into the active region which leads to a maximized effective absorption constant. The calculation shows that α_{eff} reaches a maximum of $0.5\,dB/\mu m$ and does not drop below $0.2\,dB/\mu m$ up to $z = 15\,\mu m$. For a $10\,\mu m$-long PD, its average value amounts to $0.45\,dB/\mu m$. In this range the effective absorption is predominantly constant, which is equivalent to a uniform distribution of the photocurrent density. This feature is especially beneficial to the operation under high optical power levels in order to avoid

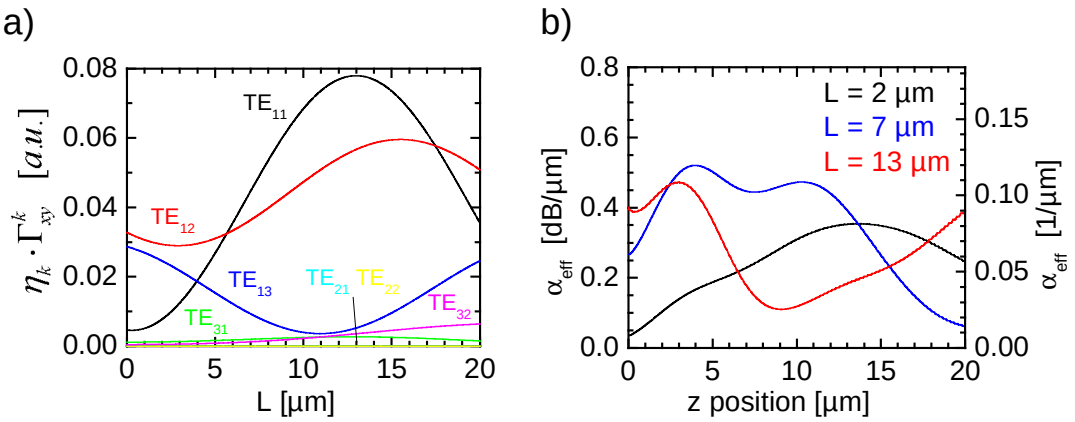

Figure 19: a) Product of excitation coefficient and mode confinement of the TE modes supported in the MM-PD, b) calculated α_{eff} vs. position z in the PD mesa for $L = (2, 7, 13)\,\mu m$ (TE). For all calculations applies $w_{pd} = 5\,\mu m$ and the structure in table 3.

local saturation effects at an early stage. For $L = 13\,\mu m$, α_{eff} can be further increased for very small z. However, the pronounced mode beating effects in the MM-PD lead to a strong z-dependance of α_{eff}, which cause a distinct decrease for $z > 4\,\mu m$.

For the practical design of the low-capacitance photodiode, a maximized responsivity in conjunction with a minimized polarization dependance is most desirable.
Referring back to fig. 18b, one observes that in agreement with the simulation, the PDL amounts to less than $1\,dB$ for devices with PD lengths $10\,\mu m < l_{pd} \leq 45\,\mu m$ but increases strongly for very small $l_{pd} \leq 5\,\mu m$. Interestingly, the calculated curve exhibits a local minimum around the PD length of $7\,\mu m$. Consequently this length was chosen in the novel design of the miniaturized photodiode.
In order to verify experimentally the simulation results in terms of the responsivity enhancement, photodetectors with $w_{pd} = 5\,\mu m$ and $l_{pd} = 7\,\mu m$ with various lengths L, ranging between $1\,\mu m$ and $11\,\mu m$, have been realised. Figure 20a gives the measured responsivities together with the theoretical expectations. Results from photodiodes comprising two different vertical layer stacks with $d_{abs} = 430\,nm$ and $d_{abs} = 200\,nm$ are shown. Their nominal layer structures can be found in table 3 and in table 13,

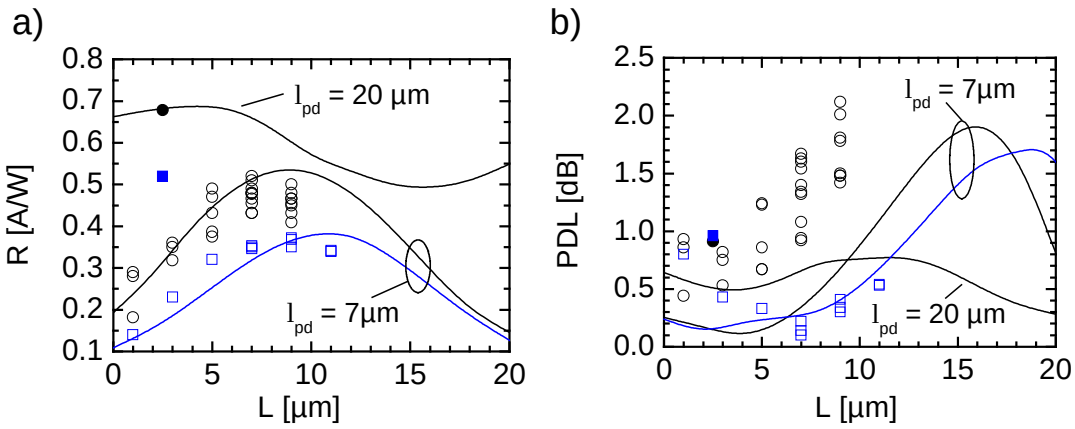

Figure 20: External responsivity (a) and PDL (b) over matching layer length L. Open circles (squares) denote results from PDs with $7\,\mu m$ length with $430\,nm\,(200\,nm)$-absorber. Filled symbols represent PDs with $20\,\mu m$ length. The lines display the simulation results. The layer structures are given in table 3 (13).

appendix 7.1, respectively.

Independently from the absorber thickness, the devices show very similar behavior in accordance with the simulations. A factor of 0.85 (0.75) was applied to the calculated responsivities in order to match the measured characteristics of the devices with $d_{abs} = 430\,nm$ $(200\,nm)$.

For $L = 7\,\mu m$, maximum responsivities up to $0.51\,A/W$ are measured in the case of the $430\,nm$-absorber. This is almost twice the responsivity of a device with $L = 1\,\mu m$. Compared to a PD with a threefold absorber length $l_{pd} = 20\,\mu m$ and $R = 0.67\,A/W$ [44], this value corresponds to a decrease of only 24%. As can be seen from fig. 18a, by exploiting multimode effects, the responsivity of a $7\,\mu m$-device has been increased to that of a PD with a length of $15\,\mu m$. Consequently, the new design allows a 50 %-reduction of capacitance at maintained responsivity.

A similar result is obtained for photodiodes with $200\,nm$-absorber. Here, the responsivity peaks with $0.37\,A/W$ at $L = 9\,\mu m$. Due to the reduced absorbing cross section one generally expects a 25% decrease in responsivity compared to the $430\,nm$-

absorber.
From the above results one derives, that the optimum device length ($=L + l_{pd}$) is apparently associated to the beat length of the two most prominent modes in the MM-WG, defined as

$$L_\pi = \frac{\lambda}{2\,(n^1_{eff} - n^2_{eff})} \tag{44}$$

In the case of the photodiodes with $d_{abs} = 430\,nm$ and $l_{pd} = 7\,\mu m$ for example, the optimum device length amounts to $14\,\mu m$ which is in good agreement with the beat length of $L_\pi = 13\,\mu m$, determined for the modes in the MM-WG shown in fig. 17 with $n^1_{eff} = 3.25$ and $n^2_{eff} = 3.19$.
Additional measurements of devices with a reduced MM-WG width of $6\,\mu m$ (compare fig. 17) did not reveal any significant differences in the responsivities. Furthermore, the simulation suggests that the influence of the MM-WG on the responsivity of a PD with $20\,\mu m$-absorber length is less pronounced.
Fig. 20b shows the results of the PDL measurement. Consistent with the calculations, a small PDL of less than $1\,dB$ can be achieved for the relevant values of L. In the case of the $430\,nm$-absorber, a spreading of $0.5\,dB$ of the PDL data is observed, which may be attributed to the peripheral position of the devices on the wafer and the consequential variation in the fabrication process. However, for larger L the increase in the polarization dependence is significant, a fact which can not be explained by mode beating effects in the multimode waveguide, as the calculated beat lengths for TE and TM agree within $\pm 1\,\mu m$.

3.3. Capacitively-loaded coplanar transmission line

The distributed TWPD is based on discrete photodiodes connected in parallel by a transmission line, which collects the electrical output signal. For interconnection, the coplanar waveguide transmission line with subjacent insulator layer is an advantageous device as it exhibits low loss and low dispersion and, compared to air bridges, gives an increased mechanical stability. Furthermore, the dielectric serves as a passivation layer and the compatibility of the device to flip-chip bonding techniques is enhanced, as all electrical interconnections are on top of the structure. Figure 21, left, shows

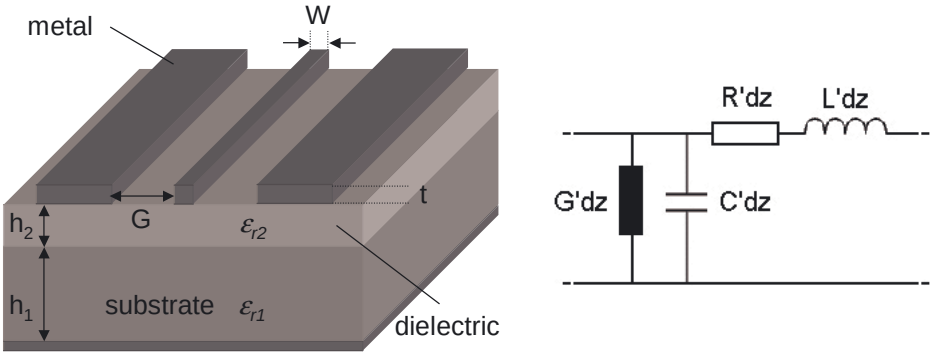

Figure 21: Left: Two-layered CPW structure with finite thickness substrate and backed ground plane, right: equivalent circuit representation of an infinitesimal TL section.

a schematic of the proposed CPW: The metal contacts in ground-signal-ground configuration with a signal line width W, a gap G and a metallization thickness t are on top of the insulating dielectric layer, e.g. Benzocyclobuten (BCB), with h_2 and ε_{r2}, which is spun on semi-insulating InP-substrate with height h_1.
Generally, the characteristic impedance Z and propagation constant γ of a CPW transmission line are given by

$$Z = \sqrt{\frac{R' + i\,\omega\,L'}{G' + i\,\omega\,C'}} \tag{45}$$

$$\gamma = \sqrt{(R' + i\,\omega\,L')(G' + i\,\omega\,C')} = \alpha + i\beta \tag{46}$$

with the series impedance per unit length $R' + i\,\omega\,L'$ and shunt admittance per unit length $G' + i\,\omega\,C'$ (fig. 21, right). L' and C' denote the inductance and capacitance per unit length, respectively. R' and G' represent the losses of the coplanar line, caused by ohmic and dielectric loss mechanisms. Radiation loss will be neglected throughout this work, as it only becomes noteworthy for frequencies well above 100 GHz [55].
The phase constant and the attenuation constant are defined by $Im(\gamma) = \beta$ and $Re(\gamma) = \alpha$, respectively. The attenuation constant caused by conductor loss is a function of frequency ($\propto \sqrt{f}$) because of the skin effect and can be computed using analytical expressions [59, 57]. The dielectric loss is related to the loss tangent of the

dielectric and can be ignored for a CPW based on high-resistivity $(10^7\,\Omega cm)$ semi-insulating InP-substrate and BCB (loss tangent: 0.0008) [59, 60].
As stated further below, the measured loss is found to be equivalent to a series resistance of only $10\,\Omega/mm$ at $100\,GHz$. Even though this gives rise to dispersion of Z and γ in eq. 45 and 46, the effect is small enough to neglect R' and G' for the moment. For the lossless case eq. 45 becomes:

$$Z = \sqrt{\frac{L'}{C'}} \tag{47}$$

The electrical phase velocity v is given by

$$v = \frac{2\pi f}{\beta} = \frac{\omega}{\beta} = \frac{1}{\sqrt{L'\,C'}} \tag{48}$$

and is approximately equivalent to the electrical group velocity.
In order to employ the two-layered coplanar waveguide in the design of the TWPD the quasi-static-TEM parameters of the unloaded CPW line are discussed first. The analysis is based on the conformal mapping method described in [59]. Again, loss is neglected. In this approach the values of the characteristic impedance Z and the phase velocity v of the transmission line are given by:

$$Z = \frac{1}{C'\,v} \tag{49}$$

$$v = \frac{c}{\sqrt{\varepsilon_{eff}}} \tag{50}$$

where c is the velocity of light in free space and ε_{eff} is the effective dielectric constant. Approximate analytic formulas for calculating the parameters of multi-layered coplanar waveguides can be found in [56]. Transferring them to the structure shown in figure 21 (left) leads to the expressions for the characteristic impedance and the effective dielectric constant

$$Z = \frac{30\,\pi}{\sqrt{\varepsilon_{eff}}}\,\frac{K'(k_1)}{K(k_1)} \tag{51}$$

$$\varepsilon_{eff} = \epsilon_e - \frac{0.7\,(\epsilon_e - 1)\,\frac{t}{G}}{\frac{K(k_1)}{K'(k_1)} + 0.7\,\frac{t}{G}} \tag{52}$$

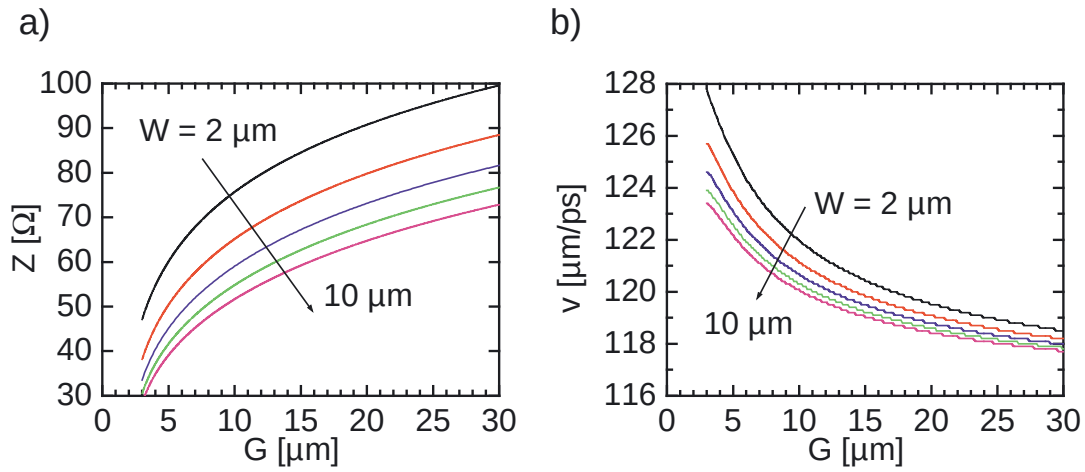

Figure 22: a) Impedance Z and phase velocity v (b) vs. gap G calculated for CPW transmission lines with $W = 2, 4, 6, 10\,\mu m$, $t = 3\,\mu m$, $h_1 = 500\,\mu m$, $\varepsilon_{r1} = 12.5$ (InP), $h_2 = 0\,\mu m$.

with the complete elliptic integral of the first kind and its complement $K(k_1)$ and $K'(k_1)$, which are given together with k_1 and ϵ_e in appendix 7.2.

Using the above formulas, the characteristic impedance Z and the phase velocity v can be computed in dependence of the gap G (see fig. 22a,b). A high-impedance line can be achieved by choosing a small width of the center conductor W combined with a large gap. In contrast, the phase velocity is less dependent on W and G and decreases only slightly for larger gaps. Figure 23 shows the dependence of Z and v on the insulator thickness for three different transmission line geometries. With growing thickness h_2, both, the impedance and the velocity increase due to the smaller line's capacitance. For practicable values of the insulator layer thickness $h_2 = 1..2\,\mu m$ the parameters increase by about 10% compared to a CPW without dielectric.

By integrating periodically several discrete p-i-n photodiodes into the above discussed TL, the parameters of the transmission line are significantly affected. Now, due to the additional pn-capacitance the device can be more commonly called a capacitively-loaded transmission line, although an additional series resistance and inductance are also present. Figure 24a shows a schematic of the loaded CPW comprising four PDs

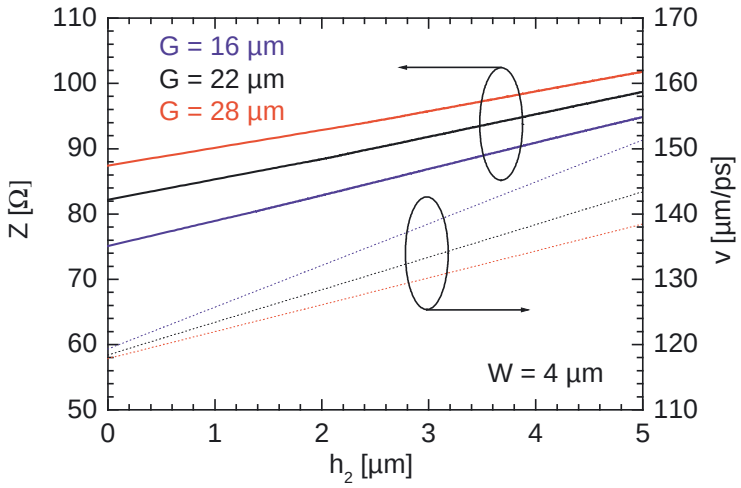

Figure 23: Characteristic impedance Z and electrical phase velocity v vs. insulator thickness h_2 of unloaded CPW lines calculated for different geometries with $W = 4\,\mu m$, $t = 3\,\mu m$, $h_1 = 500\,\mu m$, $\varepsilon_{r1} = 12.5$ (InP), $\varepsilon_{r2} = 2.7$ (BCB).

and the resulting lumped element equivalent circuit (b), depicting only one section with a length d. Provided that the electrical signal wavelength is in the order of the device length, the entire PD-loaded CPW can be described as one transmission line. Then, the periodical irregularity induced by the photodiodes' circuit elements can be averaged over the section length. In figure 24, R_s and C_{pd} denote the photodiodes' series resistance and capacitance, respectively. Hence, the resulting characteristic impedance Z_0 is

$$\begin{aligned} Z_0 &= \sqrt{\frac{Z'}{Y'}} \quad \text{with} \\ Z' &= R'(f) + i\,\omega\,L' \quad \text{and} \\ Y' &= G'(f) + i\,\omega\,C' + \left((R_s + \frac{1}{i\,\omega\,C_{pd} + G_{pd}} + i\,\omega\,L_{pd})d\right)^{-1} \end{aligned} \tag{53}$$

In most cases the parallel conductance G_{pd} and the series inductance L_{pd} are very small and can be omitted. Assuming negligible losses eq. 53 yields

$$Z_0 = \sqrt{\frac{L'}{\frac{C_{pd}}{d} + C'}} \tag{54}$$

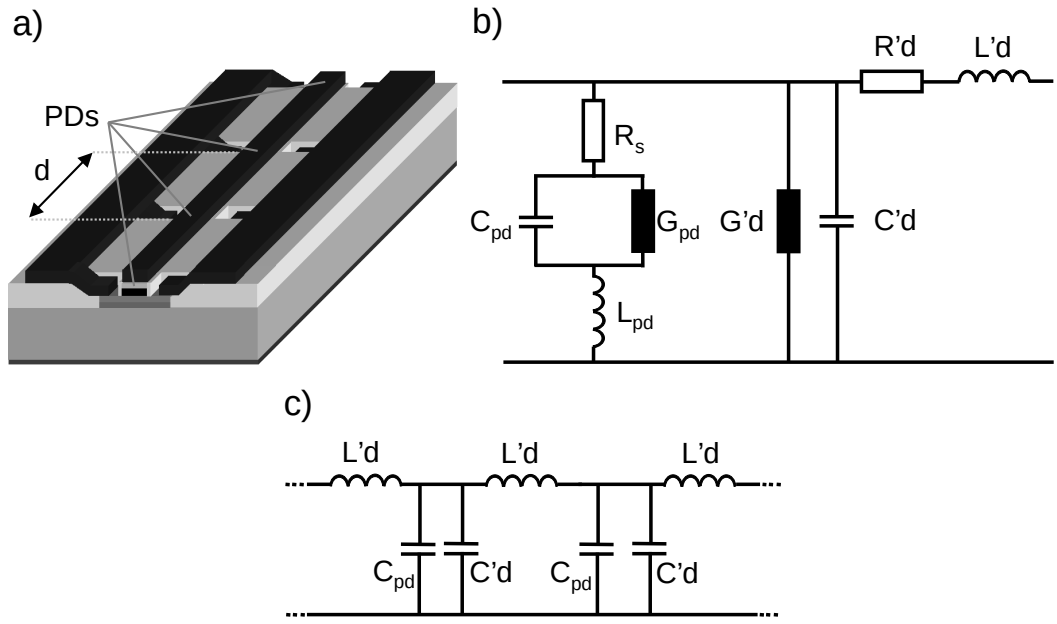

Figure 24: a) Schematic of periodically loaded CPW, b) equivalent circuit of one section of a PD-loaded CPW, c) lossless capacitively-loaded CPW.

Obviously, by integrating photodiodes with the capacitance C_{pd} within a transmission line, the overall characteristic impedance becomes lower compared to an unloaded CPW. This effect increases for shorter spacings d between adjacent photodiodes. Correspondingly, the electrical phase velocity ($\approx$ group velocity) is

$$v_0 = \sqrt{\frac{1}{L' \cdot (\frac{C_{pd}}{d} + C')}} \tag{55}$$

Here, the phase velocity decreases with increasing C_{pd}: the electrical signal can be slowed down significantly.

The above formulas describe a capacitively-loaded CPW with an equivalent circuit shown in fig.24c as a synthetic transmission line independently of the number of sections. The same result is obtained when assuming an equivalent circuit based on Π- or T-elements (see appendix 7.3).

This approach is valid for frequencies well below the Bragg-frequency f_{bragg} [61, 62], which is defined:

$$f_{bragg} = \frac{1}{\pi\sqrt{d \cdot L'(d \cdot C' + C_{pd})}} \tag{56}$$

(The derivation of this expression can be found in appendix 7.3.)
For frequencies approaching f_{bragg}, the device can no longer be described as a transmission line and the periodic nature of the device is revealed. The Bragg phenomena causes reflections and, with regard to the opto-electronic transfer function, a noticeable ripple with growing frequency, which results in a cut-off around f_{bragg}. It can be seen as a fundamental bandwidth limit of the periodically loaded transmission line and its upper limit will be determined in the following.
The above set of formulas 54-56 can be utilized as the design equations for a TWPD. For a given Z_0 and v_0 the required impedance Z and phase velocity v of the unloaded (lossless) CPW can be found by combining eq. 54 and 55 and resolving for C' and L'. One obtains

$$\begin{aligned} Z &= \sqrt{\frac{L'}{C'}} = \sqrt{\frac{\frac{Z_0}{v_0}}{\frac{1}{Z_0 v_0} - x}} \\ v &= \frac{1}{\sqrt{L'\,C'}} = \frac{1}{\sqrt{\frac{Z_0}{v_0}\left(\frac{1}{Z_0 v_0} - x\right)}} \end{aligned} \tag{57}$$

with the effective loading $x = C_{pd}/d$. Figure 25a gives an example of Z and v over x, provided that $Z_0 = 50\,\Omega$ and $v_0 = 86\,\mu m/ps$. The latter value is equivalent to the optical signal velocity in the waveguide, as will be shown below. With growing x the impedance as well as the phase velocity of the unloaded CPW must be increasing. The maximum loading is limited by

$$x < x_{lim} = \frac{1}{Z_0\,v_0} \tag{58}$$

and requires that $C' \to 0$ as well as $Z, v \to \infty$. In practice the limit is considerably lower than eq. 58, as $v < c$ and Z can not be arbitrarily chosen, as can be seen from fig. 22.

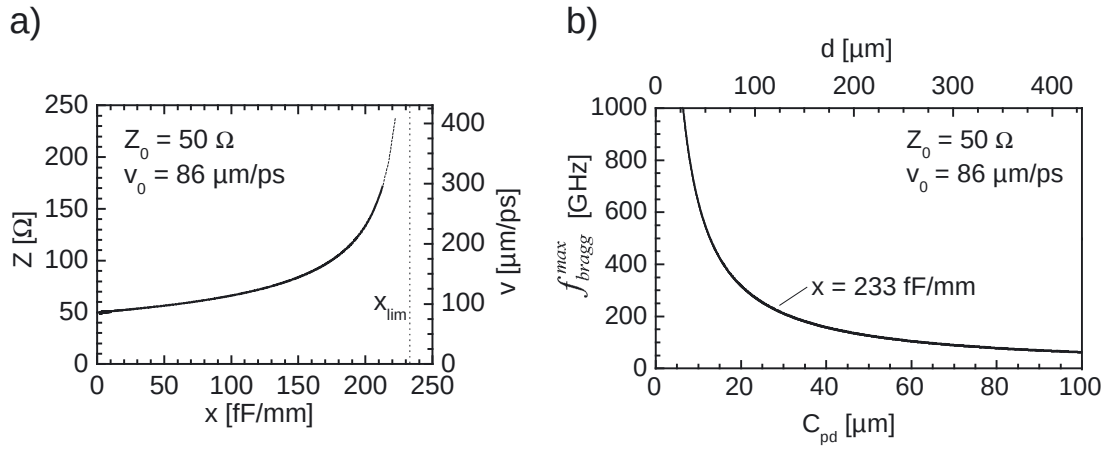

Figure 25: a) Required CPW characteristics vs. effective loading. Here, the maximum possible loading is 233 fF/mm, b) maximum Bragg-frequency.

Once eq. 54 and 55 are satisfied, $C' = (1/(Z_0 v_0) - x)$ and $L' = (Z_0/v_0)$ can be substituted into eq. 56 and the Bragg-frequency can be expressed by d:

$$f_{bragg} = \frac{v_0}{\pi\, d} \tag{59}$$

Hence, the maximum achievable Bragg-frequency f_{bragg}^{max} for a given C_{pd}, Z_0 and v_0 is associated with the shortest possible spacing $d = v_0\, Z_0\, C_{pd}$. Replacing d in the previous equation leads to:

$$f_{bragg}^{max} = \frac{1}{\pi\, Z_0\, C_{pd}} = 2\, f_{RC} \tag{60}$$

By putting $Z_0 = R_l$, this formula coincides with the expression for twice the power-related 3 dB bandwidth of a lumped RC-limited circuitry f_{RC}, which can be derived from fig. 7, with omitting all elements except from C_{pd} and R_l.

In fig. 25b, the upper limit of the Bragg-frequency versus C_{pd} is shown. The top axis gives the corresponding shortest possible spacings. As expected, a decrease in capacitance leads to smaller spacings and therefore to larger Bragg-frequencies. In order to achieve a Bragg-limit in excess of 200 GHz, the PD spacing has to be chosen smaller than 135 μm. Then, the maximum PD capacitance which can be integrated

in an intended $50\,\Omega$-line amounts to 30 fF. It should be noted however, that in a practical design the Bragg-frequency might be definitely lower as a maximum loading can not be compensated by the coplanar line.

3.4. Phase mismatch of periodic TWPD

The considerations have so far excluded the propagation characteristics of the optical signal in the TWPD. In the following, it is assumed that one optical input signal is distributed by an appropriate waveguide network to the discrete photodiodes.
Generally speaking, the distributed TWPD may suffer from potential phase mismatch due to different optical and electrical propagation constants and path lengths in the device. As soon as the longitudinal dimensions of the TWPD ($\sim$ 300 μm) are in the order of half of the signal wavelength ($\sim$ 450 μm at $100\,GHz$) these effects have to be taken into account when evaluating the bandwidth limitations, in contrast to a compact lumped element photodetector.
While the electrical signal travels approximately with v_0 on the transmission line, the optical group velocity is v_g^o, and can be computed from the group index of the optical waveguide:

$$v_g^o = \frac{c}{n_g} \tag{61}$$

As a rule it is $v_0 \neq v_g^o$ and $d \neq d_o$. Hereby d_o stands for the difference in the optical path length between two adjacent photodiodes. Figure 26 visualizes the propagation of a pulsed input signal in a simplified TWPD comprised of $m = 4$ discrete photodiodes PD1-PD4. The PDs are located at intervals of d on a transmission line with $Z = Z_0$, which connects the devices in parallel and provides the RF output at one of its ends. Optically, the PDs are separated by d_o, which gives rise to a delayed optical feeding. In this model each PD is treated as a punctual current source, feeding a forward and backward propagating photocurrent, each with magnitude $\frac{I_n}{2}$ into the TL. For simplification, only phase mismatch due to delay effects and different path lengths is regarded whereas carrier transit time-effects, Bragg-reflections, dispersion and impedance mismatch are disregarded.
The following considerations distinguish between the perfectly "terminated" and the

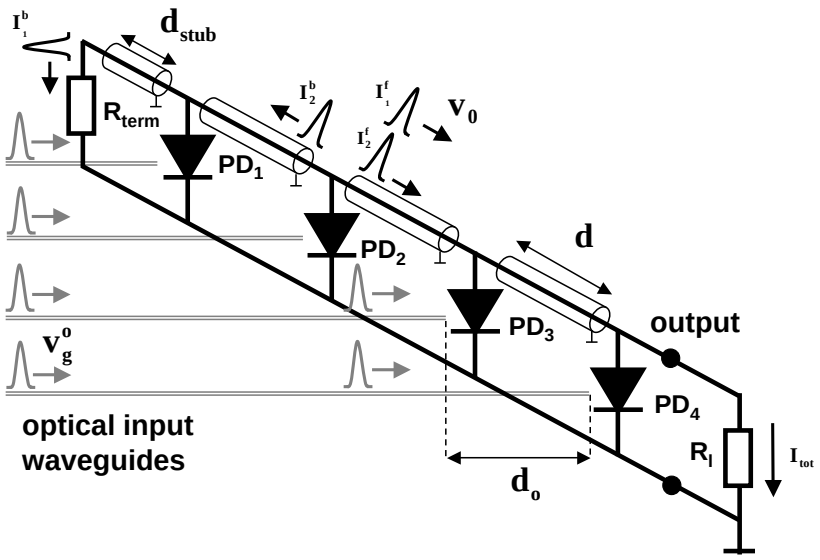

Figure 26: Simplified sketch of a terminated TWPD considering phase mismatch effects.

unterminated "open" TWPD. The terminated TWPD incorporates a matching resistor with $R_{term} = Z_0$ at its transmission line input, while the input of the unterminated TWPD is described by an open stub with length d_{stub}. The termination resistor represents a matched load to the line and ensures zero-reflection of the incident waves. The open input causes a 100% in-phase reflection of the backward travelling signals, which are then superimposed to the forward travelling waves.

Considering an optical input signal generated by means of the O/E heterodyne technique which is modulated at the frequency ω with 100% modulation depth, the total RF output current flowing through an external load with $R_l = Z_0$ is given by the sum of the forward and reflected backward propagating currents, I^f_n and I^b_n, of all m individual photodiodes:

$$I_{tot}(\omega) = \sum_{n=1}^{m} (I^f_n(\omega) e^{-\alpha(m-n)\,d} + \Gamma\, I^b_n(\omega) e^{-\alpha(d\,(n+m-2))+2\,d_{stub})} \tag{62}$$

whereby α is the transmission line's attenuation coefficient.

For the two important cases of the terminated and unterminated TWPD, the mag-

nitude of the reflection coefficient Γ becomes 0 and 1, respectively. In general Γ is complex with $0 \leq |\Gamma| \leq 1$. The following expression gives the forward travelling current contribution at the transmission line output:

$$I_n^f(\omega) = \frac{I_n}{2} \exp\Big[-i\omega(\Delta t(m-n))\Big] \tag{63}$$

The reflected backward travelling signal is:

$$I_n^b(\omega) = \frac{I_n}{2} \exp\Big[-i\omega\Big(t_e(n+m-2) + \frac{2\,d_{stub}}{v_0} - t_o(m-n)\Big)\Big] \tag{64}$$

with $\Delta t = t_e - t_o$. The time periods t_e and t_o are required by the electrical and optical signals, respectively, to travel between adjacent PDs, and are given by:

$$t_e = \frac{d}{v_0}\,, \quad t_o = \frac{d_o}{v_g^o} \tag{65}$$

From the RF current in equation 62 the power-related frequency response and the group delay due to phase mismatch can be evaluated.

Figure 27 shows the results for the unterminated (top) and terminated (bottom) TWPD with $m = 4$ and $v_g^o = 86\,\mu m/ps$. In the calculation dispersion is neglected and it is assumed that $d = d_o$, which is true for the serial-fed TWPD, and $I_1 = I_2 = \ldots = I_4$, which applies for parallel-fed TWPD. The photocurrents I_n were set to $I_{tot}/4$. For growing velocity mismatch v_0/v_g^o the unterminated TWPD exhibits a slightly growing bandwidth in the $50\,GHz$-range. As a result of the superposition of the forward and backward travelling wave local maxima in the response can be observed at higher frequencies, which reach the $0\,dB$-mark when velocity match is assumed. The group delay scatter is with $4\,ps$ considerably high.

The terminated TWPD exhibits a tremendously improved performance at the expense of a $6\,dB$ lower absolute output power. For velocity match, $v_0/v_g^o = 1$, it exhibits unlimited bandwidth and zero group delay scatter in the considered frequency range as long as any other effects are ignored. Even when allowing $v_0/v_g^o = 0.8$, the 3 dB-bandwidth reaches $400\,GHz$.

Figure 28 summarizes the calculated bandwidth results for the terminated and unterminated TWPD vs. electrical phase velocity normalized to $v_g^o = 86\,\mu m/ps$. A velocity match between 70% and 180% is required for the terminated TWPD in order

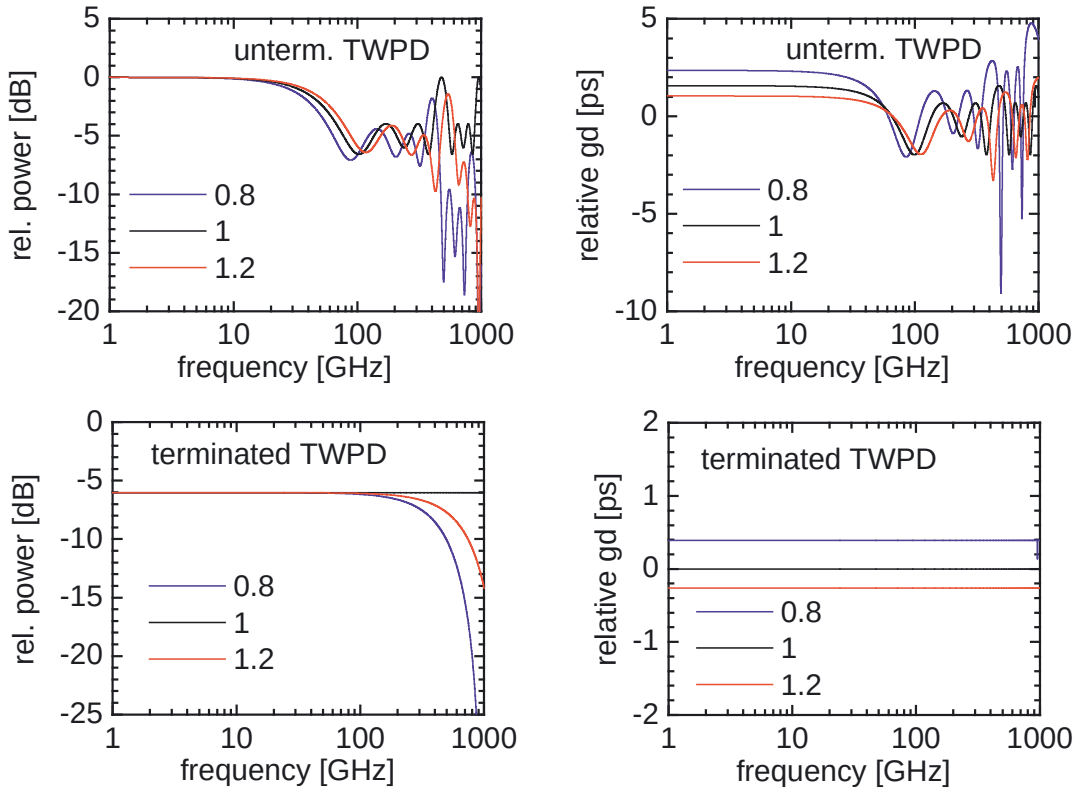

Figure 27: Left, calculated transfer functions due to velocity mismatch with $v_0/v_g^o = 0.8,\ 1,\ 1.2$ *for the unterminated (top) and terminated (below) TWPD with* $m = 4$ *and* $v_g^o = 86\,\mu m/ps$ *assuming* $d = d_o = 90\,\mu m$*, no dispersion,* $\alpha = 0$ *and* $d_{stub} = 0$*, right: relative group delay with same parameters.*

to achieve a bandwidth in excess of 200 GHz. The unterminated TWPD reaches maximum performance for $v_0 > v_g^o$. However, the maximum bandwidth is significantly limited by mismatch effects between the forward and reflected backward travelling wave and hardly reaches $100\,GHz$. One can show, that for both configurations the bandwidth decreases for a growing d and m, and in the case of the unterminated TWPD, for stub lengths $d_{stub} > 0$.

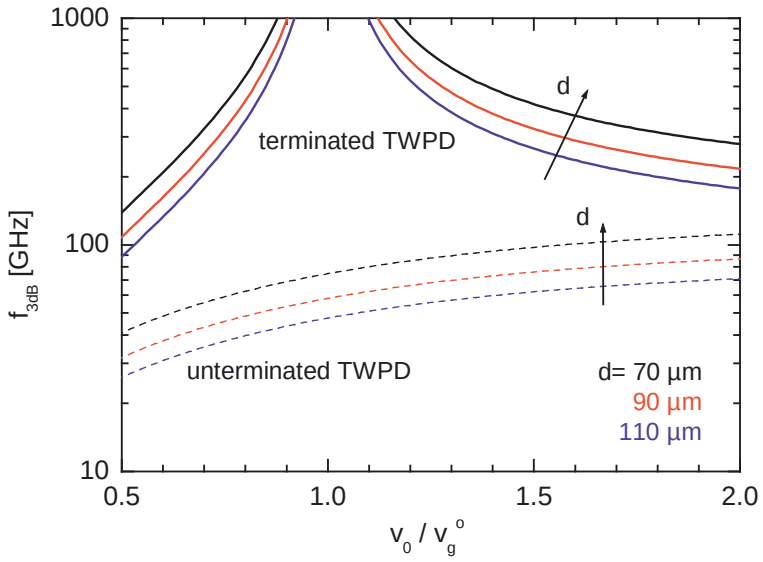

Figure 28: Calculated 3 dB bandwidth due to velocity mismatch v_0/v_g^o for the terminated (straight lines) and unterminated (dashed) TWPD for $d = d_o = 70\,\mu m$, $90\,\mu m$, $110\,\mu m$, $v_g^o = 86\,\mu m/ps$, no dispersion, $\alpha = 0$ and $d_{stub} = 0$.

3.5. Parallel optical feed

In the TWPD with parallel optical feed the input signal is split and distributed symmetrically to the discrete photodiodes (see fig.5b). By reasons of compactness, reliability and performance, a monolithic integration comprising the power splitter and the active device is superior to any hybrid solution. As a symmetric optical power divider the multimode interference splitter is beneficial, as it is easy to fabricate. Compared to Y-junctions, it has larger tolerances to variations implied by the fabrication process. Figure 29a depicts an MMI splitter as employed in a P-TWPD. The schematic shows the input waveguide, a 1×4 MMI splitter, and the output waveguides which feed the photodiodes. Figure 29b shows the cross sectional view of the MMI splitter which is derived from the singlemode waveguide in fig. 14a, but with a rib width $W_{MMI} > 2\,\mu m$, in order to support modes of higher lateral order.

The MMI dimensions (width: W_{MMI}, length: L_{MMI}) can be estimated by using the theory of self-imaging [67]. By knowing the effective indices of the two lowest order

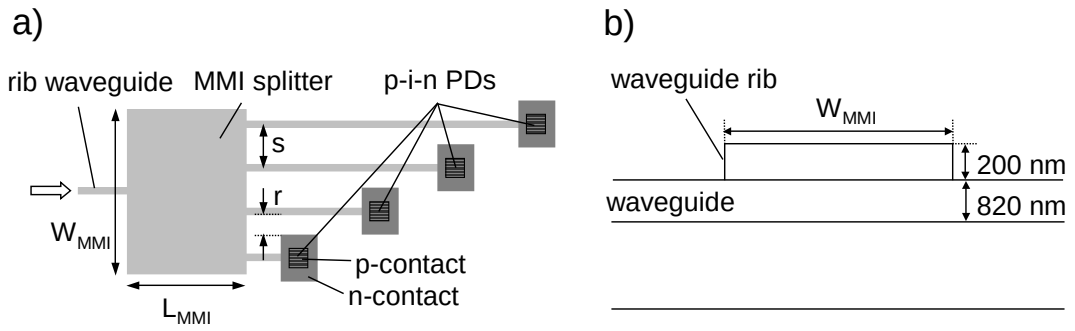

Figure 29: a) 1×4 *MMI splitter with feeding waveguide, output waveguides and photodiodes, b) cross sectional view of the MMI splitter.*

modes of the device $n_{eff}^{1,2}$, the beat length L_π given in eq. 44 can be calculated. N-fold images appear at the output of the MMI with length L_{MMI}:

$$L_{MMI} = \frac{p}{N} \cdot \frac{3\,L_\pi}{4} \tag{66}$$

with an odd number p and the splitting ratio N.

Using the cross sectional structure depicted in fig. 29b together with the layer sequence according to table 3, the required MMI length in dependence of the MMI width has been calculated. In fig. 30 L_{MMI} is plotted for $N = 4$ and $N = 8$ for the lowest orders $p = 1, 3, 5$. The bottom line refers to $p = 1$ and indicates the shortest distances from the feeding waveguide, where the manifold image appears. To keep the overall device size as small as possible $p = 1$ should be used. The minimum MMI width can be chosen with respect to the smallest allowed spacing between the centres of the straight output waveguides s (see fig. 29a). Simulations revealed that s should not fall below $4\,\mu m$ in order to prevent undesired inter-coupling between adjacent waveguides. This estimation was carried out for the waveguide with a rib of $2\,\mu m$ width and $200\,nm$ height from fig. 14a. In the practical design the spacing s has to be chosen larger as it is conditioned according to the required separation of $\geq 4\,\mu m$ between waveguide and n-mesa of adjacent photodiodes, denoted r in fig. 29a. These considerations lead to $s > 10.8\,\mu m$ and thus MMI widths of $> 43\,\mu m$ and $> 86\,\mu m$

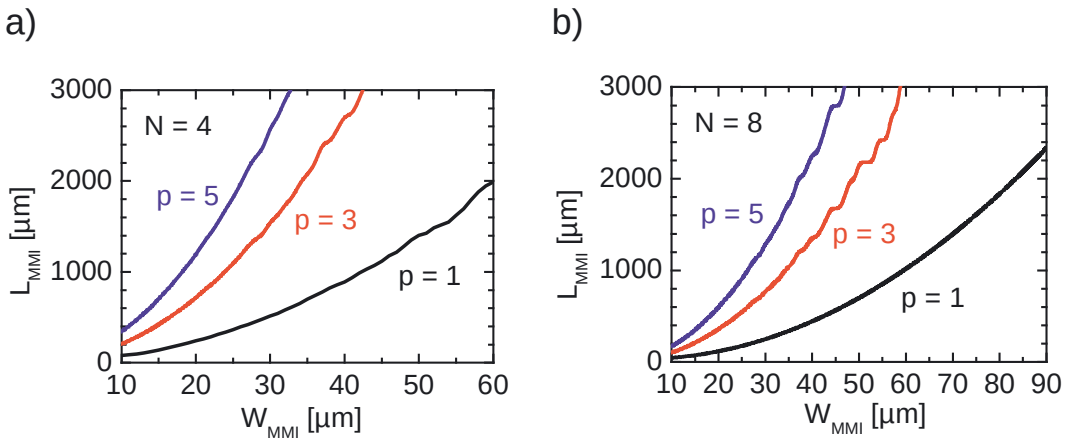

Figure 30: MMI length over width for fourfold (a) and eightfold (b) imaging of the first three orders p. The underlying waveguide structure is given in shown in fig. 29.

for $N = 4$ and $N = 8$, respectively. From fig. 30, the respective MMI lengths of $1030\,\mu m$ and $2090\,\mu m$ can be deduced.

The choice of the splitting ratio of the MMI complies with the desired performance of the entire TWPD. Obviously, a higher splitting ratio makes the chip dimensions larger. In terms of high-power saturation effects, the available unsaturated output current scales directly with the splitting ratio. However, by choosing a large ratio the output CPW becomes longer and the benefit of an increased unsaturated output power might be compensated by the higher transmission line losses. In the current design a 1×4 configuration was chosen which represents a compromise between high splitting ratio and acceptable chip area and transmission line losses.

Based on the above results, detailed device modelling was carried out by using a commercial software [49]. The design was verified in terms of minimized insertion loss and symmetric splitting ratio employing an iterative approach whereby the MMI dimensions were changed in each simulation run within some microns. The input and output waveguides with $2\,\mu m$ width were modelled as singlemode waveguides, while the multimode section was solved by use of 16 guided modes and 59 radiation modes. Figure 31a shows a top view of the simulated intensity profile (TE) of the 1×4 MMI splitter. In order to identify the optimum position of the output waveguides,

the transmitted intensity was scanned over the lateral offset at the end of the MMI (fig. 31b). For both states of polarizations the offset positions for maximum transmitted intensity coincide. The transmission is pairwise symmetric for the inner and outer waveguides and shows an imbalance of $0.2\,dB$. The waveguide separation was found to be $s = 11.25\,\mu m$

Figure 32a gives the simulated MMI excess loss and PDL versus L_{MMI}. At $L_{MMI} = 1038\,\mu m$ a minimum loss of $0.7\,dB$ and a PDL close to zero is calculated. A tolerance of $\pm 30\,\mu m$ can be determined when accepting $1\,dB$ loss. In contrast, the tolerances regarding the MMI width are more critical, as a similar analysis with varied W_{MMI} showed. Keeping all other parameters constant ($L_{MMI} = 1038\,\mu m$), a variation of $\pm 1\,\mu m$ led to an excess loss of $1.9\,dB$.

Between $\lambda = 1.52\,\mu m$ and $1.58\,\mu m$ the losses remain below $1\,dB$, which recommend this design for C-band operation (see fig. 32b).

Regarding the design of the photodiodes, the PDs are required to absorb all of the light available in the waveguide on a short length. Therefore the responsivity-enhanced PD

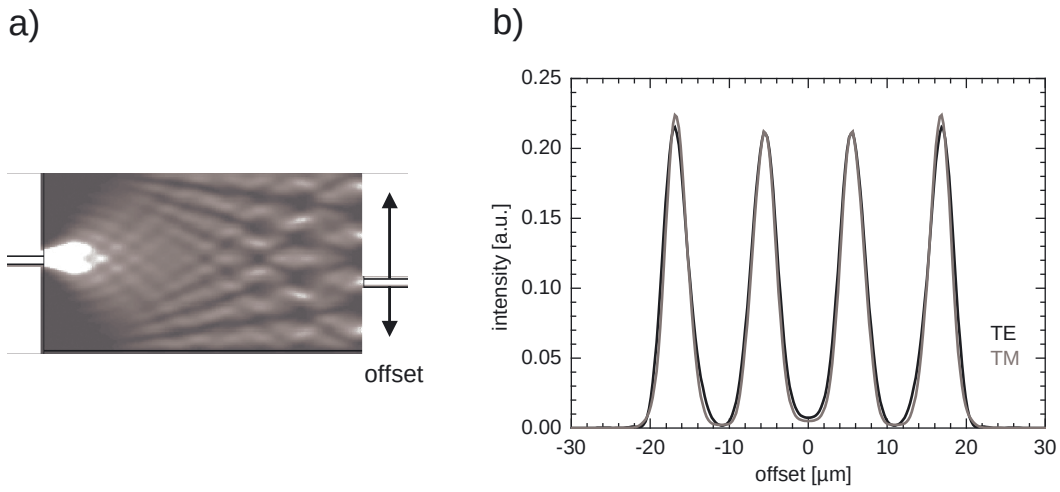

Figure 31: a) Top view of the calculated intensity distribution (TE) of a 1×4 MMI power splitter with $W_{MMI} = 43\,\mu m$, $L_{MMI} = 1038\,\mu m$ (not true to scale), b) transmitted intensity in dependence of lateral offset, see (a), for TE and TM polarization. MMI dimensions: $W_{MMI} = 43\,\mu m$, $L_{MMI} = 1038\,\mu m$.

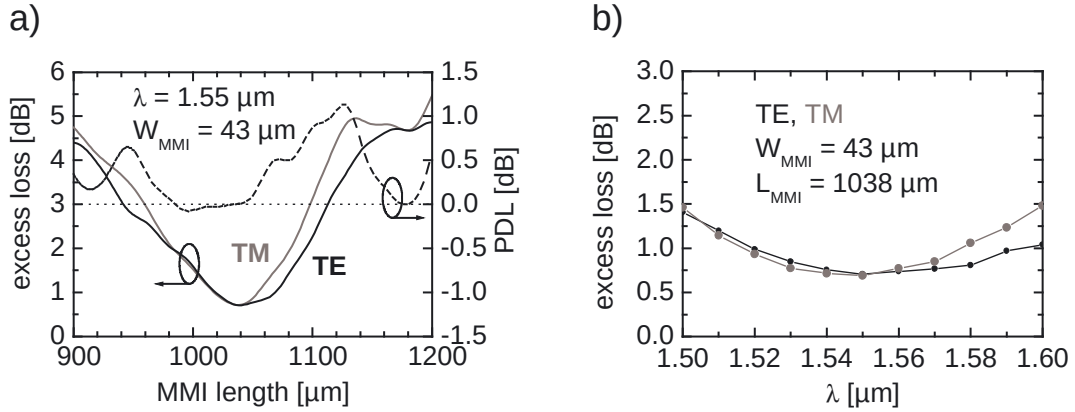

Figure 32: MMI ($W_{MMI} = 43\,\mu m$) excess loss and PDL vs. MMI length (a) and wavelength (b).

according to section 3.2.3 was adopted.

3.6. Serial optical feed

In contrast to the parallel-fed TWPD, the photodiodes in the S-TWPD are arranged in series on top of a single optical waveguide (compare fig. 5a). Since each photodiode absorbs only a fraction of the light propagating in the waveguide, the transmitted portion couples to the next detector region, and so on. Ideally, with a sufficient large number of photodiodes the light is completely absorbed at the end of the device and the responsivity and the linear photocurrent surpass those of a single photodiode. Hereby, the design of each single PD is required to exhibit a low radiation loss at its rear side.

The concept of exploiting mode beating effects in short multimode waveguides was introduced in section 3.2.3 and can also be applied to the S-TWPD. In contrast to the responsivity-enhanced single PD, the length of the resulting multimode region is now set to $2 \cdot L_\pi$ which ensures that the light couples into the active region and back to the waveguide. Therefore, the multimode waveguides (MM-WG) are located at the front and at the rear of each photodiode. In fig. 33 the lengths of the MM-WG are denoted L_1 and L_2.

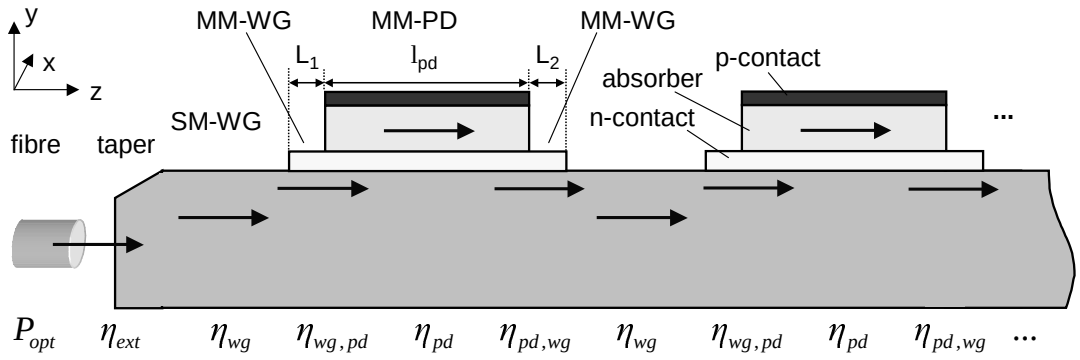

Figure 33: Schematic view of two sections of a serial-fed TWPD with spot-size converter. The corresponding coupling efficiencies η are described in the text.

Using the same waveguide structure as in table 3, the required overall length of the multimode waveguide sections can be estimated from the beat length of the two most prominent modes in the MM-WG (compare section 3.2.3):

$$2 \cdot L_\pi = 26\,\mu m = L_1 + L_{pd} + L_2 \tag{67}$$

The above result is only a rough approximation as the different waveguide sections MM-WG and MM-PD give rise to different L_π. For the MM-PD, one derives $2 \cdot L_\pi = 31\,\mu m$, when using the data of the modes TE_{12} and TE_{13} in table 4. Therefore the optimal resulting length can be estimated to be between 26 and $31\,\mu m$, but still under the assumption that all other modes are negligibly excited.
In order to specify the overall responsivity of the S-TWPD it is useful to describe the optical power in transmission in terms of optical coupling efficiencies. According to fig. 33 one obtains:

- η_{ext}: the external efficiency takes into account the fibre-chip coupling efficiency $\eta_{f,c}$ due to mode mismatch and Fresnel reflection as well as the taper efficiency η_t. Experimental results show $0.9 > \eta_{ext} > 0.7$ for TE and TM.

- η_{wg}: efficiency of the singlemode waveguide, in most cases $\eta_{wg} = 1$ is a valid approximation as long as short waveguides are used and free carrier absorp-

tion and scattering can be neglected. Experimental data for quaternary rib waveguides showed losses of $0.02\,dB/100\,\mu m$ [71].

- $\eta_{wg,pd}$: coupling efficiency between feeding waveguide and MM-PD.
- η_{pd}: transmittance of the active region taking two loss mechanisms into account: the desired absorption in the InGaAs layer (due to α_{eff}) and losses in the metal layer (α_m):

$$\eta_{pd} = exp\Big(- \int_0^{L_{pd}} (\alpha_{eff}(z) + \alpha_m(z))\, dz \Big) \tag{68}$$

  η_{pd} depends also on the state of polarization.
- $\eta_{pd,wg}$: coupling efficiency between the MM-PD and the waveguide.

Using the above definitions the overall DC responsivity of a S-TWPD consisting of n discrete photodiodes can be expressed by:

$$R = R_{ideal} \cdot \eta_{ext} \Big[\sum_{i=1}^{n} \eta_{wg}^{i} \cdot \eta_{wg,pd}^{i} \cdot \eta_{pd}^{i-1} \cdot \eta_{pd,wg}^{i-1} \Big] \cdot \Big[1 - exp\Big(- \int_0^{L_{pd}} \alpha_{eff}(z)\, dz \Big) \Big] \tag{69}$$

For practical calculations, the following simplifications are made: all efficiencies are independent of n, $\eta_{wg} = 1$ and $\eta_{ext} = 1$.
Then, by employing the simulative approach explained in section 3.2.2, the individual absorption in the PD $\eta_{wg,pd}(1 - exp[-\int_0^{L_{pd}} \alpha_{eff}(z)\, dz])$ as well as the product $(\eta_{wg,pd} \cdot \eta_{pd} \cdot \eta_{pd,wg})$ can be computed in dependance of L_1, L_{pd} and L_2 for a given waveguide structure.
The diagram in fig. 34 illustrates the simulation result of the overall responsivity in dependance of L_1 and L_2. The calculation was carried out for a S-TWPD comprising four photodiodes of fixed length $l_{pd} = 7\,\mu m$ with an underlying layer structure according to table 13 in appendix 7.1. A characteristic pattern can be observed which is attributed to the mode beating effects in the multimode regions.
In the device design two different optimization aims can be pursued: 1. maximization of the overall DC responsivity, or 2. maximization of the overall unsaturated output current by distributing the optical power uniformly to all PDs. Hence, the former

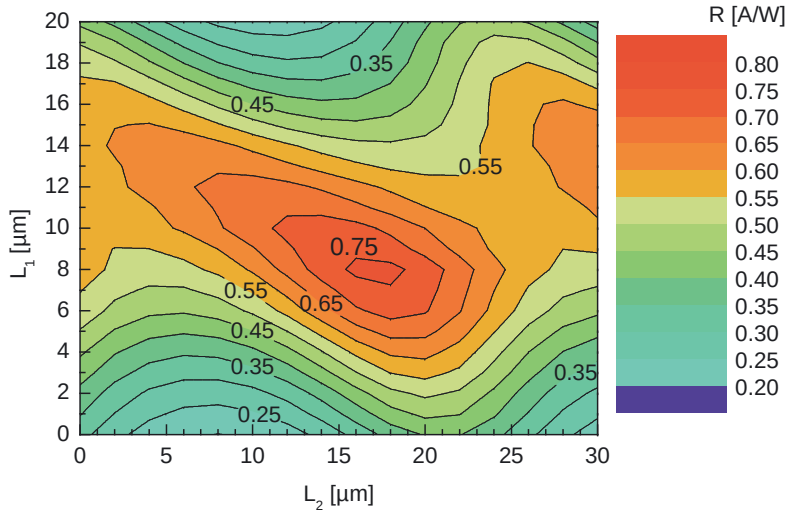

Figure 34: Simulated total responsivity of a S-TWPD comprising four PDs with $4 \times 7\,\mu m^2$ *active area* ($\eta_{ext} = 1$).

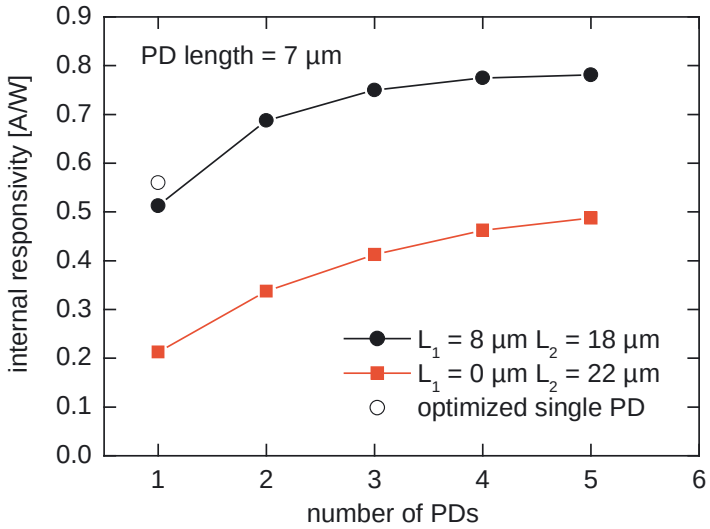

Figure 35: Responsivity of S-TWPDs, optimized for maximum efficiency (filled circles) and uniform current contribution (filled squares) for $\eta_{ext} = 1$. *The open circle represents a single PD with* $L = 7\,\mu m$.

optimizes the bandwidth-efficiency-product, while the latter increases the bandwidth-saturation-current-product.

In order to reach best responsivity-performance, the simulation result in fig. 34 reveals that MM-WG lengths of $L_1 = 8\,\mu m$ and $L_2 = 18\,\mu m$ lead to a responsivity in excess of $0.75\,A/W$ for $\eta_{ext} = 1$.
Regarding a S-TWPD without any MM-WG ($L_1 = L_2 = 0$), this value corresponds to an responsivity enhancement of a factor of > 2. An improvement of $1.5\,dB$ can be deduced by comparison with an optimized ($L_1 = 7\,\mu m$) single PD.
A detailed look at the internal current contribution is given in fig. 35, illustrated by filled circles. Here, the total responsivity is given in dependance of the number of PDs in the S-TWPD. One observes, that the first PD contributes mostly ($0.5\,A/W$) to the overall responsivity. A number of four PDs should be sufficient to reach adequate saturated efficiency. The second solution (filled squares) refers to a design with $L_1 = 0\,\mu m$ and $L_2 = 22\,\mu m$ and reveals a lower responsivity of $0.5\,A/W$. However, the slope is more linear which indicates a more uniform optical power distribution.

3.7. Equivalent circuit

In the previous sections some of the important high-frequency properties of the TWPD have been described individually. In this section, an equivalent circuit is developed which allows the prediction of the S-parameters and the complete transfer function in magnitude and phase of a TWPD for a given set of parameters. The model was developed using the simulator *Ansoft Designer SV* [68] and includes the following effects: carrier transit time, phase-and impedance match, transmission line properties, optical power distribution and electrical Bragg-reflections.
Figure 36 depicts the proposed circuit for a discretised TWPD comprising n photodiodes. The optical input signal is replaced by an ideal frequency-dependent current source $I(\omega)$. The transfer function due to carrier transit time effects according to eq. 26 is taken into account by two-port elements, denoted as H_t. The signal is distributed to the PD cells by means of current controlled current sources (CCCS). The latter can be used to model the relative time delay of the optical signal Δt_n, defined as

$$\Delta t_n = \frac{d_o}{v_g^o} \cdot (n-1) = \frac{d_o}{86\,\mu m/ps} \cdot (n-1) \tag{70}$$

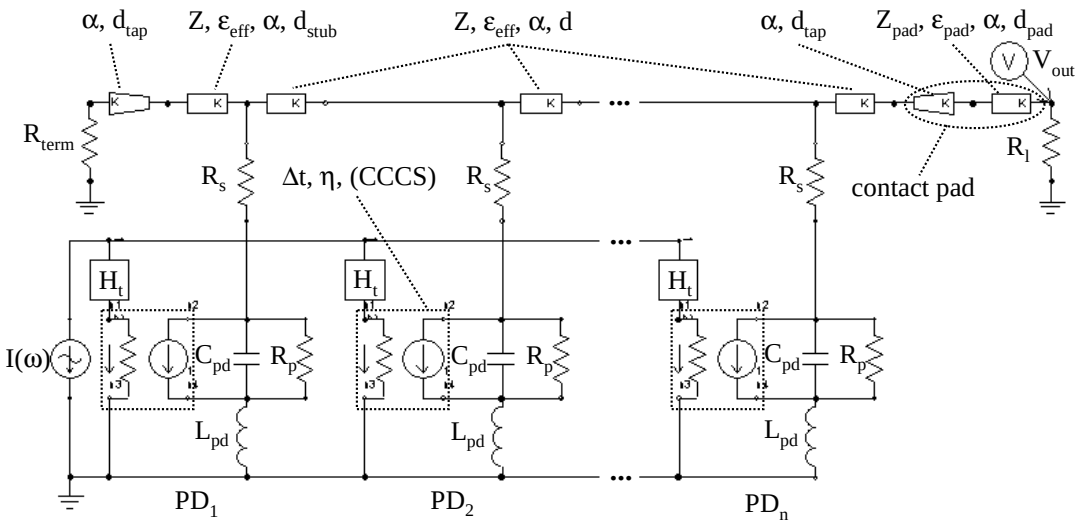

Figure 36: Discretised TWPD equivalent circuit.

and the DC quantum efficiency $\eta = R/R_{ideal}$ of each individual photodiode. In the case of the TWPD with parallel optical feed, the responsivities are set to be equal in a first estimation, while for the S-TWPD η differs according to the optical simulations in section 3.6. Each PD cell incorporates the equivalent circuit of a lumped PD consisting of RLC-elements (compare fig. 7). Neighboring cells are connected by a transmission line segment K which is characterized by its impedance Z, effective propagation constant ε_{eff} and length d. Furthermore, the attenuation constant α with a frequency dependence $\propto \sqrt{f}$ is used. These parameters are either deduced from the analytical formulas given in section 3.3 or can be extracted from S-parameter measurements of appropriate transmission line test structures. The contact pad with Z_{pad}, ε_{pad}, and d_{pad} is connected by a tapered transmission line (α, d_{tap}). Its properties are modelled by the simulator's built-in device, which employs a linear interpolation of the impedance and propagation constant between both nodes.

On the input side of the device, the TWPD is optionally terminated with a $50\,\Omega$-resistor R_{term}. The output voltage V_{out} is picked off at the external load resistor $R_l = 50\,\Omega$ and is converted to the equivalent electrical power. By taking only one

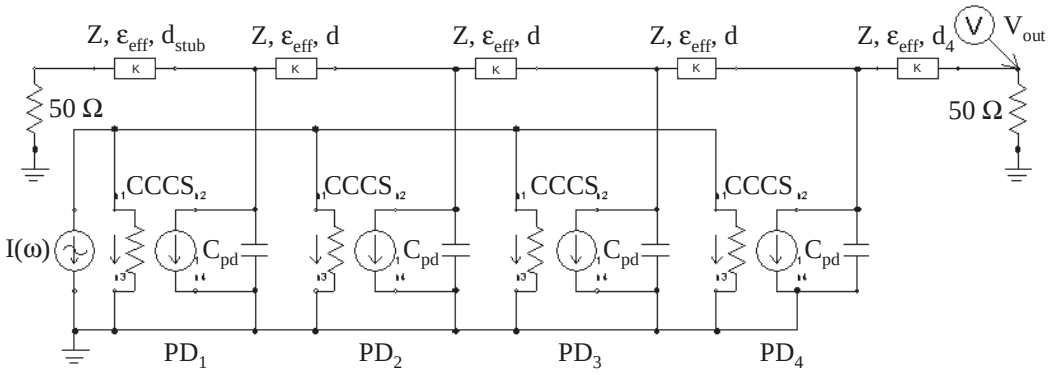

Figure 37: Simplified TWPD equivalent circuit.

section of the described circuit and omitting the CPW, the circuit represents a lumped element PD. Therefore, the model is well suited for simulating a wide range of different types of devices, in order to check the validity of the used parameters.
First, the influence of the Bragg-effect is studied.
In order to disregard all losses, parasitics and carrier transit effects, the equivalent circuit in fig. 36 can be reduced. Now, the circuit as shown in fig. 37 is used which consists of four ideal PD cells with $\eta = 1$ and $d_o = d$. The PD capacitance is assumed to be $17\,fF$, which corresponds to a $4 \times 7\,\mu m^2$-device with $200\,nm$ depletion width. Note, that the outermost TL section at the output side is now of length d_4. Impedance ($Z_0 = 50\,\Omega$) as well as phase match with the optical signal ($v_g^o = 86\,\mu m/ps$) are achieved in the simulation by appropriate choice of Z, v and d using eq. 57 and 50. It should be mentioned that the required CPW phase velocities are in part hardly feasible in a realistic TL design. All parameters used in the following simulation are listed in table 5. The solid lines in fig. 38a show the simulation results of three lossless terminated TWPDs with different CPW impedances $Z = (70, 90, 120)\,\Omega$, $d_{stub} = 0$ and $d_4 = d$. With growing Z, the Bragg-limit and therefore the bandwidth is expanded due to the decreased PD spacing d. The responses peak approximately at their Bragg-frequencies, $201\,GHz$, $266\,GHz$ and $303\,GHz$ for $Z = (70, 90, 120)\,\Omega$, respectively, and notable ripples are shown already at frequencies $\geq 0.5 \cdot f_{bragg}$. For comparison, the calculations with eq.56 yield $f_{bragg} = 184\,GHz$, $269\,GHz$ and $310\,GHz$. The marginal differences arise due to

the fact that two different types of equivalent circuit models, lumped element and

parameter	description	value
$Z\ [\Omega]$	CPW impedance	$70,\ 90,\ 120$
ε_{eff}	CPW effective dielectric constant	$6.16,\ 3.73,\ 2.09$
$v\ [\mu m/ps]$	CPW phase velocity	$121,\ 155,\ 207$
$C_{pd}\ [fF]$	PD capacitance	17
$d\ [\mu m]$	PD spacing on CPW	$149,\ 106,\ 88$
$x\ [fF/mm]$	effective loading	$114,\ 161,\ 192$
$d_{stub}\ [\mu m]$	stub length	$0,\ (d/2)$
$d_4\ [\mu m]$	CPW length	$d,\ (d/2)$
$\Delta t\ [ps]$	optical time delay	see eq. 70

Table 5: Parameters used in the reduced equivalent circuit in fig. 37.

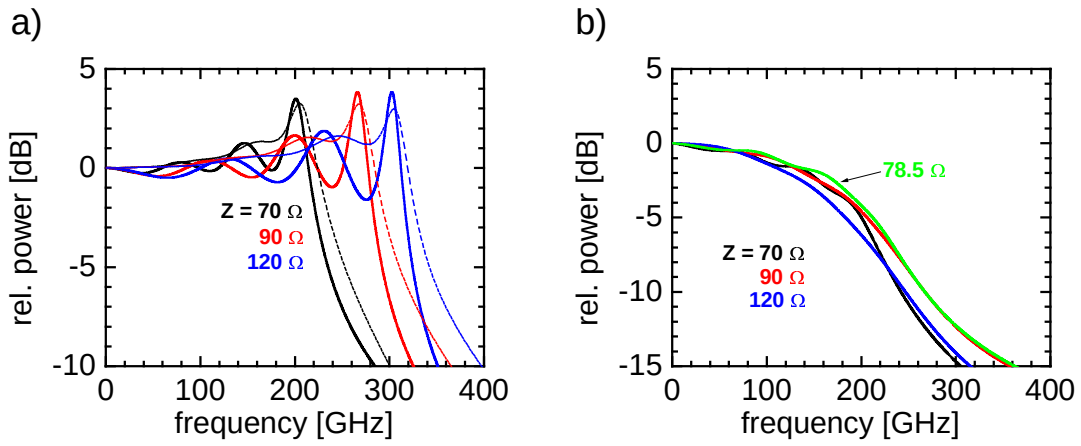

Figure 38: a) Relative power of lossless impedance- and phase-matched TWPDs with $d_{stub} = 0$ and $d_4 = d$ (solid lines) and $d_{stub} = d/2$ and $d_4 = d/2$ (dotted lines), parameters in table 5, b) relative responses with $d_{stub} = 0$ and $d_4 = d$, now including phase mismatch effects, losses and parasitic effects, parameters in table 6. The carrier transit time effects are ignored in all calculations.

transmission line are compared. The maximum achievable Bragg-frequency amounts to $374\,GHz$ and requires $d = 74\,\mu m$ (see eq. 60).
By setting $d_{stub} = d/2$ and $d_4 = d/2$ a symmetric network, based on T-circuit elements, is obtained. Keeping all other parameters as in the previous simulation, the results of the corresponding calculation are displayed as dotted lines in fig. 38a. For high frequencies approaching f_{bragg}, the symmetric network evidently leads to less ripple in the response when compared to the previous results obtained for $d_{stub} = 0$ and $d_4 = d$ (solid lines). However, only minor deviations $< 1\,dB$ can be observed up to frequencies of $150\,GHz$ in this example.
In fig. 38b, a similar simulation of terminated TWPDs with $n = 4$ is shown, but now including losses and parasitic effects employing the circuit in fig. 36. Again, the carrier transit effects are ignored. In order to describe more practicable devices the impedances and effective dielectric constants of the unloaded CPW calculated in section 3.3 are utilized. For $Z = (70, 90, 120)\,\Omega$ one determines $G = (7.3, 27, 125)\,\mu m$ for $W = 4\,\mu m$, $t = 3\,\mu m$, $h_1 = 500\,\mu m$ (InP) and $h_2 = 2\,\mu m$ (BCB). The resulting effective dielectric constants as well as the required lengths d are listed in table 6. The CPW losses given at $100\,GHz$ were determined using the model in [57]. The results show, that generally an impedance and phase match can hardly be achieved at the same time, with feasible CPW dimensions. In the example, impedance match ($Z_0 = 50\,\Omega$) according to eq. 54 is achieved, however, the resulting velocity mismatches amount to 1.22, 0.83 and 0.59 for the (unloaded) CPW impedances $Z = 70\,\Omega$, $90\,\Omega$ and $120\,\Omega$, respectively. All other simulation parameters can be found in table 6. The inductance $L_{pd} = 5\,pH$ comes from short interconnections to the PD's n-contact. The total series resistance R_s takes the following contributions into account: p-contact resistance, n-contact resistance and bulk resistances and was set to $15\,\Omega$ according to previous results from S_{22}-based parameter extraction.
As regards to the 3 dB bandwidth, the responses for $Z = 70\,\Omega$ and $Z = 90\,\Omega$ exhibit $166\,GHz$ and $170\,GHz$, respectively, while the $120\,\Omega$-device reaches only $150\,GHz$, which is mainly due to the large phase mismatch.
For $Z = 78.5\,\Omega$, $\varepsilon_{eff} = 4.89$ and $d = 125\,\mu m$, eq. 54 predicts impedance and phase match. Therefore a CPW with $G = 12.5\,\mu m$ is required. The corresponding simulation result is illustrated by the green line in fig. 38b and shows the highest 3 dB

parameter	description	value
$Z\ [\Omega]$	CPW impedance	$70,\ 78.5,\ 90,\ 120$
ε_{eff}	CPW effective dielectric constant	$4.19,\ 4.89,\ 5.45,\ 6.03$
$\alpha\ [dB/mm]$	CPW attenuation at 100 GHz	$0.74,\ 0.57,\ 0.42,\ 0.28$
$C_{pd}\ [fF]$	PD capacitance	17
$R_p\ [M\Omega]$	parallel resistance	100
$R_s\ [\Omega]$	series resistance	15
$L_{pd}\ [pH]$	series inductance	5
$d\ [\mu m]$	PD spacing on CPW	$182,\ 125,\ 88,\ 53$
$d_{pad}\ [\mu m]$	pad length	80
$d_{tap}\ [\mu m]$	CPW taper length	50
$d_{stub}\ [\mu m]$	stub length	10
$Z_{pad}\ [\Omega]$	pad impedance	50
ε_{pad}	pad effective dielectric constant	5.9
$R_{term}\ [\Omega]$	termination resistor	50 (if applicable)
$R_l\ [\Omega]$	load resistor	50
$\Delta t\ [ps]$	optical time delay	$2.12,\ 1.453,\ 1.02,\ 0.62$

Table 6: Parameters used in the equivalent circuit in fig. 36.

bandwidth being $181\,GHz$.

In fig. 39, the bandwidth simulation results of P-TWPDs for various d in dependance of the depletion width are shown. Here, the carrier transit effects are included. The TWPDs comprise $n = 4$ identical PDs with an active area of $4 \times 7\mu m^2$. The parameters used in the simulation match with those in table 6 for $Z = 78.5\,\Omega$ and $\varepsilon_{eff} = 4.89$. For depletion widths around $200\,nm$ maximum bandwidths up to $117\,GHz$ can be observed for the considered CPW design. As the curve with the largest d shows the highest bandwidth, a dominant impact of the Bragg effect is not yet visible. For all d applies that for larger d_{pn} the response is transit time-limited, while smaller depletion widths lead to an increased PD capacitance and therefore to an impedance and phase mismatch. The unterminated TWPD reaches a bandwidth of $50\,GHz$ for the shortest

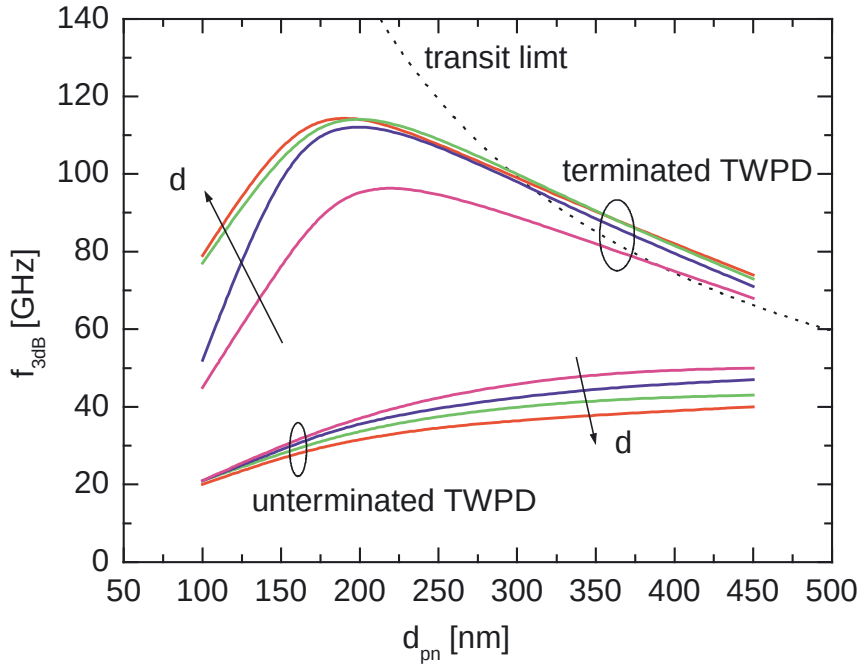

Figure 39: 3 dB bandwidth versus depletion width for terminated and unterminated TWPDs with PD spacings $d = (75, 100, 125, 150)\,\mu m$*, all with* $d_o = d$*,* $\eta = 1$*,* $Z = 78.5\,\Omega$ *and* $\varepsilon_{eff} = 4.89$*.*

PD spacing $d = 75\mu m$, which indicates that the response is mainly limited by phase mismatch effects.

3.8. Summary

In order to achieve an optimum performance of a TWPD, the results of the preceding chapter can be summarized as follows:

1. The overall RC-bandwidth limitation of a TWPD can be overcome by distributing the RC-elements on a appropriate high-impedance transmission line. Due to the capacitive loading, the characteristic impedance decreases and can be matched to that of the output load.

2. In-phase summation of the electrical signals is achieved by integrating a ter-

mination resistor at the transmission line's input, and phase matching of the electrical and optical signal.

3. The bandwidth of an impedance and phase matched TWPD is restrained by the carrier transit time limit and Bragg-frequency. The maximum Bragg-frequency is limited by twice the RC-bandwidth of the lumped element PD which is comprised in the TWPD.

4. Therefore the discretised TWPD should be based on PDs with low RC-constant.

5. The optical design derives benefits from mode-beating effects introduced by multimode waveguides. An enhancement of the responsivity can be achieved in the case of the P-TWPD, where the PDs are required to absorb all light in the waveguide as well as in the S-TWPD, where the radiation loss at the rear of each PD has to be minimized.

6. Assuming an impedance- and phase-matched TWPD, the simulations predict a 3 dB bandwidth of $115\,GHz$ for $d_{abs} = 200\,nm$, which is mainly limited due to the carrier transit times ($f_t = 150\,GHz$) and parasitic effects (series resistance R_s, CPW losses). For $\eta_{ext} = 0.75$, the calculated responsivity reaches $0.56\,A/W$ and $0.37\,A/W$ for the S-TWPD and P-TWPD, respectively.

4. Device design and fabrication

4.1. Device layout and epitaxial layer structure

The chip architecture of the travelling wave photodetectors with serial and parallel optical feed are depicted in figure 40a and (b).

In the S-TWPD, four miniaturized waveguide-integrated PDs, each with an active area of $4 \times 7\,\mu m^2$, are located on top of the rib waveguide, as previously described in section 3.2.2. The lengths of the multimode waveguides were selected to be $8\,\mu m$ at the front and $18\,\mu m$ at the rear of each PD, for a maximized total responsivity (see fig. 33). The CPW transmission line with a termination resistor at its input connects the PDs in parallel and provides the electrical output signal via a short CPW taper to the output pad. Thereby, the anode and the cathode are connected by the signal line and CPW grounds, respectively. The signal line width was minimised to $4\,\mu m$, which represents to date the lower limit for feasible metallization widths (metal thickness $\sim 3\mu m$). Three different gap widths G ($= 16\,\mu m, 22\,\mu m, 28\,\mu m$) and three PD spacings d ($=70\,\mu m, 90\,\mu m, 110\,\mu m$) have been realised. With these CPW geometries,

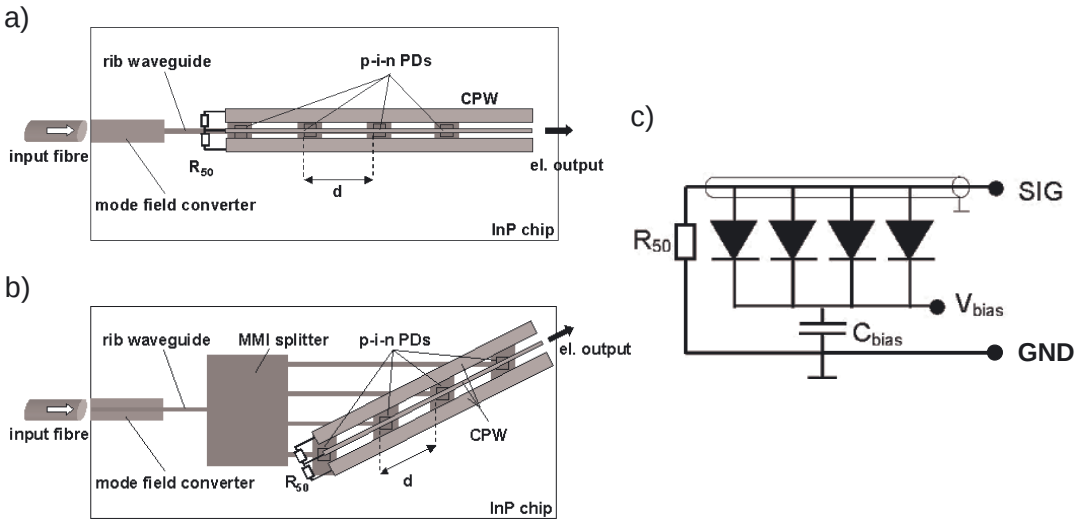

Figure 40: a) Schematic chip architecture of S-TWPD, b) P-TWPD and c) bias circuit, which is integrated on chip.

effective loading factors x of $100\,fF/mm$ up to $150\,fF/mm$ can be compensated, which in this case are equivalent to PD depletion widths of $430\,nm$ to $200\,nm$.
The P-TWPD in fig. 40b comprises a 1×4 MMI splitter (width: $43\,\mu m$, length: $1038\,\mu m$) of which singlemode output waveguides feed the four photodiodes. The output waveguide separation s amounts to $11.25\,\mu m$ due to a required separation between the waveguide and n-mesa of adjacent photodiodes (see section 3.5, fig. 29). The $4 \times 7\,\mu m^2$-PDs were optimized in terms of their front side multimode waveguide ($L = 7\,\mu m$) to provide a high responsivity.
In the current design the electrical output pads are placed almost in line (off-axis angle: $\alpha = 5°$) with the optical input. Hence, the electrical and optical paths between adjacent PDs have an almost identical length and a phase match is achieved by equalizing the optical and electrical signal velocities. This arrangement complies with the measurement setup and allows for a more satisfactory comparability with TWPDs with serial optical feed, where $d \equiv d_o$. Generally, α as a free parameter enables $d > d_o$, which may be beneficial in some specific designs.
Both types of TWPDs have an integrated biasing circuit on chip for convenient bias supply. In order to decouple the bias voltage from RF ground and to avoid the short-circuit current at the termination resistor, metal-insulator-metal (MIM) capacitors were implemented on the device. Figure 40c depicts the resulting circuit, which allows operation without external bias-tee in the RF path. The upper plate of the parallel-plate capacitor forms the RF ground line.
The above described TWPDs were also realised without termination resistor. All types of TWPD contain an optical mode field transformer which provides a nearly adiabatical transition from the circular spot of the cleaved input fibre to the much smaller optical field distribution in the rib waveguide. The mode field transformer is vertically tapered with a ramp of less than $1\,\mu m$ height over a length of approximately $1\,mm$ (see fig. 41a). Thus the fibre alignment tolerances are increased by one order of magnitude into the 2-micron range and the use of a cleaved, instead of a lensed fibre, is possible. Further details about the mode field transformer can be found in [24].
Apart from the TWPDs, a number of lumped element photodetectors of various active areas have been realised on the same wafer for reference measurements. These

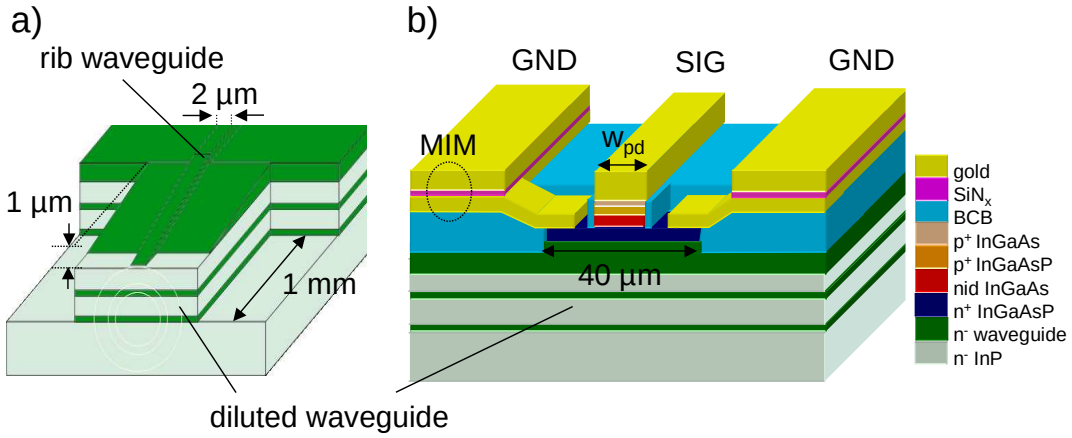

Figure 41: a) Schematic of the mode field transformer, b) schematic cross-sectional view of the TWPD.

include μ-PDs with different multimode waveguide lengths [76], PDs with optimized electrode configuration exploiting distributed RLC-effects [44] as well as large area photodiodes. Furthermore, test structures with MMI length variations and S-TWPDs with disconnected transmission lines for responsivity measurements of the individual PDs were implemented. Unloaded transmission lines of $150\,\mu m$ and $300\,\mu m$ length permit the determination of the electrical properties by 2-port characterization. Together with test devices for process control (TLM structures, NiCr resistors, MIM capacitors), the devices above were implemented on a novel mask set denoted *TWPD*. The device layouts were transferred by the *Mentor Graphics, Cadence Design Systems* CAD software. The generated mask set is comprised of 16 individual masks, which were fabricated by electron beam lithography.

Three different epitaxial layer structures have been investigated in this work. The corresponding layer sequences are given in table 3 and in the appendix 7.1 in tables 13 and 14 and are designated as TWPD#2, TWPD#4 and #5. All of them share the same underlying waveguide layer stack, based on a semi-insulating quaternary/InP sequence on InP:Fe substrate, which was adopted from well-established previous runs [24]. While the diluted waveguide for the mode field transformer is composed of thin quaternary guiding layers embedded within InP, the upper (rib-) waveguide is formed

by a $820\,nm$ thick quaternary layer and feeds the photodiode. The active region mainly consists of the following stack: a highly doped quaternary n-contact layer with $\lambda_g = 1.33\,\mu m$ which is expanded by an intrinsic portion (drift layer) in case of the dual depletion PD, the not intentionally doped ternary absorber, the p-type cladding with a larger bandgap ($\lambda_g = 1.15\,\mu m$) and the highly doped ternary p-contact. Additionally, on the p-side, thin grading layers are inserted to smooth valence band discontinuities. A schematic cross-sectional view of the TWPD is given in fig. 41b.
The three structures differ in their absorber thickness and intrinsic layer thickness. As TWPD#2 is based on a proven layer sequence and contains an undoped $430\,nm$-absorber, the absorber thickness of #4 is decreased to $200\,nm$, which leads to an expanded transit time limited bandwidth of $150\,GHz$. In return the thicknesses of the n-layer and the cladding are optimized in order to roughly maintain the total optical thickness of the p-i-n mesa and ensure evanescent field coupling. Thereby the simulative approach in section 3.2.2 was used to estimate responsivity and PDL. However, the reduction of the absorber thickness to $200\,nm$ leads, independently of the PD length, roughly to a 25 % decrease in responsivity, compared to an absorber thickness of $430\,nm$. This behavior can be attributed to a general decrease in the individual mode confinement factors, in view of the fact that the number of supported modes in the active region remains unchanged.
The design of TWPD#5 includes a novel type of dual depletion region, which is formed by an additional undoped quaternary layer with $\lambda_g = 1.33\,\mu m$ between absorber and n-contact. Hereby, the absorber and drift layer thicknesses amount to $200\,nm$ and $150\,nm$, respectively, with $d_{drift}/d_{abs} = 0.75$. With this design, the capacitance is reduced by 43%, while the transit time-limited bandwidth decreases by only 24%. Due to its reduced pn-capacitance, this structure is primarily intended to compensate for occurring stray capacitances ($5 - 10\,fF$) of the TWPD, which have not been accounted for in the device modelling and design.

4.2. Fabrication process

The subsequent section describes the substantial steps of the fabrication flow, which is based essentially on an established process of waveguide-integrated photodetectors

for $40\,Gbit/s$ applications. Besides of the numerous measures taken in order to fabricate the smallest of active devices, the introduction of the BCB layer was a major contribution.

In the following, the numbering of the process steps refers to the summary of the process sequence as given in appendix 7.5 with the underlying epitaxial layer structure of table 3. The fabrication commences with the growth of the ternary/quaternary layer stack on semi-insulating InP:Fe substrate (2 inch wafer) in a single metal organic vapor phase epitaxy (MOVPE) run. The semi-insulating waveguide layers are composed of three quaternary optical guiding layers embedded within InP, forming a diluted waveguide for the mode field converter and an upper thicker waveguide layer which feeds the photodiode. The InGaAs/InGaAsP heterostructure photodiode is grown on-top of this stack. Zn-diffusion (1) is applied to increase the p-type contact layer doping level from $10^{19}\,cm^{-3}$ to some $10^{19}\,cm^{-3}$ to assure a low contact resistance. Then the p-contact metal is evaporated and patterned by a lift-off process (2). The active photodiode volume is defined by reactive ion etching (RIE) and wet chemical etching down to the n-contact layer using the p-contact as a mask (3). Next, the n-contact is defined (4,5). The mode field transformer is formed by a vertically tapered ramp with a maximum height of $1\,\mu m$ and a length of $1000\,\mu m$ (6). Thereby, a lithographical image of the desired ramp in photoresist is created. This resist ramp is produced by shifting a mask with a window during the exposure cycle [69]. Finally, the resist ramp is transferred into the waveguide by ion beam etching. Then, the waveguides are formed by dry etching (7,8). For passivation, a layer of Benzocyclobuten is spun on the entire wafer, which is removed partly by dry etching to make p- and n-contacts accessible and to uncover the mode field transformer (9). The resulting BCB thickness amounts to $\approx 1.5\,\mu m$. The NiCr resistors, MIM capacitors, and the metallization for interconnections are subsequently processed on BCB (10-15). After cleaving (16), an anti-reflection coating (ARC) is deposited on the chip's facet (17). In fig. 42 and 43 micrographs of some fabricated photodetectors and test devices are shown.

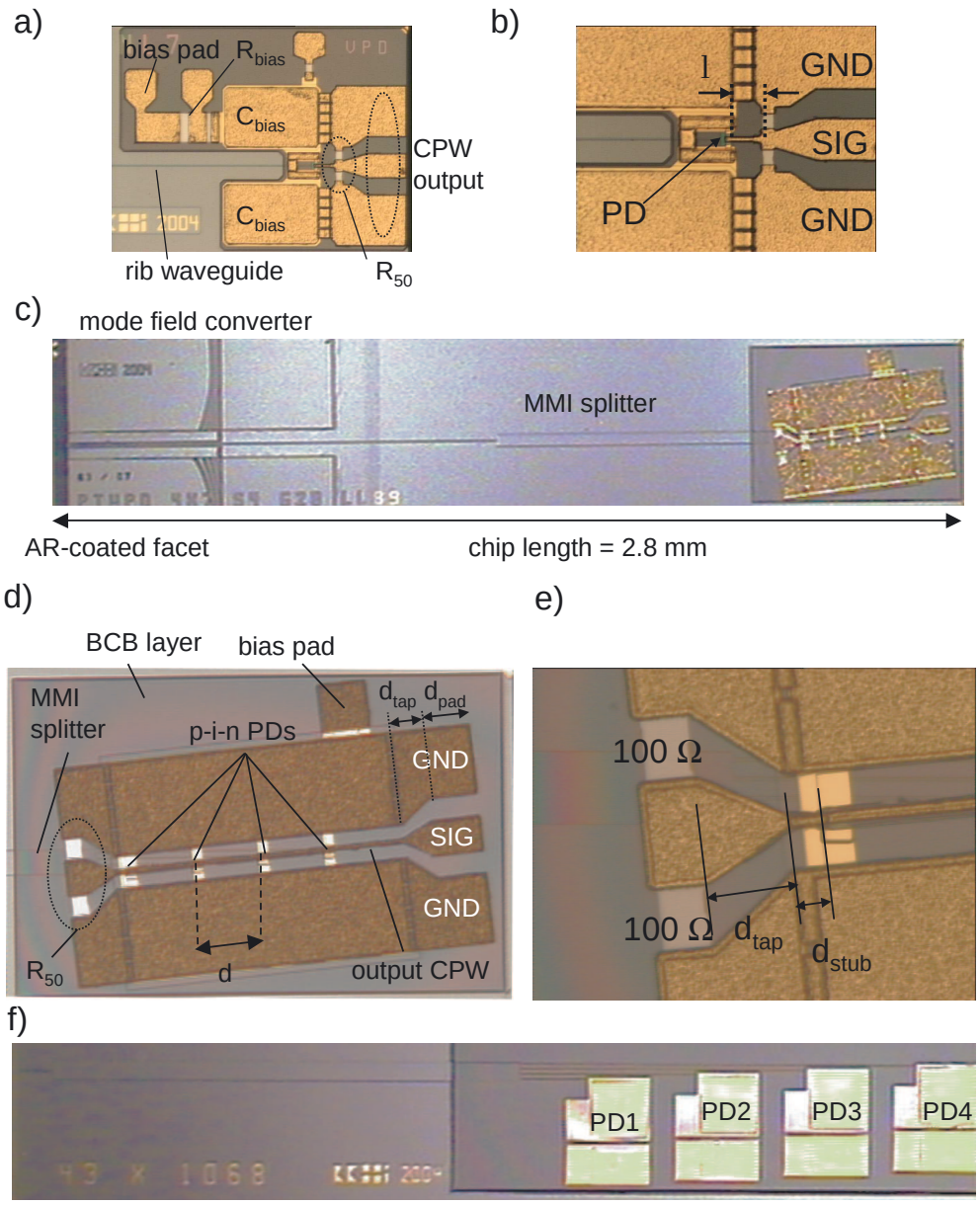

Figure 42: Micrographs of fabricated photodetectors and test device, a) lumped element $5 \times 7\,\mu m^2$ photodetector, b) detail view of picture (a), indicating the air bridge which connects the metal p-contact with the signal line with length $l = 30\,\mu m$, c) complete P-TWPD chip, d) active part of P-TWPD with $d = 90\,\mu m$, e) detail view of (d), showing the termination resistor and first PD, f) MMI test structure with four large area PDs.

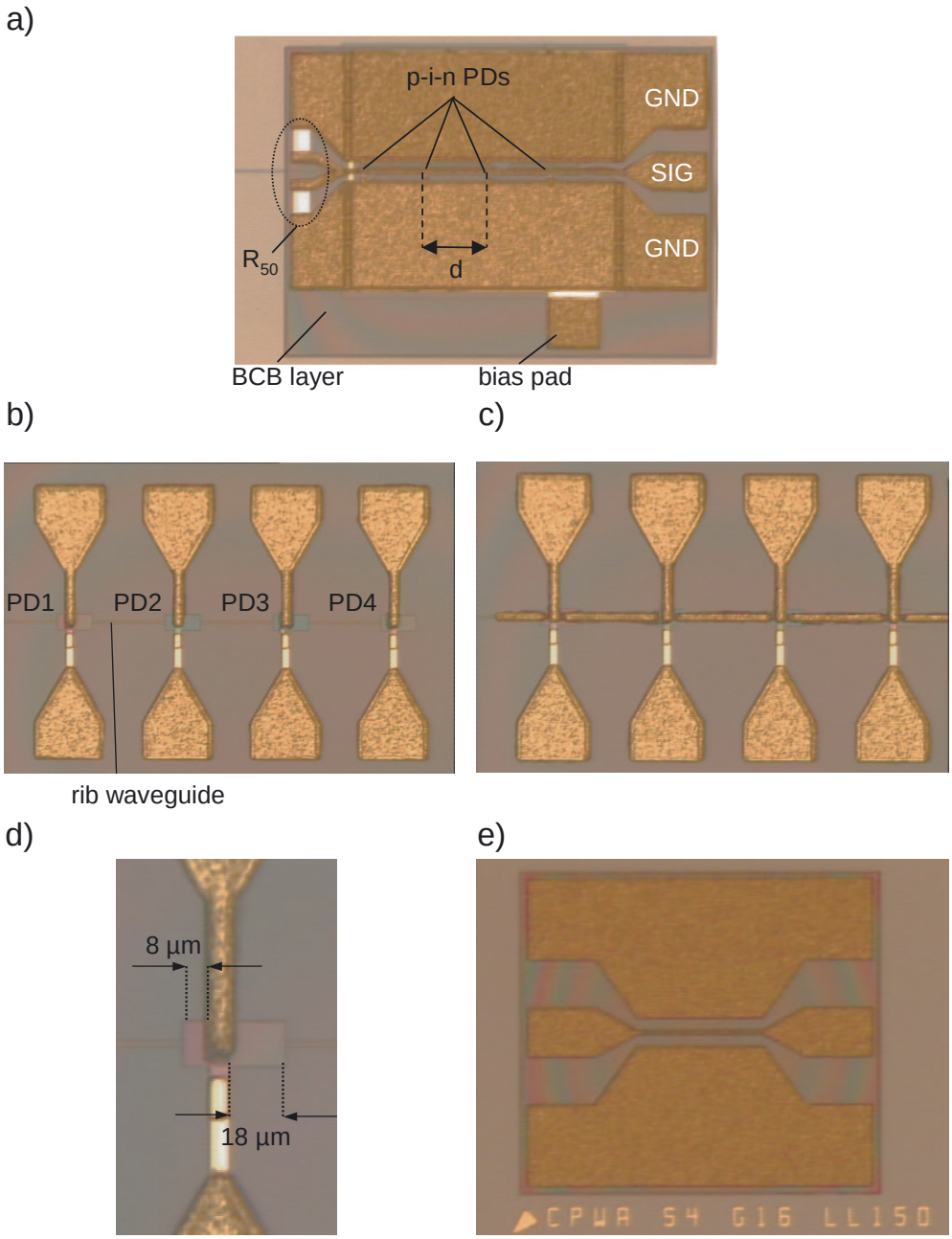

Figure 43: Micrographs of a fabricated S-TWPD and test devices, a) active part of S-TWPD with $d = 90\,\mu m$, b) S-TWPD without TL for determination of the individual photocurrent contributions, c) same device but with the optical waveguide loaded by a disconnected TL, d) detailed view of (b) indicating the multimode waveguide sections, e) CPW transmission line test structure which allows a 2-port characterization.

5. Device characterization

5.1. Current-voltage, responsivity and PDL

The measurement of the I-V characteristics represents the most straightforward test to check a diodes's functional capability. Thereby a voltage-sweep is applied to the photodiode's anode and cathode while the current is measured. Using on-wafer measurement techniques, a Keithley 2400 was employed as a voltage source and amperemeter. Probe needles were used to contact the photodiode's electrodes. The filled circles in the diagram of fig. 44 show a typical I-V curve of a TWPD from wafer #2 without illumination. For clarification, the absolute current is plotted on a log-scale. From the forward current, an ideality factor of 1.8 can be determined, which indicates a predominance of the recombination current. For reverse bias, the leakage current increases slightly to $3\,nA$ at $-3\,V$. From large area test devices one determines a current density of $1.2 \cdot 10^{-3}\,A/cm^2$, which suggests, that surface leakage currents contribute mostly to the observed dark current of the TWPD. TWPDs from wafer #4 and #5 showed substantially higher dark currents in the order of $2.5\,\mu A$ and

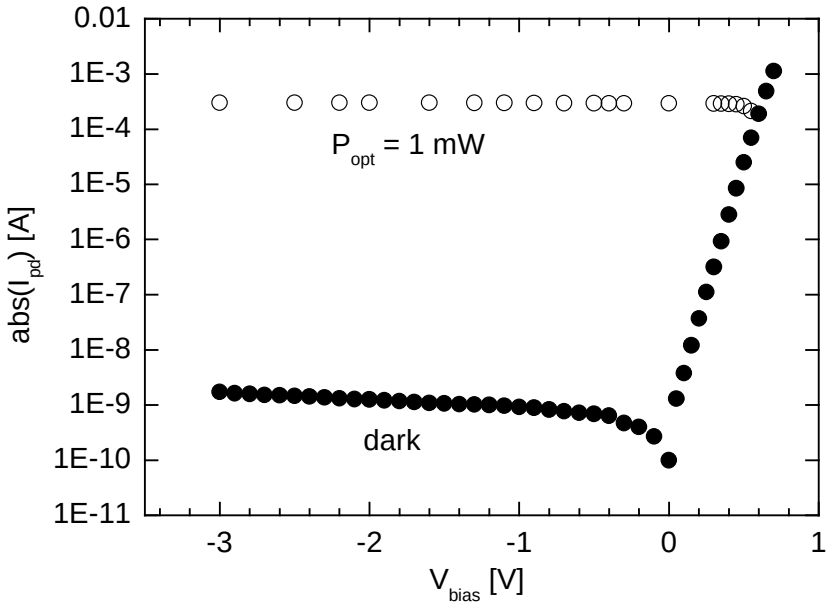

Figure 44: I-V characteristics of a TWPD in darkness and under illumination.

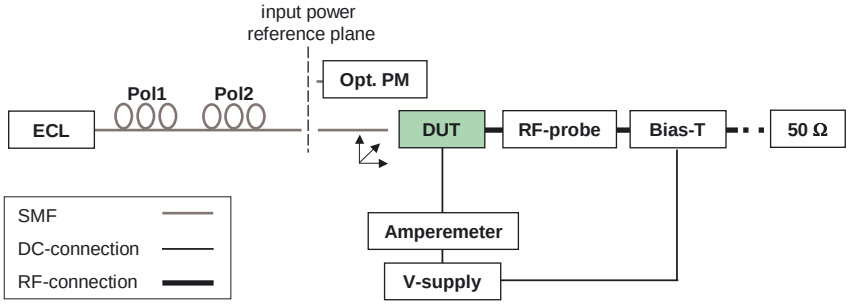

Figure 45: Experimental setup for optoelectronic continuous wave (CW) measurements.

$10\,\mu A$, respectively. While large area photodiodes without transmission lines, biasing-networks and contact pads from these wafers once more exhibited low dark current densities comparable to $\#2$, an increased bulk current did not seem responsible for the observed leakage currents. For this reason, one can attribute the leakage current in the case of the TWPDs to an increased surface conductivity due to some process irregularities.

Figure 45 depicts the experimental setup for measurements under illumination. An external cavity laser operating at $1.55\,\mu m$ was used as an optical source. After passing two polarization scramblers, the optical input signal is fed into the chip's tapered waveguide by a cleaved standard singlemode fibre (SMF). Depending on which device is under test, probe needles or a high-frequency probe were used for contacting the photodetector's electrodes. The photocurrent was determined at the bias terminal of the photodetector. As confirmed by the open circles in fig. 44, the TWPD exhibits a nearly constant photocurrent over reverse bias at a moderate optical input power of $1\,mW$. In the following responsivity measurements, R is calculated by dividing the photocurrent by the optical power, after subtracting the dark current. The responsivity refers to a fixed external bias voltage of $-2\,V$ and an optical power of $+2.3\,dBm$. The incident power is about $0.2\,dB$ lower, due to an uncorrected fibre connector in the optical path. Therefore, the indicated chip-based responsivity is somewhat underestimated and describes more the responsivity available in a fibre-pigtailed assembled module.

The results of the P-TWPD and the corresponding test structure are discussed first. The latter was designed to identify the optimum length of the MMI and its splitting symmetry. The test device contains an MMI splitter and four photodiodes (PD1 to PD4), each with an active area of $50 \times 150\,\mu m^2$ (compare fig.42 d). In order to determine the MMI excess loss, the photocurrent of each photodiode was measured separately and its responsivity was related to the responsivity of a reference PD of the same length without MMI splitter. The diagram in fig. 46a illustrates the simulated and measured minimum responsivity excess loss deduced for an optimum state of polarization in dependence of the MMI length. In agreement with theoretical expectations, a pairwise symmetric excess loss between the inner (PD2, PD3) and outer (PD1, PD4) photodiodes was predominantly achieved. A minimum insertion loss was measured for lengths of $1038\,\mu m$, exhibiting a high symmetry of all output photocurrents in good accordance with the simulation. With respect to MMI lengths $> 1048\,\mu m$, the differences between the inner and outer PDs increase slightly.
In fig. 46b the total MMI excess loss is given. The experimental data were obtained by

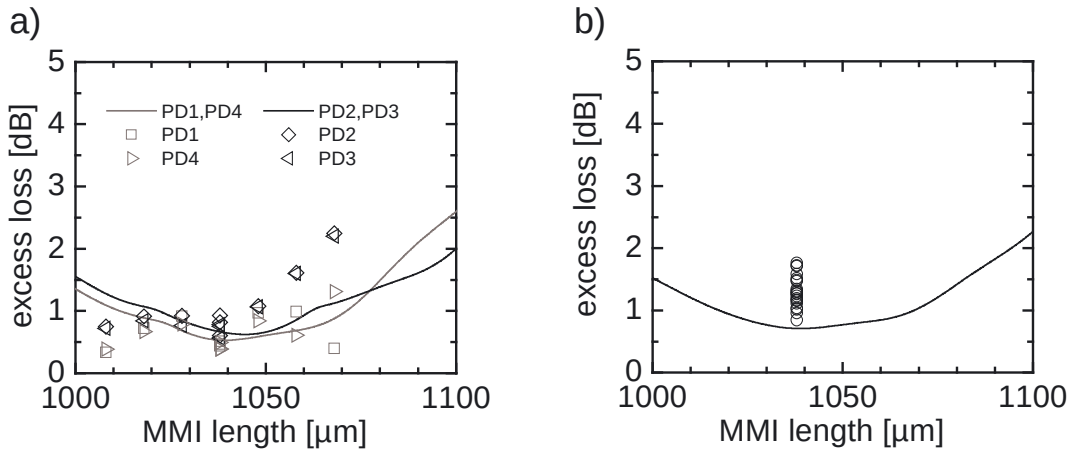

Figure 46: a) Calculated (lines) and measured (symbols) minimum individual PD excess loss vs. MMI length of all four photodiodes. Due to the MMIs symmetry, the calculated curves for PD1, PD4 and PD2, PD3, respectively, are identical, b) the curve represents the calculated total minimum excess loss. Each symbol represents experimental data of one P-TWPD from TWPD#2.

measuring the responsivity of complete P-TWPDs with $d_{abs} = 430\,nm$ for optimum state of polarization. Compared to single photodiodes without MMI splitter from the same wafer with a typical responsivity of $0.39\,A/W$, an excess loss of only $1\,dB$ was determined for numerous devices, leading to a responsivity of $0.31\,A/W$. Previous results from μ-PDs based on an identical nominal epitaxial layer stack (see fig. 20a) showed responsivities of $0.5\,A/W$. Therefore, one can assume, that this particular wafer suffers from somewhat lower taper efficiencies and responsivities up to $0.4\,A/W$ in the case of a P-TWPD should be possible by achieving external coupling efficiencies in the range of 0.8.

In fig. 47, the results of the responsivity and PDL measurements of P-TWPDs with $d_{abs} = 200\,nm$ (#4, #5) are summarized (filled circles). Responsivities up to $0.32\,A/W$ (#4) and $0.26\,A/W$ (#5) were measured, which again indicate an excess loss of only $0.9\,dB$ compared to a single PD with $7\,\mu m$-length ($0.39\,A/W$ and $0.32\,A/W$) from the same wafer. In agreement with the calculations, these losses can be attributed to the MMI splitter. Owing to the polarization insensitive design, the PDL remains below $0.6\,dB$ for all P-TPWDs. The residual PDL can be ascribed to the single μ-PD.

In order to validate the accuracy of optical design of the S-TWPD, the photocurrent contributions of each individual PD in a serial-fed PD array were determined. For this measurement, the S-TWPD without the connecting transmission line shown in fig. 43b was employed. In the experiment, each photodiode was contacted separately and the maximum and minimum photocurrent in dependence of the state of polarization were measured. It should be noted, that generally the polarization states for maximum photocurrents differed for each PD and had to be optimized individually. Figure 48a gives the individual responsivity versus the PD number in the array. Results from the two wafers #4 and #5 are displayed as circles and squares, respectively. The stars represent data from a device where the optical waveguide in between the PDs is loaded by the metallization of a disconnected transmission line on top of the BCB layer, as depicted in fig. 43c. This design complies with the condition in the S-TWPD. The first photodiode facing the optical input is denoted as PD1 and shows clearly the highest responsivity of $0.38\,A/W$. From the curve fitting results one concludes that, each following PD exhibits only 20 % of the responsivity of the preceding PD,

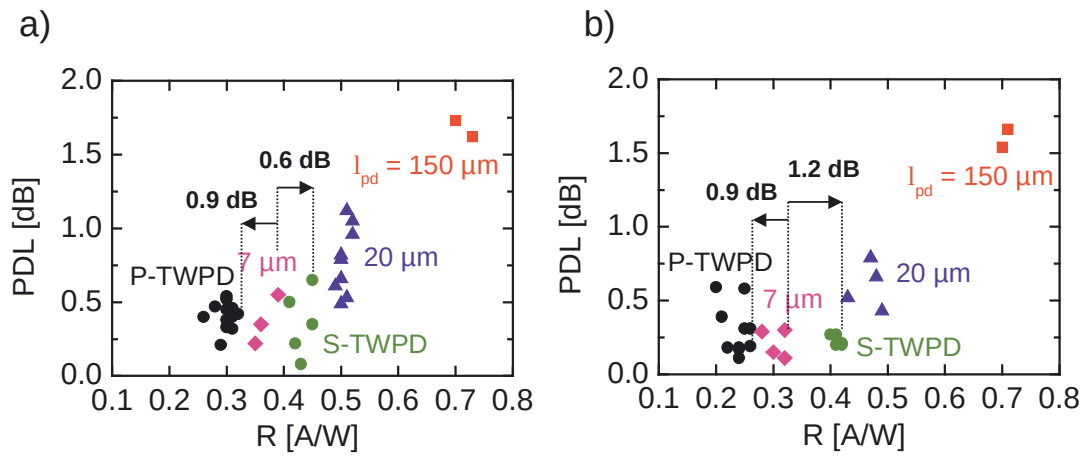

Figure 47: Results of the responsivity and PDL measurements from TWPD#4 (a) and TWPD#5 (b). Data from TWPDs as well as lumped PDs with absorber lengths $150\,\mu m$, $20\,\mu m$, *and* $7\,\mu m$ *(with a multimode waveguide length* $L = 7\,\mu m$*) are shown.*

which results in the case of PD4 in a responsivity of only $0.003\,A/W$. In this analysis, the individual photocurrent contribution was related to the input power. The PDL measurement revealed increasing values up to $6\,dB$ for the PDs 3 and 4, however, due to their minor contribution to the total photocurrent the overall PDL is negligibly affected. These results were achieved in good agreement from both considered wafers. Regarding the responsivity and the PDL, no significant influence of the metallization on top of the BCB layer was observed. From the experimental data the responsivity was calculated in dependence of the number of PDs in the S-TWPD (fig. 48b). For 3 PDs, the responsivity has almost saturated around $0.45\,A/W$, which corresponds to an improvement of more than 20 % compared to a single PD. The dotted line in fig. 48b represents the simulation result which was obtained according to section 3.6. The theoretical curve was fitted to the first data point by applying a coupling efficiency of $\eta_{ext} = 0.72$ and predicts notably higher responsivities with an increasing number of PDs. Here, each following PD exhibits 35 % of the responsivity of the preceding PD. Assuming identical absorption behavior for all PDs in the array as well

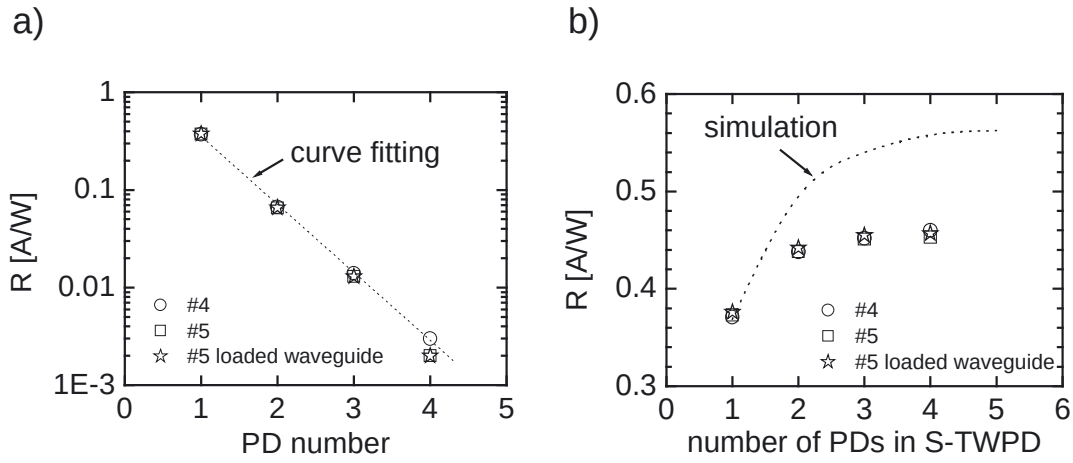

Figure 48: a) Individual responsivity versus PD number. The numbering starts with the PD facing the optical input, b) responsivity versus number of PDs in the S-TWPD. The calculated dotted line was matched to the measurement by applying a coupling efficiency of $\eta_{ext} = 0.72$. Results from the wafers TWPD#4 and #5 are shown.

as negligible losses in the waveguides ($\eta_{wg} = 1$), this deviation could be attributed to higher radiation losses at the rear of the photodiode, expressed by a decreased $\eta_{pd,wg}$ in eq. 69. The reason for that could be the process-related underetching of the PD mesa, resulting in a reduced PD length. Furthermore, the losses in the MM-PD expressed by α_m could also exceed the theoretical expectations, however, this seems more unlikely due to the short PD length ($l_{pd} = 7\,\mu m$).
The experimental results of all measured S-TWPDs are summarized in fig. 47.

5.2. Determination of the optical group velocity

In the following, the optical group velocity v_g^o is derived experimentally from Fabry-Perot resonances in a passive singlemode waveguide. Therefore, light from a tunable laser source is coupled via a tapered fibre into a straight waveguide with length L. At the opposite facet the transmitted light is collected by a second fibre leading to an optical powermeter (fig. 49a). Due to the index step between air and semiconductor

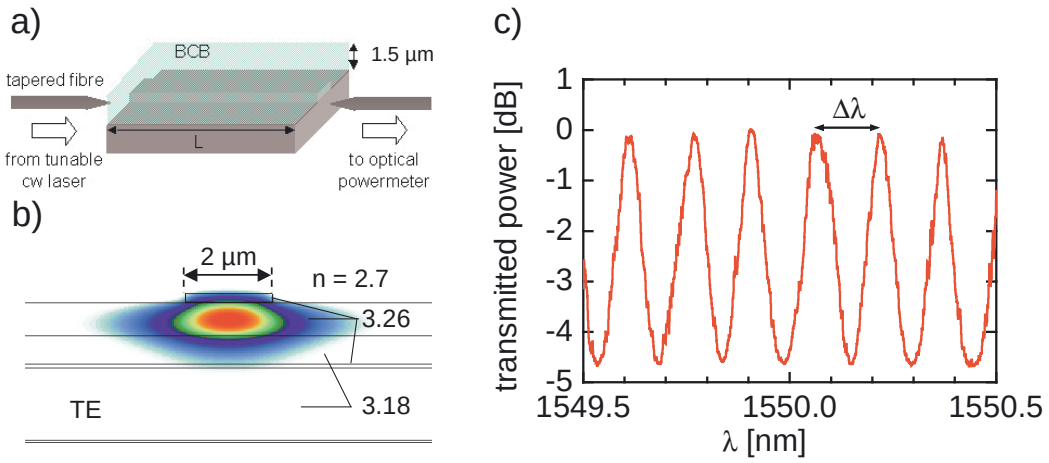

Figure 49: a) Experimental setup, b) cross sectional layer sequence of the singlemode waveguide with refractive indices and calculated TE mode profile, c) TE transmission characteristics of a BCB-loaded waveguide.

material at both facets of the waveguide, the waveguide acts as a resonator or Fabry-Perot etalon. Interference between back and forward propagating waves occurs in the waveguide, which lead to a characteristic transmittance spectrum in dependance of the wavelength. Figure 49c shows the transmitted power vs. wavelength. The device under test was a BCB-loaded rib waveguide, schematically shown in fig. 49b with the layer structure given in table 3. This structure is identical to the waveguide in fig. 14a but with $n = 1$ replaced by $n = 2.7$ and corresponds to the feeding waveguides of the TWPD. The waveguide length was determined to be $L = (2.305 \pm 0.005)\, mm$. Peaks of maximum transmission are separated by the free spectral range $\Delta\lambda$, from which the group velocity at the centre wavelength λ is calculated:

$$v_g^o = \frac{c}{n_g} = \frac{2\,L\,c\,\Delta\lambda}{\lambda^2} \tag{71}$$

Here, n_g defines the effective group index, which is caused by dispersion in the waveguide:

$$n_g = n_{eff} - \lambda \frac{d}{d\lambda} n_{eff} \tag{72}$$

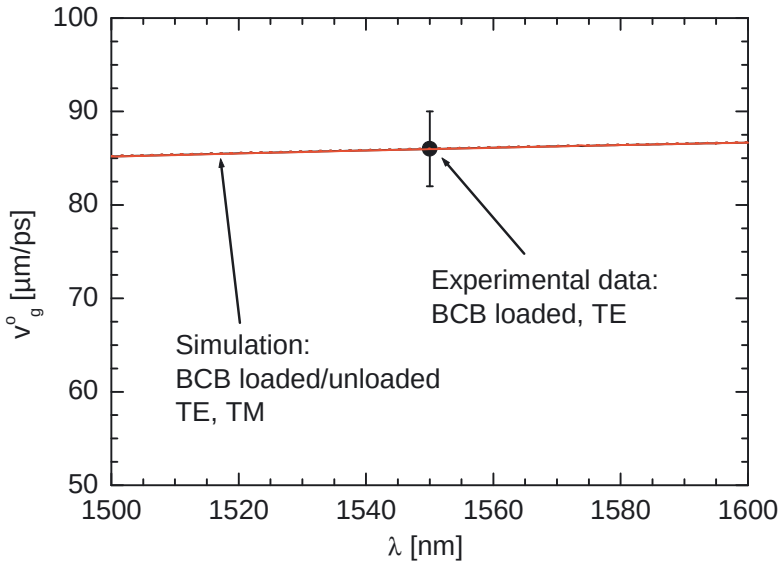

Figure 50: Optical group velocity vs. wavelength. Simulated results for TE, TM polarization for BCB-loaded and unloaded waveguides are coincident within $1\,\%$ and show good agreement with the experimental result (TE).

The averaged free spectral range and the optical group velocity around $\lambda = 1550\,nm$ were determined to be $(151 \pm 6)\,pm$ and $(86 \pm 4)\,\mu m/ps$, respectively. Equivalent measurements performed for an unloaded rib waveguide with the BCB layer on top, replaced by air, showed no differences. In this case $v_g^o = (86 \pm 3)\,\mu m/ps$ was obtained. Figure 50 summarizes the results and gives the theoretical group velocities for TE- and TM-polarized light in dependance of the wavelength. The theoretical results were obtained with *FIMMWAVE* [49] which takes the wavelength dependence of the refractive index after [65] into account. In the case of the BCB-loaded waveguide, v_g^o differs for TE and TM polarization less than 1%. In conclusion, the predicted group velocity of $86\,\mu m/ps$ could be confirmed experimentally. The simulation shows, that the optical signal velocity of the discussed singlemode waveguide is only negligibly ($< 2\%$) affected by the state of polarization, moderate variation of wavelength and BCB loading.

5.3. C-V measurements

In order to identify the bias-dependent effective thickness of the depletion layer d_{pn}, eq. 12 can be applied to the measured capacitance of a PD with known area and dielectric constant. An LCR meter (hp 4275A), operated at 10 MHz, was used for the $C(V)$ measurements. Open and short calibration procedures were accomplished in order to remove the influence of the probes and cables. In the analysis, the static dielectric constant of InGaAs was used, which may slightly overestimate d_{pn}, especially in the case of a partly quaternary depletion region. The device under test was a large area PD ($A = 28275\,\mu m^2$) embedded in BCB without electroplated contacts. Compared to a complete photodetector, this PD exhibits a lower stray capacitance and less parasitic effects. Figure 51 gives the resulting intrinsic layer thicknesses for the fabricated wafers. Corresponding to the nominal values, $430\,nm$, $350\,nm$ and $200\,nm$, the extracted d_{pn} are reasonably proportional. In all cases the depletion layer thickness grows with higher reverse bias, which can be attributed to some residual background doping ($\sim 10^{15}\,cm^{-3}$) of the not intentionally doped (n.i.d) layers. However, for an entirely depleted absorber operating voltages of <-3 V and

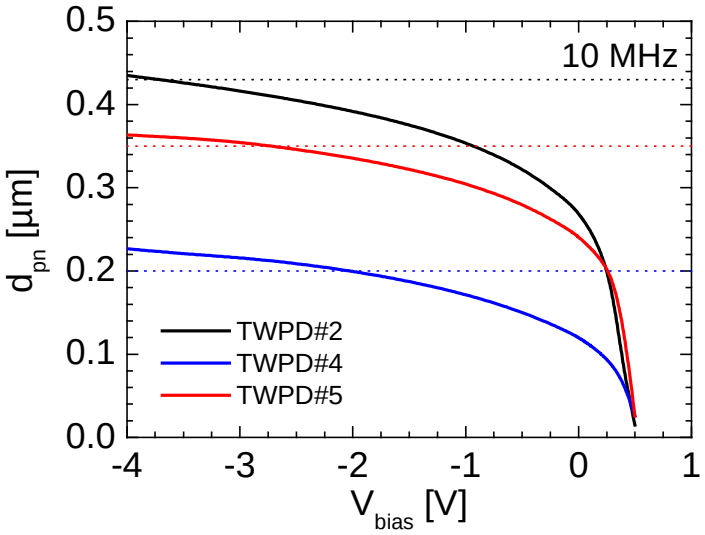

Figure 51: Intrinsic layer thickness over bias voltage deduced from C(V) measurements, dotted lines are nominal values.

<-2 V should be sufficient for #2 and #4,#5, respectively. From the above data, the capacitance of a $4 \times 7\,\mu m^2$-device was estimated by appropriate scaling of the active area, which led to $8\,fF$, $17\,fF$ and $10\,fF$ at $V_{bias} = -2\,V$.

5.4. S-parameters

5.4.1. Transmission line properties

In order to study the microwave characteristics of the fabricated transmission lines employed in the TWPD, the four complex scattering S-parameters of the unloaded CPW have been measured. The measurements were conducted with a 110 GHz network analyser (*hp8510XF*). On wafer calibration was applied [51], shifting the reference plane to the probe tips.

The considered transmission line is depicted in fig. 52a. The CPW under test of length $L_{cpw} = 300\,\mu m$ is embedded between the tapered contact pads, which allow for measurements with standard high-frequency probes.

The plots in fig. 53 give the characteristic impedance and electrical phase velocity versus frequency for the three realised line geometries with gap widths of $(16, 22, 28)\,\mu m$.

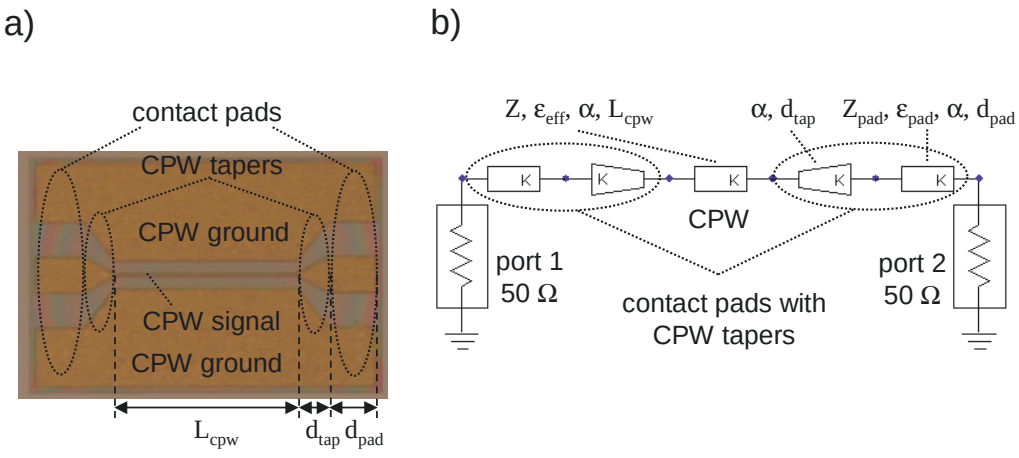

Figure 52: a) Micrograph of a fabricated CPW line from TWPD#2 with $L_{cpw} = 300\,\mu m$, $L_{tap} = 50\,\mu m$ and $L_{pad} = 80\,\mu m$, b) circuit used for de-embedding of the transmission line parameters.

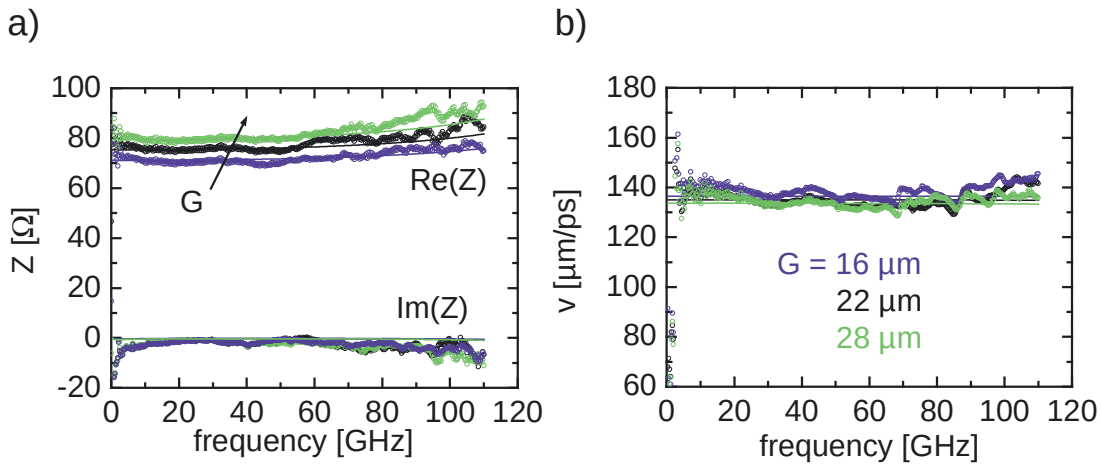

Figure 53: Measured characteristic impedance (a) and phase velocity (b) of unloaded transmission lines with $L_{cpw} = 300\,\mu m$ (circles) and gap $G = 16, 22, 28\,\mu m$ without de-embedding. The solid lines represent the results of the parameter fitting (for details see text).

These results were obtained by applying the equations given in appendix 7.4 to the raw S-parameter data without any de-embedding. As shown in fig. 53a, an increasing real part $Re(Z)$ can be observed for transmission lines with a growing gap width, due to the decreasing line capacitance C'. In all cases, the impedance remains constant over a wide range of frequencies, showing a slight slope for $f > 70\,GHz$. This effect is rather due to an impedance mismatch than to dispersion, as measurements on devices with shorter line length showed. The electrical phase velocity is less affected by the different line geometries (see fig. 53b).

Since in the experiment the impedance of the TL under test differs from the fixed impedance of the experimental setup ($50\,\Omega$), a mismatch to the TL including the contact pads exists, which gives rise to a mismatch loss and affects the measured results. As a consequence, measurements of devices with identical parameters but with different L_{cpw}, revealed significant deviations in the characteristic impedance. For example, in the case of a CPW with $G = 28\,\mu m$ and $L_{cpw} = 300\,\mu m$, an impedance

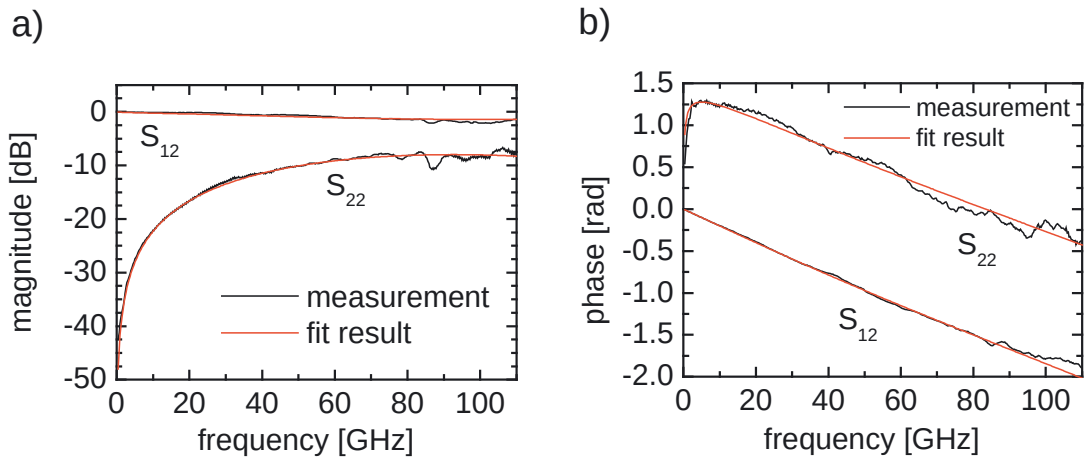

Figure 54: Results of the S-parameter fit.

of $80\,\Omega$ can be deduced from the raw data at $10\,GHz$, while the same device but with $L_{cpw} = 150\,\mu m$, exhibits only $73\,\Omega$.

In order to de-embed the intrinsic line parameters, several procedures are proposed in the literature, e.g. [72]. Here, a method of parameter fit employing the circuit shown in fig. 52b representing the pads, CPW tapers and the TL, was used for de-embedding. In the circuit simulator (*Ansoft Designer SV*), these elements are described by their characteristic impedance, effective dielectric constant and attenuation, which is modelled by a function $\propto \sqrt{f}$, as previously described in section 3.7. By varying the circuit parameters, the simulated S-parameters can be fitted to the measured results. That way, the characteristic impedance, the attenuation and the electrical phase velocity of the CPW have been extracted. The reliability of this method was enhanced by cross-checking the fit results to the measured data of identical lines with three different lengths $L_{cpw} = 1\,\mu m, 150\,\mu m, 300\,\mu m$. Figure 54 shows an example of the S-parameter fit results of a $300\,\mu m$-long CPW together with the measured raw data. The solid lines in fig. 53 represent the fit results in terms of device impedance and phase velocity.

In table 7, the extracted properties of the fabricated CPWs together with the calculated values derived from section 3.3 are summarized. Compared to the calculations,

		calculated				extracted			
W $[\mu m]$	G $[\mu m]$	ε_{eff}	v $[\mu m/ps]$	Z $[\Omega]$	α $[dB/mm]$	ε_{eff}	v $[\mu m/ps]$	Z $[\Omega]$	α $[dB/mm]$
4	16	5.37	129	81	0.51	4.6	139	74	2
4	22	5.63	126	87	0.45	4.7	137	79	2
4	28	5.81	124	91	0.42	4.8	136	84	2

Table 7: Properties of CPW lines (TWPD#2). α refers to a frequency of 100 GHz, for all calculations applies: $t = 3\,\mu m$, $h_1 = 500\,\mu m$, $h_2 = 1.5\,\mu m$ ($h_2 = 0\,\mu m$ for α), $\varepsilon_{r1} = 12.5$, $\varepsilon_{r2} = 2.7$.

the extracted Z is somewhat lower, while v exceeds the predictions. This behavior could be partly explained by a lower inductance L' in the realised TL, e.g. due to a thicker metallization layer. An insertion loss of $2\,dB/mm$ at $100\,GHz$ is determined for the realised transmission lines.
The above results were gained from devices of TWPD#2. Transmission lines from the other two wafer runs revealed very similar properties.

5.4.2. One-port measurements

Usually, lumped element photodetectors have to be integrated with a $50\,\Omega$ matching resistor at their output (compare fig. 6c) to achieve an adequate impedance-matched transition to the $50\,\Omega$-microwave-environment. Only then the device will exhibit a low output reflection S_{22} over an acceptable frequency range and represents a matched load to the e.g. subsequent external transmission line or amplifier. As a rule, a return loss of more than $10\,dB$ is required over the entire bandwidth in order to suppress potential multiple reflections between the PD chip and further electronics.
Figure 55a gives the experimentally determined magnitude of S_{22} over frequency of three discrete photodetectors. While the unterminated (open) photodiode without a matching resistor essentially shows no return loss ($S_{22} = 0\,..\,-5\,dB$), the terminated devices reach $10\,dB$ at 40 and $85\,GHz$, respectively. At low frequency, the return loss is better than $30\,dB$. With growing frequency the capacitive nature of the PD

appears in terms of an increasing S_{22}. Due to its larger capacitance (and distributed inductance in this particular design), the effect is obviously stronger in the case of the $20\,\mu m$-long PD and results in $S_{22} = -3\,dB$ at $90\,GHz$. From the S_{22} data it is straightforward to compute the impedance

$$Z = \frac{50\,\Omega \cdot (1 + S_{22})}{1 - S_{22}} \tag{73}$$

Considering the real part - this calculation leads to fig. 55b. The unterminated device turns out as expected to have a high impedance at very low frequency ($1.5\,k\Omega$). Beyond $1\,GHz$ one determines Z around $10\,\Omega$ which reflects the overall ohmic series resistance of the photodetector. In contrast, the terminated photodetector is perfectly matched in the low GHz-range and the measurement reveals primarily the quality of the integrated resistor. At higher frequencies, Z decreases and the curve approaches the ohmic series resistance.

The S_{22}-data of complete P-TWPDs from wafer TWPD#2 are given in fig. 56. Compared to the lumped PDs in the previous diagram, the output reflection is significantly lower, indicating an impedance match close to to the $50\,\Omega$-mark over a wide frequency

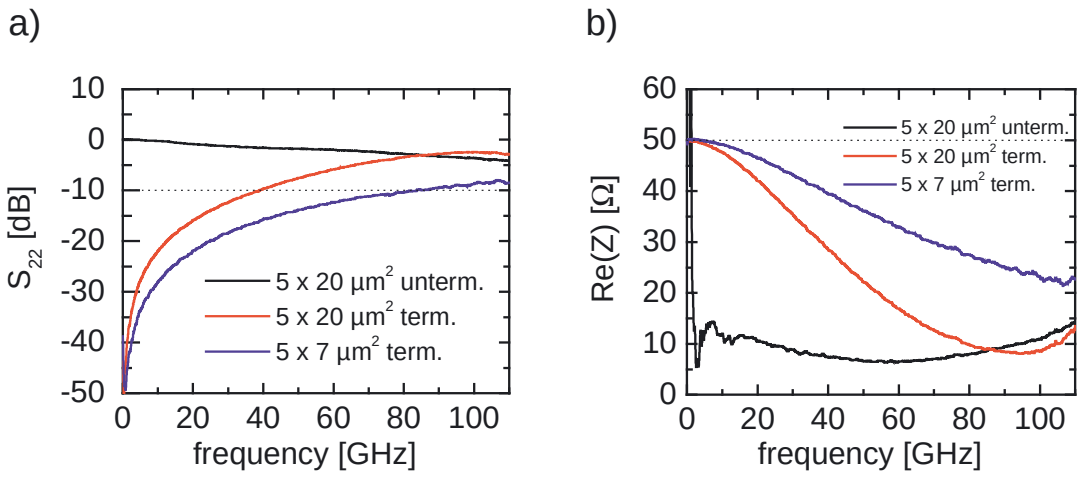

Figure 55: a) S_{22} of lumped element photodiodes (TWPD#2), b) real part of the impedance deduced from the S_{22} data.

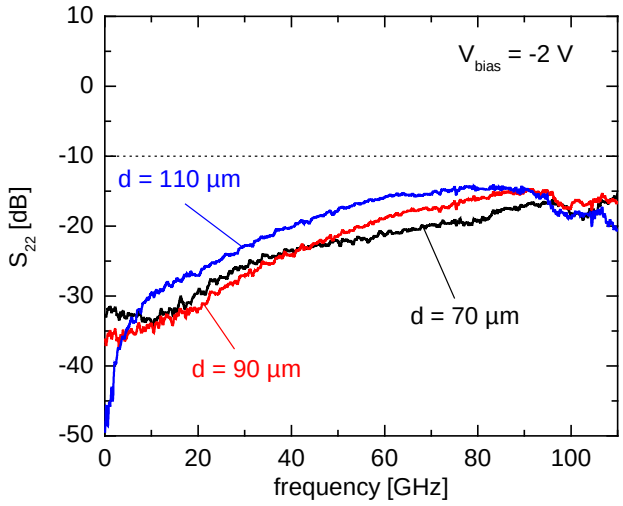

Figure 56: Magnitude of S_{22} for P-TWPDs from TWPD#2 with $G = 16\,\mu m$ and $d = 70, 90, 110\,\mu m$ determined at $-2\,V$.

range. The curve of the TWPD with the smallest PD spacing $d = 70\,\mu m$ reveals an S_{22} of less than $-15\,dB$ up to $110\,GHz$. For a larger PD spacing $d = 110\,\mu m$ a slightly increased S_{22} is observed, which suggests, that due to the reduced capacitive loading the characteristic impedance of this TWPD already exceeded $50\,\Omega$.

Figure 57a gives the results of devices from wafer TWPD#4. As these detectors comprise a thin depletion width of $200\,nm$, the loading factor is now generally larger compared to TWPD#2. In the case of the terminated device, an $S_{22} \leq -10\,dB$ can be achieved up to $110\,GHz$, independently of the applied bias voltage, as can be seen from the measurements at various bias voltages between 0 and $-2\,V$ in fig. 57a. By increasing the reverse bias, a slight decrease of S_{22} and therefore an improvement of the impedance match can be observed. This behavior can be attributed to a decrease in capacitive loading of the CPW, and confirms, that the individual photodiode is not fully depleted at lower bias voltages, in accordance with C(V)-measurements. From these results one can also conclude, that the characteristic impedance of the TWPD seems to be still below the desired $50\,\Omega$, because a lower PD capacitance induced by a higher reverse voltage leads to an improvement in return loss.

The black line in fig. 57a represents the result of an unterminated P-TWPD. Apart

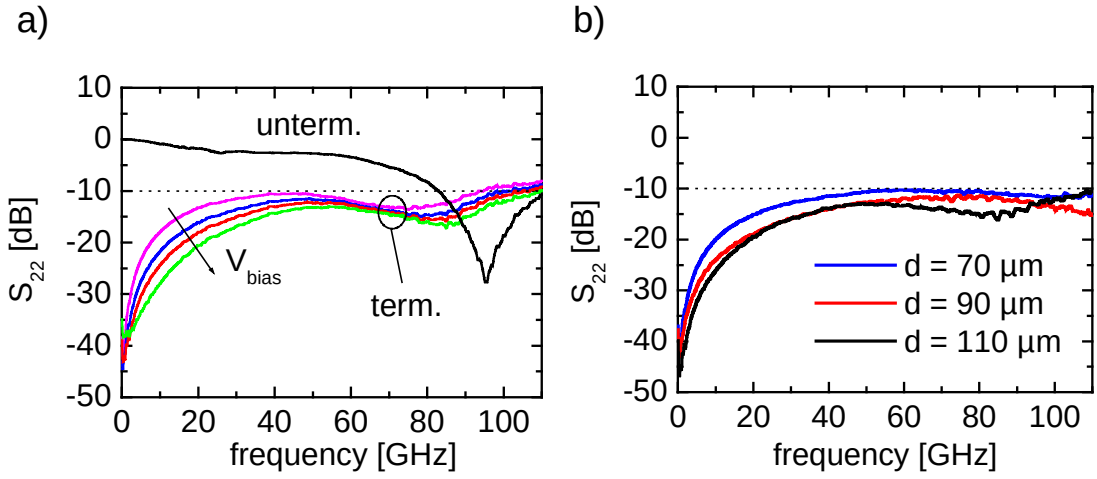

Figure 57: a) S_{22} of an unterminated (black) and terminated P-TWPD (coloured) at $2\,V$ and $0\,V, 0.5\,V, 1\,V, 2\,V$ reverse bias, respectively, from wafer TWPD#4 ($d = 110\,\mu m$, $G = 22\,\mu m$, $d_{abs} = 200\,nm$), b) S_{22} of terminated P-TWPDs from #5 (DDR structure with $d_{abs} = 200\,nm$, $d_{drift} = 150\,nm$) with $G = 22\,\mu m$ and $d = (70, 90, 110)\,\mu m$ determined at $-2\,V$.

from the dip around $95\,GHz$ it exhibits similar behavior in terms of the magnitude of S_{22} as the unterminated lumped PD in fig. 55.

From the one-port measurements, the device impedance can be estimated by curve fitting the circuit model in fig 36 to the experimental data. In the simulator, the load resistor R_l is replaced by a microwave port and $I(\omega)$ is set to zero. Once the circuit parameters are found, a second microwave port is added instead of the termination resistor R_{term}, and the device impedance is determined from the simulated two-port S-parameters according to section 7.4.

In fig. 58, the fit results (lines) of two P-TWPDs from wafer TWPD#4 together with the measured data (circles) are shown. In order to achieve sufficient agreement between simulation and experiment, the circuit model has to be modified in form of an additional RC-series element, denoted C_S and R_S, as depicted in fig. 59a. Otherwise, the variation of the given parameters does not lead to acceptable fit results. It should

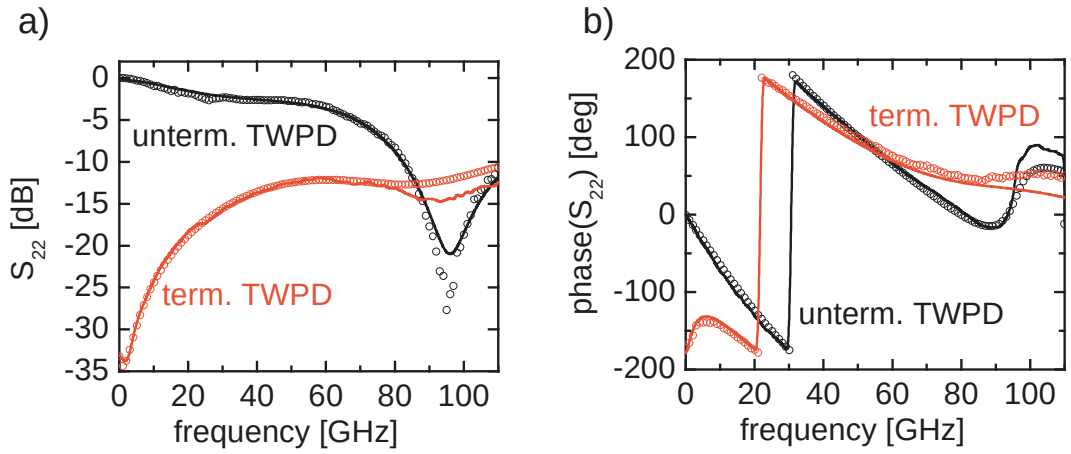

Figure 58: S_{22} magnitude (a) and phase (b) of a terminated and an unterminated P-TWPDs. Circles display the experimental data at $V_{bias} = -2\,V$ (TWPD#4), lines give the fit results with the parameters in table 8.

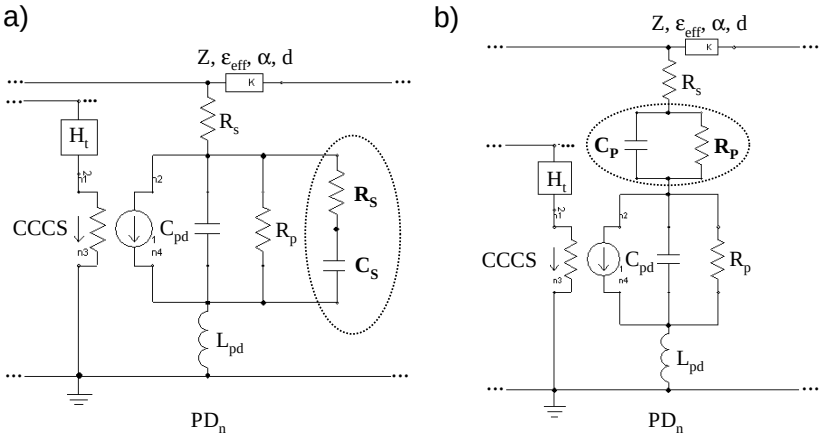

Figure 59: Single PD section with RC-series (a) and RC-parallel element (b) extracted from the TWPD equivalent circuit model.

be mentioned here, that the introduction of the RC-series element is phenomenological. In principle, the use of an RC-parallel combination as shown in fig. 59b is also possible and allows for reasonable fit results. A potential explanation of the corresponding physical meanings of the different circuit elements will be given below in

parameter	unterm. / term.	parameter	unterm. / term.
$Z\ [\Omega]$	79	ε_{eff}	5.1
$\alpha\ [dB/mm]$	2.2	$C_{pd}\ [fF]$	17
$R_p\ [M\Omega]$	3	$R_s\ [\Omega]$	15
$L_{pd}\ [pH]$	5	$d\ [\mu m]$	90
$d_{pad}\ [\mu m]$	60	$d_{tap}\ [\mu m]$	50
$d_{stub}\ [\mu m]$	10	$Z_{pad}\ [\Omega]$	52
ε_{pad}	5.9	$R_{term}\ [\Omega]$	- / 48
$C_S\ [fF]$	14 / 10	$R_S\ [\Omega]$	15 / 30

Table 8: Parameters used in the modified equivalent circuit for parameter fit of TWPDs from TWPD#4 in fig. 58. α refers to a frequency of 100 GHz .

section 5.5.2.

The parameters which were used in the model are listed in table 8. Most of them are consistent with the values in table 6 and 7. The PD capacitance C_{pd} was deduced from the above C(V) measurement. For both devices identical values were used, except those from C_S and R_S.

Using these sets of parameters, both fit results show good agreement at least up to $80\,GHz$. A characteristic impedance of the PD-loaded transmission line of $42\,\Omega$ and $43\,\Omega$ in the range up to $50\,GHz$ can be extracted for the unterminated and terminated TWPD, respectively. By omitting C_S and R_S in the circuit model, the same simulation revealed a device impedance of $48\,\Omega$, indicating that the RC-series element leads to an additional capacitive loading.

In order to lower the PD capacitance, the TWPD with dual depletion region was introduced. However, regarding S_{22}, an improvement was not traceable as can be seen from the measurements of terminated P-TWPDs from wafer TWPD#5 in fig. 57b. Again, devices with the lowest capacitive loading with $d = 110\,\mu m$ showed the best results in terms of an output reflection of $< -11\,dB$ over the entire measurement range, suggesting that these devices suffer from similar effects as TWPD#4.

To sum up, even though some undesired loading effects have been observed, all con-

sidered TWPDs with termination resistor revealed an output reflection of less than $-10\,dB$ over the entire measurement range. This value represents a significant improvement, even when compared to miniaturized lumped element PDs.

5.5. O/E heterodyne measurements

5.5.1. Experimental setup

The optical heterodyne detection scheme is based on the nonlinear relation between the incident electromagnetic fields of two laser signals with slightly different wavelengths and the generated photocurrent in the detector (see appendix 7.6). It is well-suited to determine the amplitude of the photodetector's O/E transfer function, because a calibration of the optical signal over frequency is not necessary.
Figure 60 shows the experimental setup. The laser signals are provided by two external cavity lasers (ECL) operating around $1.55\,\mu m$ wavelength followed by polarization scramblers (parallel polarization ensured) and fibre based power splitters. About 10 % of each signal of the available power are fed into a 2x1 optical switch, which is connected to an optical powermeter and wavelength meter, respectively. Here, both power levels as well as wavelengths are monitored. The 90% signal paths lead to a 3 dB combiner, where both signals are superimposed. From there the signal passes

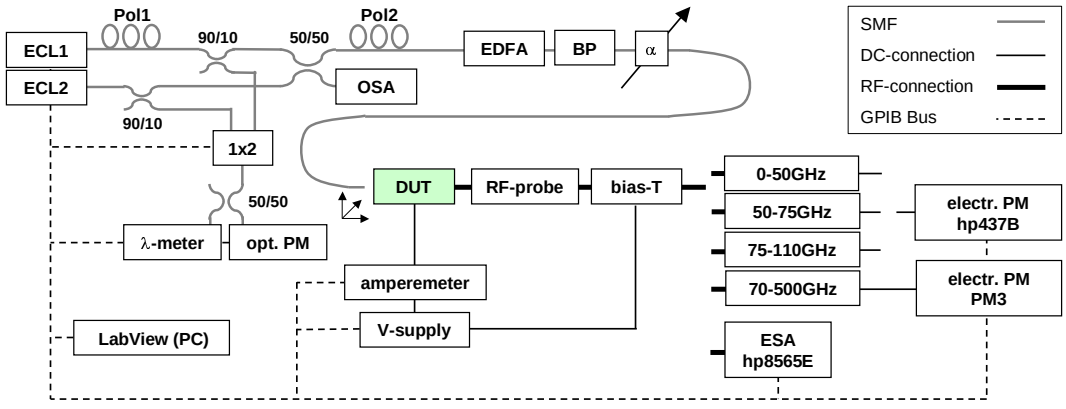

Figure 60: Setup for O/E heterodyne measurements. All relevant instruments are controlled over GPIB by LabVIEW measurement software.

through a second polarization scrambler and enters an erbium doped fibre amplifier (EDFA). The EDFA is followed by an optical bandpass filter ($5\,nm$) and a variable attenuator. In the case of on-wafer measurements, the signal is injected via a cleaved fibre into the device under test. On the output side, the DUT is contacted with a high-frequency coplanar probe head. Depending on the signal frequency, the electrical output power can be detected alternatively with a $50\,GHz$ electrical spectrum analyser (ESA), a calibrated electrical microwave power meter (hp437B) with three different power sensors and an Erickson PM3 submm power meter [70]. The detected RF output power is considerably affected by the microwave components (probe, bias-T, adapters), which are used in the signal path. By subtracting the frequency-dependent losses $L_i(f)$ of all parts i from the measured power $P_m(f)$, the frequency response can be corrected:

$$P_{rf}(f)\ [dBm] = P_m(f)\ [dBm] - \sum_i L_i(f)\ [dB] \tag{74}$$

This is a reasonable method, as long as the return losses of the different components are well-below $-10\,dB$. In order to determine the calibration data $L_i(f)$ we performed S-parameter measurements (DC to $170\,GHz$) or referred to the manufacturer's specifications. Data was only not available in the case of the PM3 calibration. However, a direct comparison with the hp meter showed excellent agreement in the W-band [75]. Since all setups provide sufficient overlap in frequency, a continuous response from several MHz up to some hundred GHz can be obtained by merging the results from adjoining spans.

5.5.2. Experimental results

Photodetectors with 430 nm-absorber thickness

The influence of the termination resistor on the frequency-response of a parallel-fed TWPD with a $430\,nm$-absorber is studied first. Therefore, fig. 61 compares the data of two TWPDs with identical design, but one without termination resistor. Each curve consists of four individual measurements, given by the available frequency bands of the setup. The absolute electrical power levels refer to the measurements in the fre-

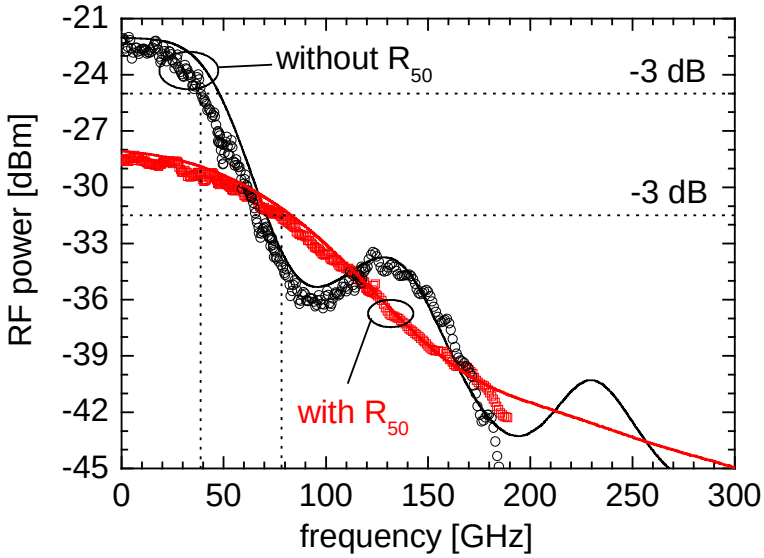

Figure 61: Electrical power vs. frequency for a TWPD with (red symbols) and without (black symbols) termination resistor. Both devices stem from the same wafer with $d_{abs} = 430\,nm$ *(#2) and* $d = 90\,\mu m$*. Lines illustrate the simulation results.*

quency range up to $50\,GHz$, which were done at an optical input power of $+2.3\,dBm$. Given that both detectors showed a responsivity of $0.3\,A/W$ the DC photocurrents were $0.5\,mA$. Above $50\,GHz$ the input power was reasonably higher to increase the signal-to-noise ratio, but making sure that the photodetectors are still working in the linear regime. As next, for a smooth transition, the absolute power levels of these data were normalised to a photocurrent of $0.5\,mA$. In the case of the unterminated device (black circles), a 3 dB bandwidth of $40\,GHz$ is obtained. The interaction of the forward and the reflected backward travelling wave leads to significant distortion at higher frequencies. Due to the interference effects, the response drops by $14\,dB$ at $95\,GHz$ and shows a local maximum at $130\,GHz$. A comparison with the results from the circuit simulator (solid lines) using the model in fig. 36 shows good agreement. Only at frequencies $> 180\,GHz$, the response deviates distinctly from the simulation. This behavior can be attributed to an insufficient calibration of the measured curve, as reliable calibration data of the experimental setup were available only up to $170\,GHz$. For higher frequencies the calibration curve was simply extra-

polated which may underestimate the losses in the setup. The relevant values of the parameters used in the simulation are summarized in table 9.

The bandwidth result seems plausible, since eq. 55 together with $C_{pd} = 8\,fF$ and $d = 90\,\mu m$ leads to an electrical signal velocity of $v_0 = 90\,\mu m/ps$, which limits the bandwidth due to phase mismatch to $59\,GHz$ (see fig. 28). Considering a transit time-limited cut-off of $73\,GHz$ and neglecting any further effects, an overall 3 dB bandwidth of $46\,GHz$ is calculated.

By implementing the matching resistor at the input of the CPW, the backward travelling wave is terminated and the bandwidth can be significantly enhanced up to $80\,GHz$, as shown by the red circles in fig. 61. Even at $140\,GHz$, the response has dropped only by $10\,dB$. However, due to the integrated resistor half of the photocurrent is being lost, resulting in a reduction of absolute output power of $6\,dB$ at low frequencies. Once again, the simulation with the parameters in table 9 shows excellent agreement with the experimental data. This design is obviously limited by the carrier transit time, as the calculated 3 dB bandwidth due to transit-effects is $f_t = 73\,GHz$.

It is worth noting that the absolute mm-wave power generated by the unterminated TWPD can exceed the output power of the terminated TWPD around certain resonance frequencies. This could be interesting, especially for the generation of narrowband THz-signals.

The response is less affected by changes of the transmission line properties and measurements of devices with different CPW gaps G and various spacings d reveal only

parameter	TWPD#2	parameter	TWPD#2
$Z\ [\Omega]$	84	ε_{eff}	4.8
$\alpha\ [dB/mm]$	2	$C_{pd}\ [fF]$	8
$d_{pn}\ [nm]$	390	$d\ [\mu m]$	90
$R_{term}\ [\Omega]$	50 (if applicable)	$I(\omega)\ [mA]$	0.5

Table 9: Relevant values for TWPD#2 used in the circuit simulator. All other parameters can be found in table 6. α refers to a frequency of 100 GHz.

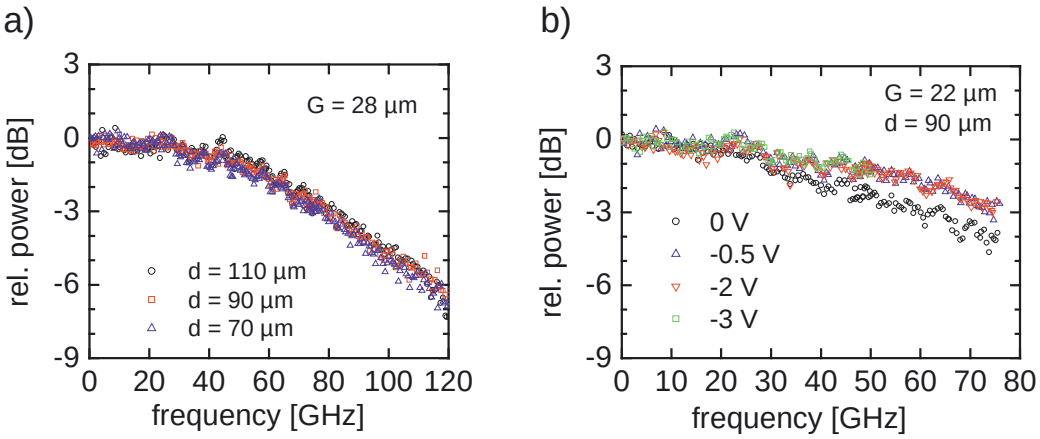

Figure 62: a) Frequency responses of P-TWPDs with different PD spacings d; for comparison, the transit time-limited 3 dB bandwidth amounts to $73\,GHz$, b) bias-dependence of the frequency response, $P_{opt} = +2.3\,dBm$ (TWPD#2).

minor changes in the frequency response up to $110\,GHz$ (fig. 62a). At a moderate input power the variation of the bias $\leq -0.5\,V$ did not significantly change the response (fig. 62b). This verifies, that even in a non-entirely depleted absorber the contribution of a slower diffusion current is small enough, that a fast charge carrier transport is possible. However, at $0\,V$, the bandwidth decreases to $60\,GHz$ which can be explained by the reduced drift velocity of the holes.

Photodetectors with 200 nm-absorber thickness

The reduction of the depletion width to $200\,nm$ pushes the carrier transit time-limited bandwidth to $150\,GHz$ and should enable extended bandwidths of the TWPD. The same considerations are valid for the miniaturized lumped element PD, which has already been shown to reach a transit time-limited bandwidth of $120\,GHz$ in the case of a $270\,nm$-depletion width [76].

Considering the lumped μ-PD from wafer TWPD#4 first, fig. 63 gives the frequency characteristics of a $50\,\Omega$-terminated device with $(4 \times 7)\,\mu m^2$ active area indicated by the blue circles. The plot exhibits a smooth decay of only $6\,dB$ up to $180\,GHz$. The $3\,dB$ bandwidth reaches $145\,GHz$, which is a record-bandwidth for waveguide-integrated photodetectors. The responsivity of this particular photodetector amounts

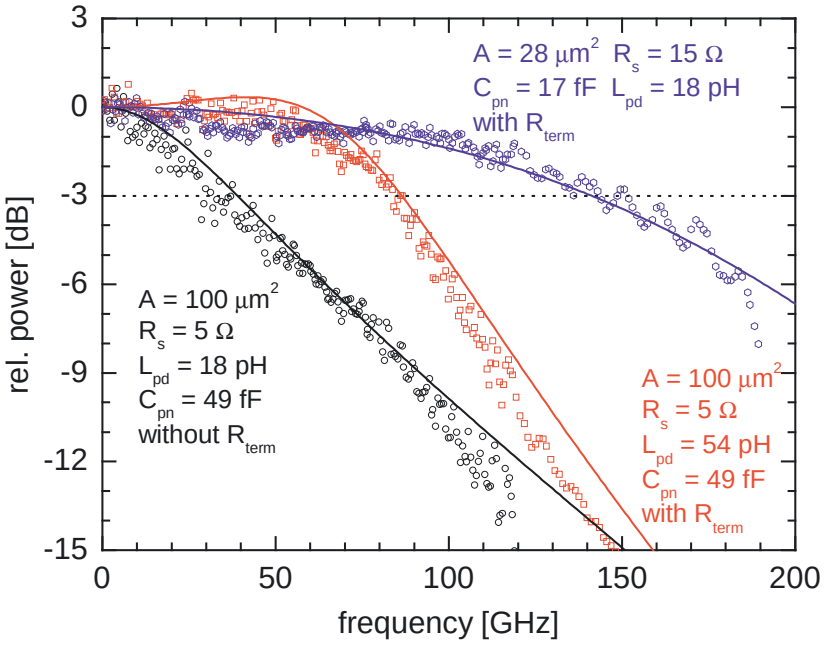

Figure 63: Frequency characteristics of lumped element PDs (symbols) and results from the equivalent circuit simulation (lines) for TWPD#4 with $d_{abs} = 200\,nm$.

to $0.35\,A/W$ (with ARC).

For comparison and to verify the theoretical model, the results of $(5\times20)\,\mu m^2$-devices with and without termination are depicted. Due to RC-limitation, both photodetectors exhibit significantly lower bandwidths. The lines indicate the calculated responses deduced from the analytic approach in section 3.2.1 and reveal good agreement with the measured data. The parameters of the equivalent circuit elements C_{pd}, R_s and L_{pd} are given in the figure. The data was gained from parameter extraction of S_{22}-measurements. In this procedure experimental S_{22} data are fitted by the parameters of the lumped element PD equivalent circuit, similar to the method already described in section 5.4.2. In order to achieve best fit results, the stray capacitances were set to $5\,fF$ and $15\,fF$ for the $28\,\mu m^2$ and $100\,\mu m^2$ photodetectors, respectively. The latter is somewhat higher than that of comparable devices without BCB passivation [77]. The inductance L_{pd} of the $(4\times7)\,\mu m^2$-device origins from the short airbridge, which connects the metal p-contact with the signal line (for details see fig. 42b). The length

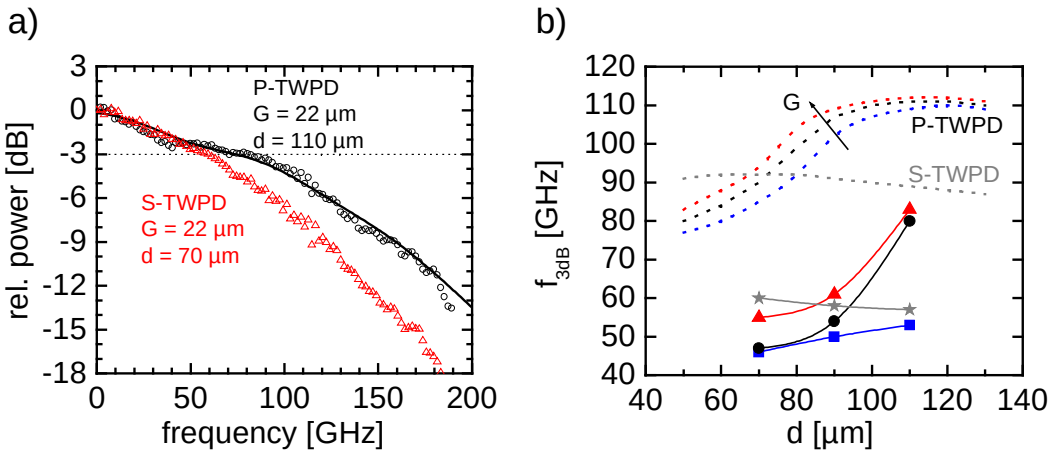

Figure 64: a) Frequency characteristics of P-TWPD (circles) and S-TWPD (red triangles) from TWPD#4 with $d_{abs} = 200\,nm$. Both devices contain an internal termination resistor, the black line indicates the simulation utilizing the modified equivalent circuit, b) 3 dB bandwidth versus PD spacing. Squares, circles and triangles refer to P-TWPDs with $G = (16, 22, 28)\,\mu m$, respectively. The stars illustrate results from S-TWPDs with $G = 22\,\mu m$. The dotted lines are the modelling results with $G = (16, 22, 28)\,\mu m$ (P-TWPD) and $G = 22\,\mu m$ (S-TWPD).

of the airbridge was set to $l = 30\,\mu m$ in the design, in order to exploit RLC-effects for best bandwidth performance. The $100\,\mu m^2$-PD with termination resistor includes an optimized output electrode configuration according to [44], which can be described approximately by an increased inductance of $L_{pd} = 54\,pH$ in the lumped element model. However, as fig. 10a confirms, an increased inductance does not lead to an optimal bandwidth performance in the case of $d_{pn} = 200\,nm$.

The experimental results of the serial and parallel-fed terminated TWPD are given in fig. 64a. The bandwidth of the P-TWPD, displayed by black circles, amounts to $83\,GHz$. Especially at frequencies above $90\,GHz$, the TWPD, which comprises a total active area of $4 \times 28\,\mu m^2$, profits from a partial compensation of the RC-limit when compared with the lumped element photodetector with an active area of $100\,\mu m^2$ and termination resistor in fig. 63. For instance in the $150\,GHz$ range, the difference in their responses amounts to $7\,dB$ to the benefit of the TWPD. Thus, the travelling

wave concept has been demonstrated.
In fig. 64b, f_{3dB} is given in dependence of the PD spacing. The symbols give the measured results and reveal, that for $d = 70\,\mu m$ the P-TWPD shows only a bandwidth of $55\,GHz$, while for $d = 110\,\mu m$, corresponding to the lowest capacitive loading, a maximum bandwidth of $83\,GHz$ can be achieved. The dependence of the gap is also marked: best results were achieved for largest gaps, which points out that by increasing the transmission line impedance the bandwidth is expanded.
The dotted lines represent the circuit simulation results using the model in fig. 36 with the nominal parameters in table 6 and the extracted TL data in table 7; the depletion width was set to $d_{pn} = 200\,nm$ and the PD capacitance amounts to $C_{pd} = 17\,fF$. Compared to the experimental data, the model predicts definitely larger bandwidths. The detailed comparison of the simulated response with the measured data in fig. 64a reveals that in particular the $2\,dB$-drop on the first $40\,GHz$ can not be reproduced by the circuit model with reasonable parameters. From the assumed values $Z = 79\,\Omega$, $\varepsilon_{eff} = 4.7$, $C_{pd} = 17\,fF$ and $d = 110\,\mu m$ the resulting characteristic impedance and the electrical phase velocity are determined to be $48\,\Omega$ and $84\,\mu m/ps$, respectively. Therefore one can conclude that the device should exhibit a sufficient impedance match as well as an excellent velocity match of 97%. The Bragg frequency is determined to be $244\,GHz$, which is high enough to provide a smooth frequency response up to more than $100\,GHz$.
In order to explain the observed bandwidth, a further loss mechanism has to be taken into consideration. A potential explanation could be hole trapping in the p-isotype heterostructure. This effect would be adequately modelled in the equivalent circuit by an RC-parallel combination [73] (see fig. 59b) and should be also visible in the case of lumped element PDs. As these PDs exhibit a frequency response which is in good agreement with the analytical model, the existence of a capacitively-coupled conductive surface layer, which leads to a decay in the response at lower frequencies, seems to be more likely. This effect could originate from some process-related irregularities at the PD mesa surface and can be represented by the series element depicted in fig. 59a.
By utilizing the circuit model in fig. 36, modified by the RC-series element in fig. 59a, a much better agreement with the measured data was found. The fit result using

$R_S = 10\,\Omega$ and $C_S = 7\,fF$ (other parameters as in the previous simulation) is shown by the black line in fig. 64. As already demonstrated by the S_{22} fit results in fig. 58, the modified circuit model is again well-suited to describe the high frequency behavior of devices from this particular wafer.

Though the studied S-TWPD is based on a very similar transmission line layout and photodiode geometry as the parallel type, it shows a deviating response and a lower bandwidth of only $61\,GHz$ (red triangles in fig. 64a). By analysing the dependence of f_{3dB} on the spacing d in fig. 64b, one finds out that with growing d the bandwidth decreases slightly, which is in contrast to the P-TWPD. In order to motivate this behavior, one can indicate a major difference between the parallel and serial type regarding the internal photocurrent distribution: While in the P-TWPD the current contributions of each PD are of the same magnitude, the S-TWPD exhibits an exponentially decaying photocurrent for increasing PD numbers. According to section 5.1, the first PD facing the optical input side provides the highest photocurrent while each following PD shows only a fraction of 20%. By taking the correct distribution into account, the circuit simulator reveals a qualitatively similar dependence as can be seen from the dotted grey line in fig. 64b. Due to the longer path length, the output current of the first PD suffers from the highest loss. Regarding the absolute performance, the S-TWPD lags behind the predictions as similar damping effects to those in the P-TWPD may be the case.

Photodetectors with dual depletion region

The implementation of a depleted, transparent electron drift layer gives rise to a lower pn-capacitance at only a slightly increased electron drift time. In the TWPD this structure can be used to relax design constraints of very thin absorbing layers and compensate for stray capacitances, in order to achieve impedance and velocity match. Since the capacitive loading is decreased, a reduced PD spacing may be possible to expand the Bragg-limit.

Figure 65 shows the measured results for lumped PDs and a P-TWPD, all with integrated termination resistor from TWPD#5 with $d_{abs} = 200\,nm$ and $d_{drift} = 150\,nm$. Compared to the lumped element PDs from TWPD#4 in fig. 63, the bandwidth of the $100\,\mu m^2$-device can be pushed to $102\,GHz$ due to the decreased PD capacitance.

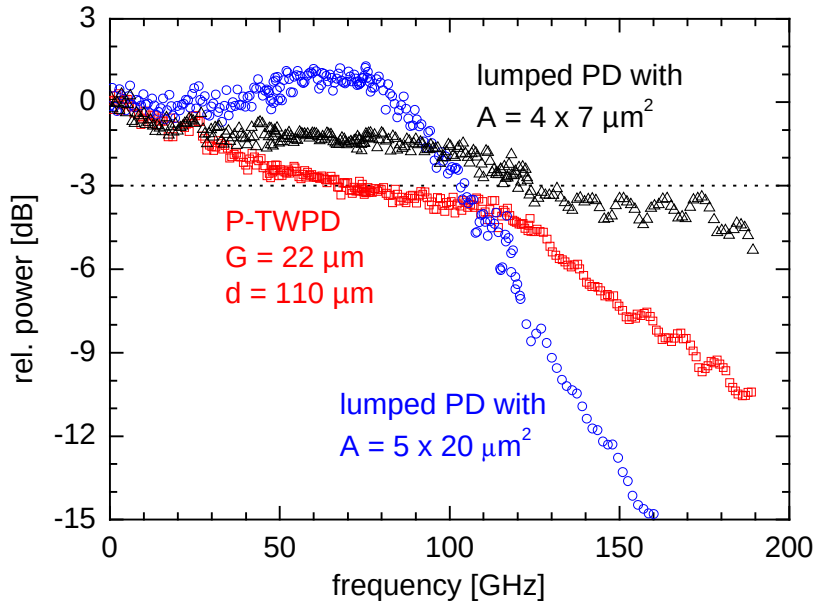

Figure 65: Frequency characteristics of lumped element PDs and P-TWPD from TWPD#5 with DDR structure; $d_{abs} = 200\,nm$, $d_{drift} = 150\,nm$.

For the μ-PD with $A = (4 \times 7)\,\mu m^2$, the measurement reveals a bandwidth of $123\,GHz$. As this device is limited primarily by the carrier transit times ($f_t = 114\,GHz$), the additional drift layer in the structure leads to a longer electron drift time and a reduced bandwidth compared with fig. 63. However, the relative drop of the frequency response remains above $-4\,dB$ up to $180\,GHz$.

The P-TWPD reaches a bandwidth of $75\,GHz$. An impact of the dual depletion region can be observed at frequencies above $140\,GHz$, where a higher relative response of $3\,dB$ compared to the P-TWPD without drift layer in fig. 64a can be determined. The corresponding circuit simulation predicts a f_{3dB} of $103\,GHz$, which is about 25% larger than measured. As this wafer shows similar characteristics in terms of $I(V)$ and S_{22} as TWPD#4, it seems plausible that here too, the above mentioned bandwidth constraints apply (both wafers have been fabricated at the same period).

5.6. Pulse measurements

In contrast to the heterodyne-method, where only the magnitude of the photodetector's transfer function is deduced, the opto-electronic pulse measurement in the time domain provides both, magnitude *and* phase. It reveals quantities as the detector's pulse width, rise-, fall-times and ringing, which are of certain interest especially when considering applications in digital optical frontends.

5.6.1. Electrical sampling setup

The setup for pulse measurements is illustrated in fig 66. An actively mode locked laser (MLL) serves as optical pulse source with a pulse width of $1\,ps$ and a repetition rate of $10\,GHz$ at $1.55\,\mu m$ wavelength. From there the signal passes a polarization controller and enters an EDFA followed by an attenuator. Finally, it is injected via a cleaved fibre into the photodetector chip. On the chip's output side a coplanar probe, a short ($10\,cm$) coaxial cable and a high-speed electrical sampling scope (Agilent 86100C with 86118A) are used to extract the electrical signal. The scope is directly triggered by the $10\,GHz$ sine wave of the synthesizer. The performance of the current setup is mainly limited by the electrical sampling scope, since the pulse width of the optical pulse is around 1 ps. Therefore, it is short enough to be approximated as a delta-shaped stimulus. In contrast, the bandwidth of the employed sampling head has been experimentally determined by swept-sine calibration [74] to be $77\,GHz$, which results in an instrument-limited response with a full width at half maximum (FWHM) of $6\,ps$. According to the manufacturer's data the instrument's rise time (from 10%

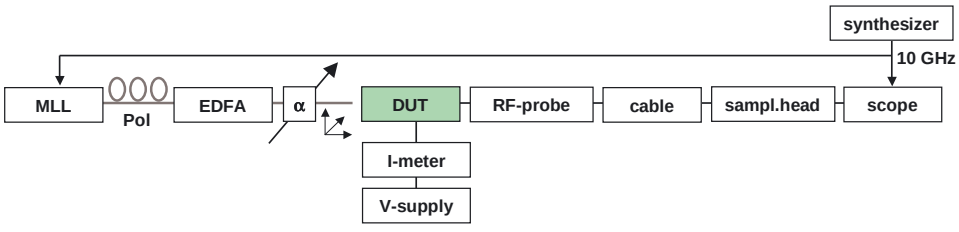

Figure 66: Experimental setup for on-wafer o/e pulse measurements.

to 90%) amounts to $4.5\,ps$.

5.6.2. Experimental results

Using the above setup, pulse measurements of travelling wave and lumped element photodetectors from the same wafer with DDR layer structure (TWPD#5) have been carried out. In figure 67a the results taken in the linear regime at a low output amplitude are shown. The black line indicates the response of the parallel-fed TWPD with termination resistor. The analysis yields a pulsewidth of $7.4\,ps$ and rise/fall times of $6.3\,ps$ and $3.5\,ps$, respectively. Regarding ringing, the TWPD exhibits an undershoot of only 8%. In contrast, the unterminated TWPD (red line) shows considerably increased pulsewidth ($9\,ps$) and fall time ($9.3\,ps$) due to a pronounced tail in the response. This can be attributed to the interference with the reflected backwards travelling wave. In figure 67b the results of two discrete photodetectors with integrated termination resistors are given. They exhibit comparable results compared to the terminated TWPD, in terms of pulsewidth, rise and fall times. However, the

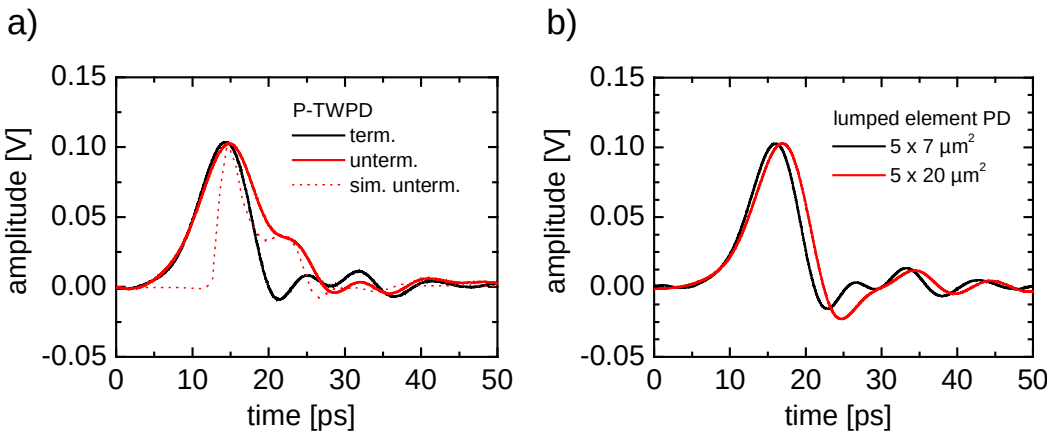

Figure 67: a) Measured pulse responses of P-TWPDs with (black) and without (red) termination resistor. The optical input was adjusted depending on the chip's responsivity to match a peak voltage of. 0.1 V. The dotted line gives the simulation result of the latter, b) pulse responses of lumped element PDs with $5 \times 7\,\mu m^2$ (black) and $5 \times 20\,\mu m^2$ (red) active areas (TWPD#5).

	$5 \times 7\,\mu m^2$ PD	$5 \times 20\,\mu m^2$ PD	P-TWPD
rise $[ps]$	6.2	7.3	6.3
fall $[ps]$	3.2	3.5	3.5
FWHM $[ps]$	7	7.8	7.4
undershoot $[\%]$	15	23	8

Table 10: Results from the time domain measurements in fig. 67 at low optical input powers. All photodetectors contain an integrated termination resistor.

undershoot is notably higher and amounts to 15 % and 23 % for the $5 \times 7\,\mu m^2$ and $5 \times 20\,\mu m^2$ PDs, respectively. In table 10 the characteristics are summarized. The comparisons with the simulated results (dotted line in fig. 67a) provide only qualitative agreement, due to the bandwidth limitation of the experimental setup. Assuming Gaussian pulse shapes and using the simple formula

$$FWHM^2_{DUT} = FWHM^2_{measure} - FWHM^2_{scope} \tag{75}$$

one can estimate the pulse width of the terminated TWPD to be $4.3\,ps$, which still includes the influence of the RF probe. This agrees well with the predicted pulsewidth of $4.1\,ps$.

5.7. High-power saturation effects

5.7.1. Frequency domain

The small active volume of a lumped element high-speed photodiode leads inevitably to a higher photocurrent density and increased ohmic heating, which give rise to saturation and potential device failure. Since the TWPD contains a comparatively larger overall active volume, it offers improved high-power capability and, if bandwidth is maintained, a better bandwidth-saturation current-product. The following measurements were carried out utilising the already described O/E heterodyne setup, operated at a fixed beat frequency. The DC photocurrent as well as the electrical output power were determined at constant external bias voltage.

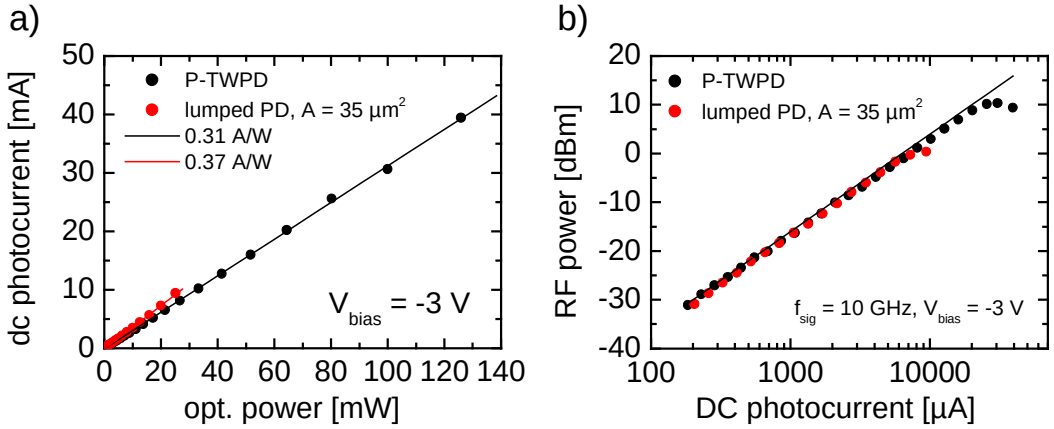

Figure 68: a) DC photocurrent vs. optical input power, b) detected output power vs. the DC photocurrent (both devices without termination resistor from TWPD#2) at $V_{bias} = -3\,V$. The line in (b) indicates the ideal current-power relation at a $50\,\Omega$ load.

In fig. 68a the DC photocurrent of a P-TWPD in dependence of optical input power at $3\,V$ reverse bias is depicted. A linear photocurrent up to $39\,mA$ has been measured corresponding to a responsivity of $0.31\,A/W$. For comparison, a single $(5\times7)\,\mu m^2$-PD from the same wafer and 0.37 A/W responsivity reached a maximum linear photocurrent of $10\,mA$, before failure.

In fig. 68b the same devices (both without termination resistor) were studied at a beat frequency of $10\,GHz$. In the case of the TWPD a maximum electrical output power of $+10.3\,dBm$ has been detected; compared to the single PD with a slightly larger active area ($35\,\mu m^2$) than the PDs contained in the TWPD ($4 \times 28\,\mu m^2$), this is an improvement of $10\,dB$ available output power. A gain of $12\,dB$ would be expected in comparison with a single PD of $28\,\mu m^2$.

The 1 dB compression point denotes the average photocurrent, at which the RF output power at a specified frequency deviates 1 dB from the quadratic current-power relation at a fixed load. In the previous measurements the $1\,dB$ compression points amount to $8\,mA$ and $27\,mA$ for the single PD and the TWPD, respectively.

Identical experiments were performed at $2\,GHz$ and $40\,GHz$ signal frequency. The

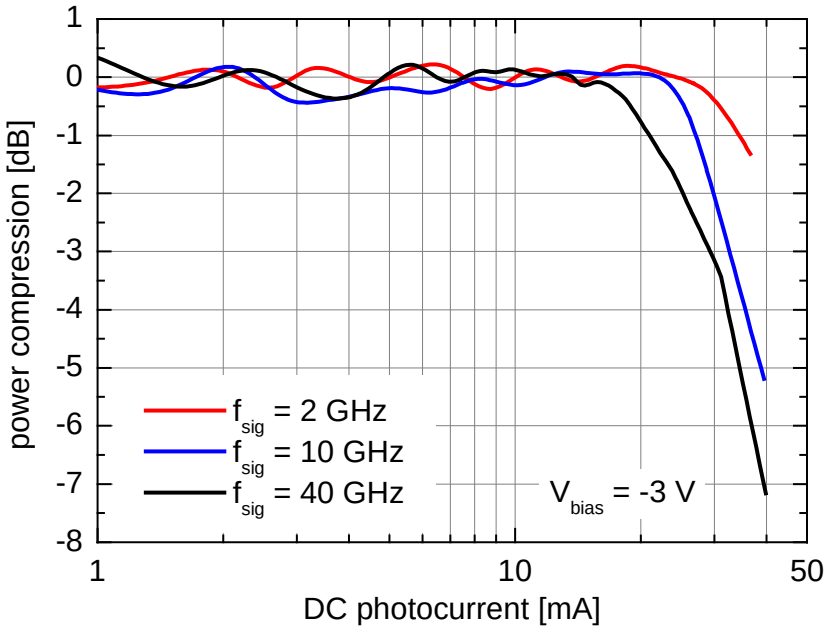

Figure 69: Compression curves at $2\,GHz$, $10\,GHz$, $40\,GHz$ at $V_{bias} = -3\,V$ from a P-TWPD (TWPD#2).

deduced power compression curves of the P-TWPD, illustrated in fig. 69, are constant over the entire linear working range, in contrast to detectors based on UTC photodiodes, which often show an increasing RF response when the optical input power is raised from low to medium values [40]. A similar measurement at $110\,GHz$ signal frequency using a terminated P-TWPD from the same wafer showed a maximum output power of $-1.8\,dBm$ and a compression point of $23\,mA$, which compares favorably to a lumped element PD with a comparable total active area and absorber thickness showing $-7\,dBm$ at $100\,GHz$ [44].

The decrease in RF output power at high photocurrents can be generally attributed to a reduced electric field in the depletion layer, which gives rise to lower carrier drift velocities and therefore longer transit times. The two main reasons for the reduction of the electric field are a voltage drop at ohmic resistances and screening effects induced by the space-charge of photogenerated holes and electrons [14, 13], as outlined in section 2.1. The former is proportional to the total series resistance, including both contributions from inside the structure and the external bias path. It

should be noted, that for structures which are not fully depleted this could also lead to a smaller depletion width and hence an increased capacitance. In the considered case, the external bias was chosen large enough to assure, that even at photocurrents of $34\,mA$ the voltage drop did not lead to an effective reverse bias below $2\,V$. At the low modulation frequency of $2\,GHz$, the DC model in section 2.1 can be used to estimate the electrical field in the absorber under illumination. Using the results from fig. 69 at $2\,GHz$, the peak photocurrent density of a single PD in the TWPD amounts to $60\,kA/cm^2$ at $1\,dB$ RF compression. For calculating the carrier densities, equation 11 is applied, using $N_D = 10^{15}\,cm^{-3}$, $V_b = 0.6\,V$ and $d_{abs} = 420\,nm$. V_b was determined from the voltage at which the depletion width tends to zero in fig. 51. The effective bias is reduced to $2.3\,V$ which corresponds to an internal and external resistance of $15\,\Omega$ and $5\,\Omega$, respectively. With these data, a local minimum electrical field in the absorber of $35\,kV/cm$ is computed, which compares well with the critical field around $40\,kV/cm$ at which the holes travel below their saturated drift velocity (compare fig. 2).

Depending on the application, saturation effects far beyond the 3 dB bandwidth may be of certain interest. Especially when considering the efficient generation of submm- and THz-waves in the photodetector by means of optical heterodyning, a large absolute output power at ultra-high frequencies is desired. Fig. 70a shows the most successful results, which have been achieved with a parallel-fed travelling wave photodetectors comprising a dual depletion region. Again, the DC photocurrent was linear for all applied optical input powers. At $150\,GHz$, the maximum output power reaches $-2.5\,dBm$ at a DC photocurrent of $30\,mA$. At $200\,GHz$ the available power still amounts to $-9\,dBm$, and even at $400\,GHz$ a power of $-32\,dBm$ was detected. Due to the lack of calibration data beyond $170\,GHz$, these data were not calibrated and the output power can be anticipated to be somewhat higher due to the disregarded losses in the experimental setup.

Interestingly, at these high frequencies the maximum power did not improve by increasing the bias voltage, as fig. 70b illustrates. On the contrary, the available power decreased for a reverse bias $> 2.5\,V$, which may well be attributed to the field-dependent drift velocity of the photogenerated electrons. As for low electrical fields the electrons' drift velocity increases linearly, an optimum bias around $2\,V$ is necessary

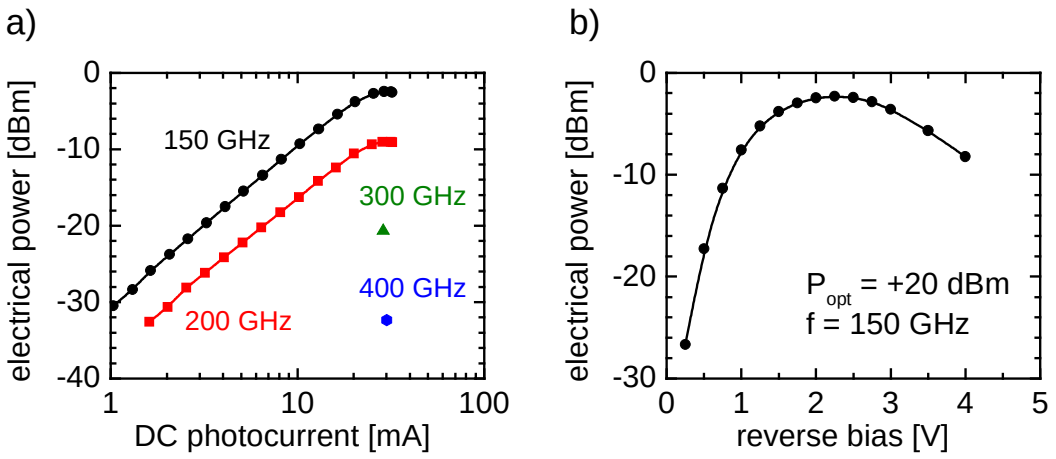

Figure 70: a) Detected electrical power versus photocurrent at $150\,GHz$, $200\,GHz$, $300\,GHz$ *and* $400\,GHz$ *at* $V_{bias} = -2\,V$, *b) power versus reverse bias at* $150\,GHz$ *and* $+20\,dBm$ *optical input power (P-TWPD from TWPD#5).*

to exploit fully the velocity overshoot. At higher bias the drift velocity decreases again and approaches its saturation value. This result was also confirmed by measurements of devices from a wafer without DDR structure. Furthermore we found, that the bias for the highest output power decreases when applying lower optical input powers.

From the above results, the travelling wave photodetector demonstrates its promising potential for the use in high-power submm- and THz-systems. Hence, the TWPD with parallel optical feed clearly outperforms both the considered S-TWPD and miniaturized lumped element PD, which achieved power levels of only $-10\,dBm$ at $110\,GHz$ and $-11\,dBm$ at $150\,GHz$, respectively (both devices from TWPD#5).

5.7.2. Time domain

The results from the previous section characterize the saturation effects for a sinusoidal optical input signal. However, for digital applications, the available peak voltage of pulsed input signals at maintained pulsewidth is of particular interest.
Again, the devices from section 5.6.2 are compared. At the applied bias of $-2\,V$ the

mean photocurrents were linear for all considered input powers. Figure 71a depicts the detected pulse response of the P-TWPD in comparison with the results of two lumped element PDs at a constant output peak voltage of $0.53\,V$. Depending on the responsivity of the individual detector, the average optical input power was adjusted to values between $+12\,dBm$ and $+15\,dBm$. At these high input powers, the TWPD exhibits superior performance with regard to pulsewidth, fall time and undershoot, which amount to $8\,ps$, $4\,ps$ and 4%, respectively. While the miniaturized PD is already saturated, the PD with an area of $100\,\mu m^2$ shows a considerable increased undershoot of 13%. In contrast, the TWPD is still operated in its linear regime and exhibits only small ringing, due to its high-power handling capability, broadband impedance match and linear phase response. Its fall time as well as FWHM remains below $10\,ps$ up to output amplitudes of $0.8\,V$ and therefore compares well with the $100\,\mu m^2$-PD (fig. 71b).

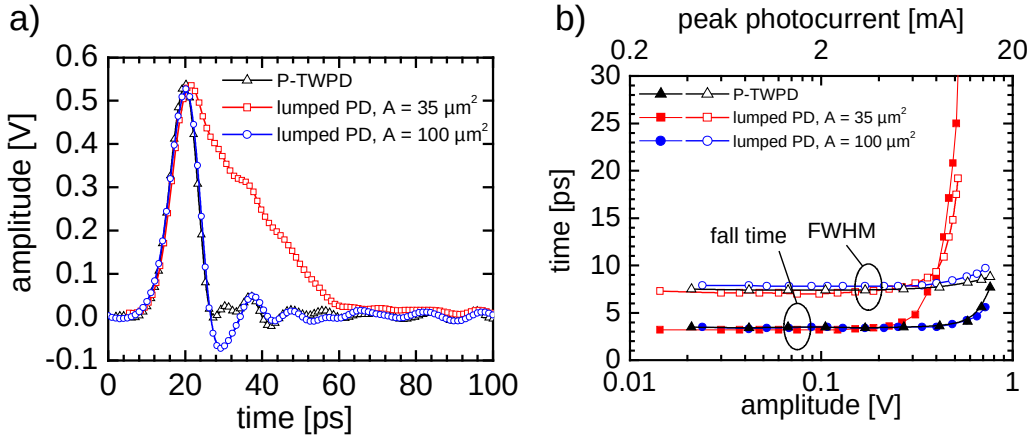

Figure 71: a) Electrical pulse responses of lumped element PDs and a P-TWPD at high optical input power ($V_{bias} = -2\,V$), b) fall time (90%/10%) and FWHM versus output amplitude and peak photocurrent (top axis) at $50\,\Omega$ load of the same photodetectors (TWPD#5).

5.8. Chip packaging and system tests

In order to evaluate the fabricated TWPD in a system-related environment, it is necessary to realise a robust packaging of the chip. Following HHI's established packaging concept [78, 79], a P-TWPD chip ($G = 22\,\mu m$, $d = 90\,\mu m$) from wafer TWPD#5 was assembled into a standard housing equipped with a 1 mm coaxial output connector and a fibre pigtail.

Figure 72a shows a top view of the mounted chip. The chips's output pads are connected by multiple short bonding wires with a following low-loss output CPW ($\alpha = 0.25\,dB/mm$ at $100\,GHz$) on quartz substrate with $\varepsilon_r = 3.8$ (see fig. 72b). This CPW provides the adequate interface to the 1 mm coaxial connector (Agilent 11923A), which is specified for operation up to $110\,GHz$. The transition to the connector's inner centre pin and outer conductor is made by highly conductive epoxy, ensuring a low series resistance ($< 1\,\Omega$). For convenient and safe biasing, the module is provided with a PI-filtre, Zener diode (4V3) and additional capacitors (10 and $100\,pF$), blocking the bias path to ground. Optical coupling is done by fixing a cleaved

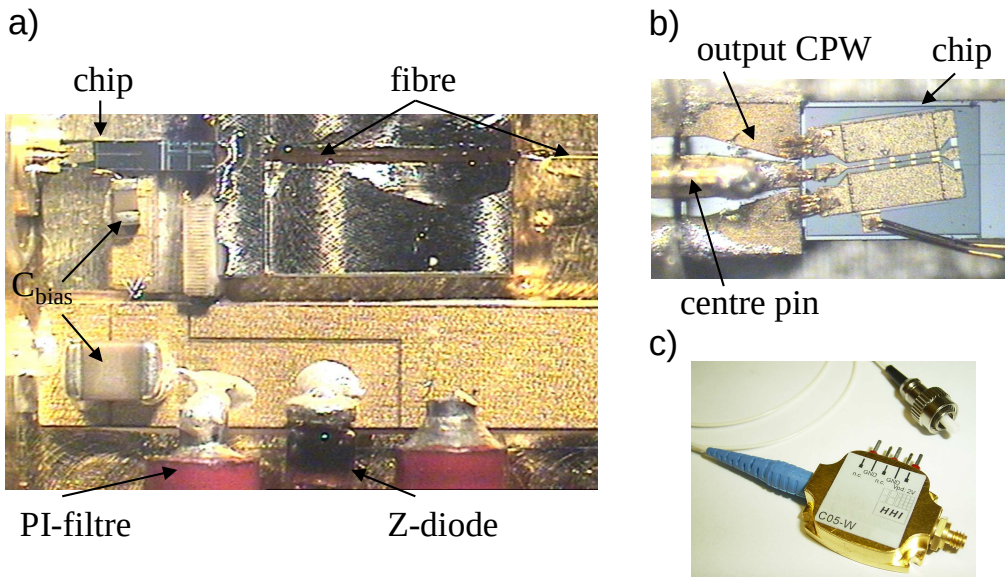

Figure 72: a) Mounted chip in the module, b) chip with output CPW, c) TWPD module with 1 mm connector.

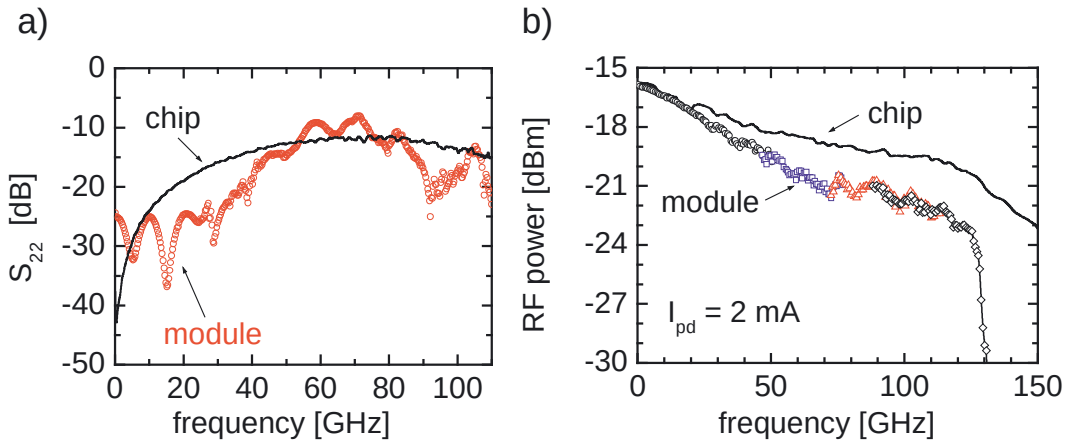

Figure 73: a) Magnitude of S_{22} of the fully packaged P-TWPD (red circles) and a comparable on-wafer measurement (solid line), b) frequency response of the P-TWPD module (symbols) and result from on-wafer measurement of the identical chip (solid line). All measurements at $V_{bias} = -2\,V$.

fibre directly at the chip's antireflection-coated waveguide facet by UV curable epoxy. In good accordance with the chip-based measurement a responsivity of $0.24\,A/W$ with a PDL of $0.17\,dB$ was obtained after packaging. The finished TWPD module is shown in fig. 72c.

The result of the one-port S_{22} measurement is illustrated by the red circles in fig. 73a. A return loss of almost $10\,dB$ over the entire frequency range can be observed. However, the comparison with an on-wafer measurement of a comparable P-TWPD chip from TWPD#5 (solid line in fig. 73a) shows substantial differences and indicates the impact of the packaging. Especially at low frequencies the chip exhibits a $15\,dB$-lower S_{22}, which gives rise to the assumption, that an additional series resistance in the signal path exceeds $2\,\Omega$ in this particular package. The frequency characteristic of the TWPD module was determined by the optical heterodyne method described in section 5.5.1. The influence of the adapters used in the experimental setup were taken into account by applying eq. 74 to the measured values. Only above $110\,GHz$ - the calibration data of the employed coax-to-waveguide adapter (1 mm to WR10, Agilent W281D) - was not available; whereby the calibration curve was simply extrapolated

to higher frequencies.

The symbols in fig. 73b show the frequency response of the TWPD module at $V_{bias} = -2\,V$. The optical input power was set to $+9.2\,dBm$ which led to a DC photocurrent of $2\,mA$. An excellent agreement of the measured characteristics can be observed in the overlapping frequency ranges of different measurement ranges, indicated by symbols of different colors. From the plot, a 3 dB bandwidth of $45\,GHz$ can be determined. At $120\,GHz$ signal frequency, the response has dropped only by $7\,dB$. At higher frequencies, pronounced losses can be observed which lead to a clear cut-off of the response at $125\,GHz$. The cut-off can be attributed in part to the coax-to-waveguide adapter in the setup, which has not been calibrated correctly, and to the coaxial connector, which is supposed to support the first higher order waveguide mode at frequencies above $130\,GHz$.

The solid line in fig. 73 represents the fully calibrated on-wafer measurement of the identical chip and reveals a bandwidth of $70\,GHz$. By comparison of the two measurements in the diagram, the package-related losses can be identified to be $1\,dB$ around $50\,GHz$ and roughly $2\,dB$ at $100\,GHz$. In contrast to previous PD modules using a similar packaging technique [76], these values appear somewhat higher. Further work has to be done in order to explain in detail the origin of the high-frequency losses of this particular module.

In view of the operation in high-bitrate transmission systems, the TWPD module was employed in back-to-back transmission experiments at various bitrates. The experimental setup is shown in fig. 74. The transmitter consists of a $10\,GHz$ mode locked semiconductor laser with a pulse width of $1.7\,ps$ and an $10\,GHz$ amplitude modu-

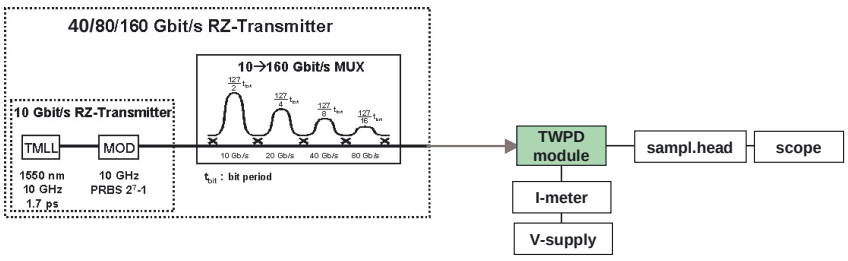

Figure 74: Experimental setup for eye diagram measurements.

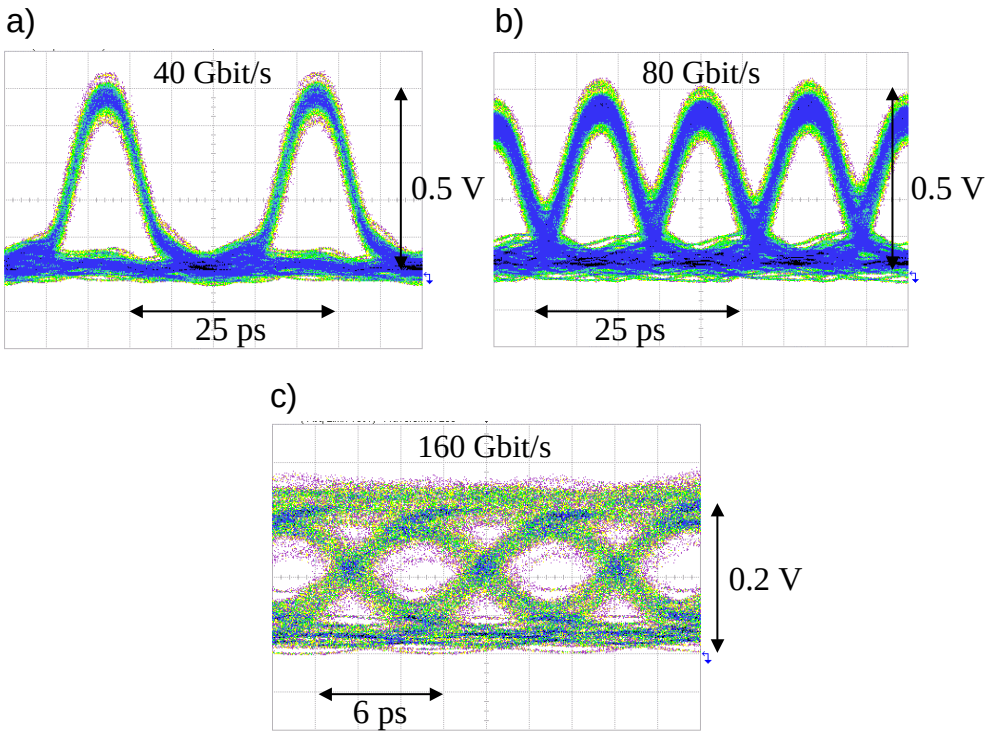

Figure 75: Electrical eye diagrams at $40\,Gbit/s$ (a), $80\,Gbit/s$ (b) and $160\,Gbit/s$ (c) RZ modulation format detected by the TWPD module ($V_{bias} = -2\,V$).

lator. By using optical time domain multiplexing techniques, a return-to-zero (RZ) modulated data stream (pseudo random bit sequence) with $2^7 - 1$ pattern length was generated with a bitrate of $40\,Gbit/s$, $80\,Gbit/s$ and $160\,Gbit/s$ [80]. On the receiver side the TWPD module and an electrical sampling scope (Agilent 86100B with Agilent 86118A) with a bandwidth of $70\,GHz$ were employed. Figure 75a and b show the received 40 and $80\,Gbit/s$ electrical eye patterns at average optical input powers of $+12\,dBm$ and $+14.4\,dBm$, respectively. The eye diagrams are opened widely with peak voltages of $0.5\,V$, which are twice as much as required by state-of-the-art demultiplexing electronics. The slight asymmetry between adjacent eye patterns is attributed to some minor imbalances in the optical multiplexer. Figure 75c shows the detected $160\,Gbit/s$ RZ data stream at $+15.6\,dBm$ optical input power. Due to the insufficient bandwidth of the sampling head and the TWPD module (overall 3 dB bandwidth $< 40\,GHz$) one observes an RZ-to-NRZ conversion and a significantly

reduced inner eye opening. However, as the bandwidth of the P-TWPD chip is considerably higher, one can expect a better performance at $160\,Gbit/s$ by an improved packaging in a forthcoming module.

6. Conclusion

In the work at hand, novel periodic travelling wave photodetectors based on discrete miniaturized p-i-n waveguide-integrated photodiodes with serial and parallel optical feed are studied. Therefore, the following theoretical aspects have been addressed:

- A bandwidth-model for lumped element PDs taking RLC- and carrier transit-effects into account was applied, in order to determine the bandwidth-limits of discrete photodiodes.
- Based upon a commercial software, a simulation procedure for calculating quantitatively the responsivity of evanescently-coupled waveguide-integrated PDs was developed.
- The theoretical treatment of the Bragg-effect and the phase mismatch in the periodic TWPD gave insight into the bandwidth constraints and revealed a bandwidth limit of a terminated TWPD, which equals twice the RC-limit of the single unterminated lumped element PD.
-An equivalent circuit based on discrete PD cells was designed in order to predict and model the O/E transfer function of a TWPD.

Periodic TWPDs based on two-layered coplanar transmission lines were designed, with special regard to an impedance and velocity match.
The optimization of the optical properties led to the introduction of multimode waveguides, which allow the retention of the proven concept of singlemode waveguides and the established design of the mode field transformer for integrated optical networks. By exploiting mode beating effects in multimode waveguides, the low-capacitance miniaturized lumped element photodiode as well as both considered types of TWPDs benefit significantly in terms of an increased quantum efficiency. In the case of the parallel type a low-loss 1×4 multi mode interference splitter has been successfully designed.
The characterization of the fabricated devices includes static, pulse, high-power and high-frequency optical heterodyne measurements. An important task of the present work was the extension of the optical heterodyne measurement setup - now allowing

calibrated measurements in the frequency range up to $170\,GHz$.
In table 11, the experimental results of the investigated travelling wave photodetectors are summarized. In conclusion, the periodic TWPD with integrated termination resistor reveals a responsivity up to $0.45\,A/W$ with a PDL around $0.3\,dB$. The return loss is determined to be better than $10\,dB$ up to $110\,GHz$, demonstrating an ultra-broadband impedance match to the load. The measured frequency responses exhibit bandwidths up to $83\,GHz$ and show a superior performance at ultra-high frequencies when compared to a lumped element PD due to the travelling wave effect. As some of the devices suffered from process-related loading effects, the bandwidth can be expected to be even higher in a forthcoming run. In the time domain, an

	TWPD#2		TWPD#4		TWPD#5	
$d_{abs}\ [nm]$	430		200		200, d_{drift} : 150 nm	
	S-TWPD	P-TWPD	S-TWPD	P-TWPD	S-TWPD	P-TWPD
$R\ [A/W]$	0.41	0.31	0.45	0.32	0.41	0.26
$PDL\ [dB]$	1	1.3	0.3	0.4	0.2	0.2
$f_{3dB}\ [GHz]$	66	80	61	83	68	75
f_{10dB} $[GHz]$	128	139	130	170	140	183
$\eta \cdot f_{3dB}$ $[GHz]$	22	20	22	21	22	16
$P_{max}^{out}\ [\mu W]$		316@150			80@110	562@150
$S_{22}\ [dB]$	< -15	< -15	< -10	< -10	< -10	< -10
$I_{dark}\ [nA]$	< 3	< 3	≈ 2500	≈ 2500	≈ 10000	≈ 10000

Table 11: Performance of investigated photodetectors at 2 V reverse bias and $1.55\,\mu m$ wavelength, all devices with integrated termination resistor. f_{10dB} denotes the frequency at which the electrical output power has dropped by 10 dB below the power value at DC. The maximum (saturated) output power P_{max}^{out} at the specified frequency in $[GHz]$ was partly obtained at higher reverse bias voltages. The data on the magnitude of S_{22} refer to a frequency range up to $110\,GHz$.

	TWPD#5
d_{abs} $[nm]$	200 ($d_{drift} = 150\,nm$) PD with $A = (4 \times 7)\,\mu m^2$
R $[A/W]$	0.39
PDL $[dB]$	0.5
f_{3dB} $[GHz]$	123
f_{10dB} $[GHz]$	> 190
$\eta \cdot f_{3dB}$ $[GHz]$	38
P_{max}^{out} $[\mu W]$	80@150
S_{22} $[dB]$	< -8
I_{dark} $[nA]$	800

Table 12: Performance of the investigated lumped element photodetector with integrated termination resistor from TWPD#5 at 2 V reverse bias and $1.55\,\mu m$ wavelength.

instrument-limited pulsewidth of $8\,ps$, an unsaturated pulse peak voltage of $0.5\,V$ and negligible undershoot are demonstrated. System experiments employing a fully packaged P-TWPD proved the suitability of the travelling wave photodetector for the use in optical frontends at bitrates in excess of $80\,Gbit/s$. These characteristics of the fabricated TWPD reveal a substantial improvement as a comparison with the data of previously published long-wavelength travelling wave photodetectors in table 2 shows. In terms of the bandwidth and available output power, the TWPD with parallel optical feed clearly outperforms the S-TWPD and the also considered miniaturized lumped element PD. Although a record bandwidth for waveguide-integrated photodiodes of $145\,GHz$ was obtained from a discrete $4 \times 7\,\mu m^2$-photodetector (TWPD#4 with $d_{abs} = 200\,nm$), this device suffers from poor high-power capability. In table 12, the results of a $4 \times 7\,\mu m^2$-PD from wafer TWPD#5 are summarized. Here, the maximum available electrical output power reached only $80\,\mu W$ at $150\,GHz$. For comparison, a P-TWPD from the same wafer showed an output power of $562\,\mu W$ at $150\,GHz$. By the above results, in particular the travelling wave photodetector with parallel

optical feed demonstrates its promising potential for the use in high-speed and high-power digital and analogue applications up to THz-frequencies. By eliminating the process-related loading effects in forthcoming process runs, the current design should enable 3 dB bandwidths in excess of $100\,GHz$.

7. Appendix

7.1. Epitaxial layer stack

function	compound	$\lambda_g\,[\mu m]$	$d\,[nm]$	dopant	$N\,[cm^{-3}]$
p-contact	p^+-$In_{0.53}Ga_{0.47}As$	1.65	80	Zn	1.0 E+19
grading	p-$InGa_{0.3}As_{0.64}P$	1.33	5	Zn	5.0 E+18
cladding	p-$InGa_{0.18}As_{0.39}P$	1.15	410	Zn	1.0 E+18
spacer	p-$InGa_{0.18}As_{0.39}P$	1.15	30	Zn	5.0 E+17
grading	p-$InGa_{0.34}As_{0.73}P$	1.3	5	Zn	1.0 E+17
absorption	$In_{0.53}Ga_{0.47}As$	1.65	200		n.i.d.
n-contact	n^+-$InGa_{0.3}As_{0.64}P$	1.33	450	Si	2.0 E+18
waveguide rib	s.i. $InGa_{0.11}As_{0.25}P$	1.06	205	Fe	4.4 E+16
etch stop	s.i. InP	0.92	20	Fe	4.4 E+16
waveguide	s.i. $InGa_{0.11}As_{0.25}P$	1.06	820	Fe	4.4 E+16
diluted waveguide	s.i. InP/InGaAsP		4500	Fe	4.4 E+16
substrate	s.i. InP	0.92	500000	Fe	4.4 E+16

Table 13: Vertical layer stack of TWPD#4. d denotes the layer thickness, N stands for the doping concentration.

function	compound	$\lambda_g\,[\mu m]$	$d\,[nm]$	dopant	$N\,[cm^{-3}]$
p-contact	$In_{0.53}Ga_{0.47}As$	1.65	80	Zn	1.0 E+19
grading	$InGa_{0.3}As_{0.64}P$	1.33	5	Zn	5.0 E+18
cladding	$InGa_{0.18}As_{0.39}P$	1.15	410	Zn	5.0 E+17
spacer	p-$InGa_{0.18}As_{0.39}P$	1.15	30	Zn	1.0 E+17
grading	p-$InGa_{0.34}As_{0.73}P$	1.3	5	Zn	1.0 E+17
absorption	$In_{0.53}Ga_{0.47}As$	1.65	200		n.i.d.
drift	$InGa_{0.3}As_{0.64}P$	1.33	150		n.i.d.
n-contact	n^+-$InGa_{0.3}As_{0.64}P$	1.33	300	Si	2.0 E+18
waveguide rib	s.i. $InGa_{0.11}As_{0.25}P$	1.06	205	Fe	4.4 E+16
etch stop	s.i. InP	0.92	20	Fe	4.4 E+16
waveguide	s.i. $InGa_{0.11}As_{0.25}P$	1.06	820	Fe	4.4 E+16
diluted waveguide	s.i. InP/InGaAsP		4500	Fe	4.4 E+16
substrate	s.i. InP	0.92	500000	Fe	4.4 E+16

Table 14: Vertical layer stack of TWPD#5 with dual depletion region. d denotes the layer thickness, N stands for the doping concentration.

7.2. Two-layered coplanar waveguide

In eq. 52, ϵ_e is defined by:

$$\epsilon_e = \frac{1+\varepsilon_{r1}}{2} + Q\,(\varepsilon_{r2} - \varepsilon_{r1}) \tag{76}$$

The filling factor Q is:

$$Q = \frac{1}{2}\,\frac{\frac{K(k_2)}{K'(k_2)}}{\frac{K(k_1)}{K'(k_1)}} \tag{77}$$

and is not a function of the type of the dielectric interfaces in this approximation. $K(k)$ is the complete elliptic integral of the first kind and its associated complement $K'(k) \equiv K(k')$, defined as [58],

$$\begin{aligned} K(k) &= \int_0^{\frac{\pi}{2}} \frac{d\psi}{\sqrt{1-k^2\sin^2(\psi)}} \\ k' &= \sqrt{1-k^2} \end{aligned} \tag{78}$$

The arguments are given by:

$$\begin{aligned} k_1(G,W) &= \frac{W+\delta}{W+\delta+2\,(G-\delta)} \\ k_2(h_2,G,W) &= \frac{\sinh(\pi\,\frac{W+\delta}{4\,h_2})}{\sinh(\pi\,\frac{\frac{W+\delta}{2}+G-\delta}{2\,h_2})} \end{aligned} \tag{79}$$

and include the effect of metal thickness t of the CPW expressed by

$$\delta = 1.25\,\frac{t}{\pi}\,(1+\ln(3.8\,\pi\,\frac{W}{t})) \tag{80}$$

In order to compute the ratio $K(k)/K'(k)$ a simple relation may be used [59],

$$\begin{aligned} \frac{K(k)}{K'(k)} &= \frac{\pi}{\ln[2(1+\sqrt{k'})/(1-\sqrt{k'})]} \quad for\ 0 \le k \le 0.707 \\ \frac{K(k)}{K'(k)} &= \frac{1}{\pi}\ln[2(1+\sqrt{k})/(1-\sqrt{k})] \quad for\ 0.707 \le k \le 1 \end{aligned} \tag{81}$$

The expressions (81) are accurate to within 3 parts per million.

7.3. Derivation of the Bragg-frequency f_{bragg}

Figure 76a depicts the lumped element equivalent circuit, represented as a T-network, of one section of a capacitively-loaded transmission line (compare fig. 24c). Its corresponding two-port network in fig. 76b consists of two series elements $Z_S/2$ and the shunt element Y_P with $Z_S = (L'\,d)$ and $Y_P = (C'\,d + C_{pd})$. The terminal voltages and currents are denoted as V_1 and I_1 at the input and V_2 and I_2 at the output. The $ABCD$ transmission matrix $\mathbf{T}$ relates the terminal voltages and currents of the two-port via the following equation [54],

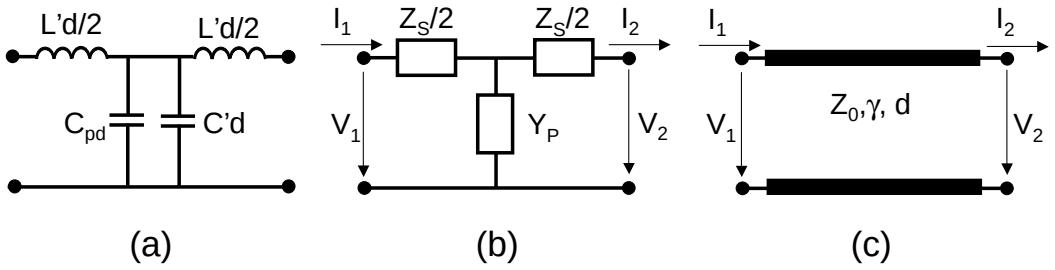

Figure 76: a) T-network representing one section of the capacitively-loaded CPW, b) corresponding two-port, c) two-port transmission line.

$$\begin{pmatrix} V_1 \\ I_1 \end{pmatrix} = \mathbf{T} \times \begin{pmatrix} V_2 \\ I_2 \end{pmatrix} \tag{82}$$

For the simple cascaded network in fig. 76b, the matrix T is determined by

$$\mathbf{T} = \mathbf{T_Z} \times \mathbf{T_Y} \times \mathbf{T_Z} \tag{83}$$

with the $ABCD$ matrices of the series and shunt elements $\mathbf{T_Z}$ and $\mathbf{T_Y}$:

$$\mathbf{T_Z} = \begin{pmatrix} 1 & Z_S/2 \\ 0 & 1 \end{pmatrix}, \quad \mathbf{T_Y} = \begin{pmatrix} 1 & 0 \\ Y_P & 1 \end{pmatrix} \tag{84}$$

Making use of eq. 83 and 84, equation 82 can be written as:

$$\begin{aligned} V_1 &= V_2 \left(1 + \frac{Y_P\, Z_S}{2}\right) + I_2\, Z_S \left(1 + \frac{Y_P\, Z_S}{4}\right) \\ I_1 &= V_2\, Y_P + I_2 \left(1 + \frac{Y_P\, Z_S}{2}\right) \end{aligned} \tag{85}$$

In order to apply these two-port equations to a transmission line, the coefficients have to be determined by comparison with the coefficients of the solution of the transmission line in fig 76c. The latter is given by [81]:

$$\begin{aligned} V_1 &= V_2\, \cosh(\gamma\, d) + I_2\, Z_0\, \sinh(\gamma\, d) \\ I_1 &= \frac{V_2}{Z_0}\, \sinh(\gamma\, d) + I_2\, \cosh(\gamma\, d) \end{aligned} \tag{86}$$

Here Z_0 and $\gamma = (\alpha + i\,\beta)$ stand for the transmission line's characteristic impedance and propagation constant, respectively. The comparison of eq. 85 and 86 and using the relation $\tanh(x/2) = (\cosh(x) - 1) \cdot (\sinh(x))^{-1}$, yield:

$$\cosh(\gamma\, d) = 1 + \frac{Y_P\, Z_S}{4} \tag{87}$$

$$Y_P = \frac{1}{Z_0}\, \sinh(\gamma\, d) \tag{88}$$

$$Z_S = 2\, Z_0\, \tanh(\gamma\, d) \tag{89}$$

By combining the above equations and replacing Z_S and Y_P with the circuit elements, an expression for the characteristic impedance Z_0 of the two-port can be derived:

$$Z_0 = \sqrt{\frac{Z_S}{Y_P} \cdot \left(1 + \frac{Z_S\, Y_P}{4}\right)} = \sqrt{\frac{L'\, d}{C'\, d + C_{pd}}} \cdot \sqrt{1 - \frac{\omega^2\, L'\, d\, (C' d + C_{pd})}{4}} \tag{90}$$

Thereby it is assumed, that the two-port networks are terminated at both terminals with their characteristic impedance.
The Bragg-frequency ω_{bragg} of the network can be defined as:

$$\omega_{bragg} = \frac{2}{\sqrt{L'\, d\, (C'\, d + C_{pd})}} \tag{91}$$

or, with $\omega = 2\pi f$,

$$f_{bragg} = \frac{1}{\pi\, \sqrt{L'\, d\, (C'\, d + C_{pd})}} \tag{92}$$

Employing the definition of ω_{bragg} in eq. 90 yields:

$$Z_0 = \sqrt{\frac{L'}{C' + \frac{C_{pd}}{d}}} \cdot \sqrt{1 - \frac{\omega^2}{\omega_{bragg}^2}} \tag{93}$$

For $\omega << \omega_{bragg}$, Z_0 is basically given by $\sqrt{\frac{L'}{C' + \frac{C_{pd}}{d}}}$ in agreement with what has been derived for a transmission line in eq. 54 in section 3.3. For frequencies approaching ω_{bragg} the device can not be described as a transmission line anymore and the periodic nature of the device is revealed due to Bragg-reflections.

The expression for the phase velocity v_0, can be obtained in a similar way by employing eq. 87 using the identity $\cosh(\gamma\, d) = \cosh(\alpha\, d)\, cos(\beta\, d) + i\, \sinh(\alpha\, d)\, \sin(\beta\, d)$. Since we describe a lossless line, it is $\alpha = 0$, which leads to

$$\cosh(\gamma\, d) = \cos(\beta\, d) = 1 - 2\,\frac{\omega^2}{\omega_{bragg}^2} \tag{94}$$

where the definition of the Bragg-frequency in eq. 91 has been used.
With $\beta = \omega/v_0$ and the series expansion

$$\arccos(z) = \sqrt{2}\,\sqrt{1-z}\left[1 + \frac{1-z}{12} + \frac{3}{160}\,(1-z)^2 + ...\right],\ \ for\ |z-1| < 1 \tag{95}$$

the phase velocity is:

$$v_0 = \frac{1}{\sqrt{L'\,(C' + \frac{C_{pd}}{d}) \cdot \left(1 + \frac{\omega^2}{6\,\omega_{bragg}^2} + ...\right)}} \tag{96}$$

Again, the comparison with the result in eq. 55 reveals agreement for $\omega << \omega_{bragg}$. For $\omega \rightarrow \omega_{bragg}$ the periodicity of the network becomes visible in terms of a decreasing phase velocity.
It should be mentioned, that by using a π-network in fig. 76b the same result for ω_{bragg} is obtained.

7.4. Transmission matrix of a lossy transmission line

The $ABCD$ transmission matrix of a lossy transmission line with length L is given by [53, 54]:

$$\mathbf{T_{TL}} = \begin{pmatrix} A_{TL} & B_{TL} \\ C_{TL} & D_{TL} \end{pmatrix} = \begin{pmatrix} \cosh(\gamma L) & Z\sinh(\gamma L) \\ \frac{\sinh(\gamma L)}{Z} & \cosh(\gamma L) \end{pmatrix} \tag{97}$$

The transmission line parameters γ, and Z can be written as:

$$\gamma = \frac{\cosh^{-1}(A_{TL})}{L} \tag{98}$$

$$Z = \sqrt{\frac{B_{TL}}{C_{TL}}} \tag{99}$$

Note, that the matrix elements are complex numbers and therefore equation (98) has an infinite number of solutions with period $i(\arg(A_{TL})+2\pi k)$ with $k = (0, \pm 1, \pm 2, ..)$. The correct branch can be identified by considering the properties of a real transmission line, which are $\alpha > 0$, $\beta > 0$, zero phase shift at zero frequency and a finite group velocity.
The $ABCD$ matrix elements are related to the S-parameters of the scattering matrix by the following conversions:

$$A_{TL} = \frac{(1 + S_{11})(1 - S_{22}) + S_{12}S_{21}}{2S_{21}} \tag{100}$$

$$B_{TL} = \frac{(1 + S_{11})(1 + S_{22}) - S_{12}S_{21}}{2S_{21}} \tag{101}$$

$$C_{TL} = \frac{(1 - S_{11})(1 - S_{22}) - S_{12}S_{21}}{2S_{21}} \tag{102}$$

$$D_{TL} = \frac{(1 - S_{11})(1 + S_{22}) + S_{12}S_{21}}{2S_{21}} \tag{103}$$

7.5. Process steps

The following process steps refer to the fabrication of TWPD#2 with the epitaxial layer structure given in table 3. Similar steps were applied to wafers #4 and #5.

1. *Zn-diffusion*
   - Deep in-diffusion of Zn (DIFF), depth: 150 nm, source: Zn_3As_2
2. *Formation of p-metal contacts*
   - Lithography (LITH) for lift-off process, mask: TWPD-PK
   - contact deposition (EBEV)
     Pt/Ti/Pt/Au/Pt with 30/100/500/2000/500 Å
3. *p-mesa etching*
   - LITH, mask: TWPD-PM
   - dry etching (RIE) of the following layers: p-contact, grading, cladding, grading.
   - wet etching (WCET) of the absorption layer
4. *n-mesa etching*
   - LITH, mask: TWPD-NM
   - dry etching of n-contact layer (RIE)
5. *Formation of n-metal contacts*
   - LITH, mask: TWPD-NK
   - contact deposition (EBEV)
     Ge/Ni/Ge/Ni/Au/Pt with 100/100/300/100/1500/250 Å
   - tempering
6. *Formation of vertically tapered ramp*
   - LITH, mask: TWPD-VM + TWPD-VO

- etching (CAIBE)

7. *Formation of rib waveguide*
   - LITH, mask: TWPD-WG
   - dry etching (RIE)
8. *Formation of fibre rib waveguide*
   - LITH, mask: TWPD-WF
   - dry etching (RIE)
9. *BCB spinning and patterning*
   - spinning dry-etch BCB
   - BCB curing
   - dry etching (RIE)
   - LITH, mask: TWPD-BCB
   - dry etching (RIE)
   - LITH for BCB vias
   - dry etching (RIE)
10. *Formation of lower plate for MIM capacitor*
    - LITH, mask: TWPD-UK
    - Deposition of metal
      Ti/Pt/Au with 200/500/2000 Å
11. *Deposition of MIM dielectric*
    - LITH, mask: TWPD-MIM
    - PECVD deposition of SiN_x (124 nm)
12. *NiCr resistor*

- LITH, mask: TWPD-NICR
- Co-evaporation of NiCr layer

13. *Lower metallization layer*

    - LITH, mask: TWPD-UM
    - Evaporation of metal layer
      Ti/Pt/Au with 200/1000/3000 Å

14. *Plating base*

    - LITH, mask: TWPD-SAL
    - Deposition of plating base
      Ti/Au with 50/1500 Å

15. *Gold-electro-plating*

    - LITH, mask: TWPD-GLM
    - Electro-plating, Au thickness: $3\,\mu m$
    - etching (CAIBE)

16. *Wafer cleaving*

17. *Anti-reflection coating*

    - Sputtering of TiO_x layer, thickness optimized for $1550\,nm$, $n_{fibre} = 1.46$, $n_{chip} = 3.18$, keeping a potential packaged assembly of the chip in mind.

7.6. Optical heterodyne microwave generation

The heterodyne detection scheme is based on the nonlinear relation between the incident electromagnetic field $\vec{E}^2$ of two laser signals with slightly different wavelengths and the generated photocurrent in the detector,

$$I_{pd} \propto P_{opt} \propto \vec{E}^2 \tag{104}$$

Considering the linear polarized signals of two laser sources with frequencies ω_1, ω_2 and a relative phase ϕ superimposed in a 3 dB coupler, the total electromagnetic field is:

$$\vec{E_{12}}(t) = \vec{e}_1 \, \hat{E}_1 \, \cos(\omega_1 t) + \vec{e}_2 \, \hat{E}_2 \, \cos(\omega_2 t + \phi) \tag{105}$$

Making use of $P_{opt}(t) = E_{12}^2 / Z_F$ with the free space impedance $Z_F = \sqrt{\mu_0 / \varepsilon_0}$ and assuming parallel polarizations leads to the incident total optical power:

$$\begin{aligned} P_{opt}(t) \;\; = \;\; & \frac{\hat{E}_1^2}{Z_F} \, (\frac{1}{2} + \frac{1}{2} \, cos(2 \, \omega_1 \, t)) \\ & + \frac{\hat{E}_2^2}{Z_F} \, (\frac{1}{2} + \frac{1}{2} \, cos(2 \, \omega_2 \, t)) && (106) \\ & + \frac{\hat{E}_1 \, \hat{E}_2}{Z_F} \, cos((\omega_1 - \omega_2) \, t - \phi) && (107) \\ & + \frac{\hat{E}_1 \, \hat{E}_2}{Z_F} \, cos((\omega_1 + \omega_2) \, t + \phi) && (108) \\ & && (109) \end{aligned}$$

After time averaging corresponding to $P_{1,2} = \hat{E}_{1,2}^2 / (2 \, Z_F)$, and cancellation of all contributions with modulation frequencies well above the detector bandwidth and vanishing mean value, one obtains the modulated photocurrent:

$$I_{pd}(\omega) \propto P_{opt}(\omega) = P_1 + P_2 + 2 \sqrt{P_1 \, P_2} \, cos((\omega_1 - \omega_2) t - \phi) \tag{110}$$

which consists of a DC and modulated part with a frequency of $\omega = |\omega_1 - \omega_2|$. Maximum (100 %) modulation depth is achieved by parallel states of polarizations and $P_1 = P_2$ of both laser input signals.

7.7. List of symbols

A	Active area $[m^2]$
α	Absorption constant $[m^{-1}]$
α_{eff}	Effective absorption constant $[m^{-1}]$
β_k	Mode propagation constant $[1/m]$
c	Vacuum velocity of light $[m/s]$
C'	Capacitance per unit length $[F/m]$
C_{pd}	Photodiode capacitance $[F]$
C_{pn}	pn junction capacitance $[F]$
C_{st}	Stray capacitance $[F]$
d	PD spacing on TL $[m]$
d_{abs}	Thickness absorption layer $[m]$
d_{drift}	Thickness drift layer $[m]$
d_o	PD spacing on optical waveguide $[m]$
d_{pd}	Thickness depletion layer $[m]$
E	Electrical field $[V/m]$
E_g	Bandgap energy $[eV]$
$\vec{E}_k$	Electric field mode profile $[V/m]$
E_{max}	Maximum electrical field at breakdown $[V/m]$
ε_0	Permittivity of free space $[A\,s/V\,m]$
ε_r	Dielectric constant $[1]$
ε_{eff}	Effective dielectric constant $[1]$
η	Internal quantum efficiency $[1]$
η_{ext}	External quantum efficiency $[1]$
f_{10dB}	-10 dB cut-off frequency $[Hz]$
f_{3dB}	Bandwidth, -3 dB cut-off frequency $[Hz]$
f_{bragg}	Bragg frequency $[Hz]$
f_r	Resonant frequency $[Hz]$
f_{RC}	RC limited bandwidth $[Hz]$
f_{RLC}	RLC limited bandwidth $[Hz]$

f_t	Transit time limited bandwidth $[Hz]$
G	Gap width $[m]$
G'	Conductivity per length $[S/m]$
γ	Propagation constant $[1/m]$
gd	group delay $[s]$
Γ_{xy}	Confinement factor $[1]$
h	Planck constant $[Js]$
$\vec{H}_k$	Magnetic field mode profile $[V/m]$
H_{pd}	Photodiode transfer function $[dB]$
H_{RLC}	Transfer function due to RLC-circuit $[dB]$
H_t	Transfer function due to transit effects $[dB]$
I	Energy density $[J/m^{-3}]$
I_{dark}	Photodiode dark current $[A]$
I_{pd}	Photocurrent $[A]$
J_{pd}	Photocurrent density $[A/m^2]$
λ	Wavelength in vacuum $[m]$
λ_g	Wavelength in vacuum equivalent to bandgap $[m]$
L	Matching layer protrusion length $[m]$
L_{pd}	Photodiode inductance $[H]$
l_{pd}	Photodiode length $[m]$
L'	Inductance per length $[H/m]$
L_π	Beating length $[m]$
μ_0	Magnetic field constant $[V\,s/A\,m]$
μ_e	Electron mobility $[m^2/V\,s]$
μ_h	Hole mobility $[m^2/V\,s]$
n	Refractive index $[1]$
$n_{eff,k}$	Mode effective refractive index $[1]$
$n(x)$	Electron density $[m^{-1}]$
N_D	Background doping level $[m^{-1}]$
ν	Frequency $[Hz]$
ω	Angular frequency $[Hz]$

$p(x)$	Hole density $[m^{-3}]$
ϕ_ω	Phase response $[rad]$
P_{opt}	Optical power $[W]$
P_{RF}	Electrical radio frequency power $[dBm]$
PDL	Polarization dependant loss $[dB]$
Q	Filling factor $[1]$
q	Electron charge $[C]$
R	Responsivity $[A/W]$
R'	Series resistance per length $[\Omega/m]$
R_p	Parallel resistance $[\Omega]$
R_{ideal}	Ideal responsivity $[A/W]$
R_l	Load resistance $[\Omega]$
R_{max}	Maximum responsivity $[A/W]$
R_{min}	Minimum responsivity $[A/W]$
R_o	Surface reflectance $[1]$
R_s	Series resistance $[\Omega]$
R_{term}	Termination resistance $[\Omega]$
R_{tot}	Total series resistance $[\Omega]$
R_{50}	50-Ohm resistance $[\Omega]$
t	Transmission line metallization thickness $[m]$
τ_e	Electron transit time $[s]$
τ_h	Hole transit time $[s]$
S_{ij}	Scattering parameter $[1]$
v	Transmission line phase velocity $[m/s]$
v_e	Drift velocity electron $[m/s]$
v_e^{sat}	Saturated drift velocity electron $[m/s]$
v_g^o	Optical group velocity $[m/s]$
v_h	Drift velocity hole $[m/s]$
v_0	TWPD electrical phase velocity $[m/s]$
v_h^{sat}	Saturated drift velocity hole $[m/s]$
v_{ph}	Phase velocity $[m/s]$

$\bar{v}$	Average carrier drift velocity $[m/s]$
V_b	Built-in voltage $[V]$
V_{bias}	External bias voltage $[V]$
W	Signal line width $[m]$
w_{pd}	Photodiode width $[m]$
Z	Transmission line characteristic impedance $[\Omega]$
Z_0	TWPD characteristic impedance [Ω]

7.8. List of abbreviations

AlGaAs	Aluminium Gallium Arsenide
APD	Avelanche photodiode
ARC	Anti-reflection coating
BCB	Benzocyclobuten
BP	Bandpass
BW	Bandwidth
CAD	Computer aided design
c.b.	Conduction band
CAIBE	Chemically assisted ion beam etching
CPW	Coplanar waveguide
CW	Continuous wave
DC	Direct current
DDR	Dual depletion region
DUT	Device under test
ECL	External cavity laser
ESA	Electrical spectrum analyser
EDFA	Erbium doped fibre amplifier
FMM	Film mode matching
FWHM	Full width at half maximum
GaAs	Gallium arsenide
GND	Ground
GSG	Ground signal ground
HHI	Heinrich-Hertz-Institut
InP	Indium phosphide
InGaAs	Indium gallium arsenide
InGaAsP	Indium gallium arsenide phosphide
O/E	Opto-electronic
LTG	Low temperature grown
MMI	Multimode interference

MIM	Metal insulator metal
MLL	Mode locked laser
MOVPE	Metal organic vapor phase epitaxy
MQW	Multi quantum well
MSM	Metal semiconductor metal
μ-PD	Micro-photodiode
NiCr	Nickel chrome
NRZ	Non-return-to-zero
NTT	Nippon telegraph and telephone corporation
OSA	Optical spectrum analyser
PD	Photodiode
PM	Powermeter
RC	Resistance capacitance
RF	Radio frequency
RIE	Reactive ion etching
RLC	Resistance inductance capacitance
RCE	Resonant cavity enhancement
RZ	Return-to-zero
SIG	Signal
SMF	Singlemode fibre
TE	Transversal electric
TEM	Transversal electromagnetic
TM	Transversal magnetic
TL	Transmission line
TLM	Transmission line method
TDM	Time division multiplexing
TWPD	Travelling wave photodetector
P-TWPD	TWPD with parallel optical feed
S-TWPD	TWPD with serial optical feed
TUB	Technische Universität Berlin
UCLA	University of California Los Angeles

UCSB	University of California Santa Barbara
UDE	Universität Duisburg Essen
UTC	Uni-travelling carrier
V	Voltage
v.b.	Valence band
VIM	Vertical impedance matching
VPD	Vertically illuminated photodiode
WDM	Wavelength division multiplexing
WG	Waveguide
WG-PD	Waveguide photodiode

References

[1] K. Schuh, B. Junginger, E. Lach, S. Vorbeck, R. Leppla, M. Schneiders, "8x85.4 Gbit/s WDM Field Transmission over 421 km SSMF Link Applying an 85.4 Gbit/s ETDM receiver," Proceedings 31st European Conference on Optical Communication (ECOC 2005), Glasgow, Scotland, 25-29. Sept. 2005, vol. 3, We2.2.2, pages: 379-380.

[2] P. J. Winzer, G. Raybon, M. Duelk, "107 Gb/s optical ETDM transmitter for 100 G Ethernet transport," Proceedings 31st European Conference on Optical Communication (ECOC 2005), Glasgow, Scotland, 25-29. Sept. 2005, vol. 6, Th4.1.1, pages: 1-2.

[3] G. C. Gupta, R. E. Tench, O. Mizuhara, L. L. Wang, N. N. Dang, N. Chand, B. Mason, A. Ougazzaden, and C. W. Lentz, "3.2 Tbit/s (40 x 80 Gb/s) transmission over 1000 km with 100 km span (25 dB loss) and 0.8 bit/s/Hz of spectral efficiency," Techn. Digest Optical Fiber Communication (OFC 2002), March 17-22, 2002, Anaheim, CA, USA, pages: 6-8.

[4] K. Schuh, M. Schmidt, E. Lach, B. Junginger, A. Klekamp, G. Veith, P. Sillard, "4 x 160 Gb/s DWDM/OTDM transmission over 3 x 80 km TeraLight - Reverse TeraLight fibre," Proceedings 28th European Conference on Optical Communication (ECOC 2002), September 8-12, 2002, Copenhagen, Denmark, paper 2.1.2.

[5] H. Ito, T. Furuta, F. Nakajima, K. Yoshino, T. Ishibashi, "Photonic generation of continuous THz wave using uni-traveling-carrier photodiode," Journal of Lightwave Technology, Vol. 23, No: 12, December 2005, pages: 4016 - 4021.

[6] J. Payne, J. Shillue, B. Vaccari, "Photonic techniques for use on the Atacama Large Millimeter Array," International Topical Meeting on Microwave Photonics, 1999 (MWP '99), 17-19 Nov. 1999, vol. 1, pages: 105 - 108.

[7] S. Ramo, "Currents induced by electron motion," Proceedings of the I. R. E., September 1939, pages: 584-585.

[8] S. M. Sze, "Physics of semiconductor devices," John Wiley and Sons, 1981.

[9] S.Adachi, "Physical Properties of III-V Semiconductor compounds," John Wiley and Sons, 1992.

[10] New Semiconductor Materials: Characteristics and Properties, Ioffe Physico-Technical Institute, 26 Polytekhnicheskaya, St. Petersburg 194021, Russian Federation (www.ioffe.rssi.ru/SVA/NSM/) .

[11] K. Kato, S. Hata, K. Kawano, and A. Kozen, "Design of Ultrawide-Band, High-Sensitivity p-i-n Photodetectors," IEICE Trans. Electron., Vol.E76-C, No. 2, February 1993, pages: 214-221.

[12] K. J. Williams, "Comparisons between dual-depletion.region and uni-travelling-carrier p-i-n photodetectors," IEE Proc.-Optelectron., Vol. 149, No. 4,August 2002, pages: 131-137.

[13] K. Kato, "Ultrawide-Band/High-Frequency Photodetectors," IEEE Trans. on Microwave Theory and Techniques, vol. 47, no. 7, July 1999, pages: 1265-1281.

[14] M. Dentan and B. Cremoux, "Numerical Simulation of the Nonliniear Response of a p-i-n Photodiode Under High Illumination," J. Lightwave Technol., vol. 8, no.8, August 1990, pages: 1137-1144.

[15] T. Ishibashi, T. Furuta, H. Fushimi, S. Kodama, H. Ito, T. Nagatsuma, N. Shimizu, Y. Miyamoto, "InP/InGaAs Uni-Traveling-Carrier Photodiodes," IEICE Trans. Electron., Vol. E83-C, No. 6, June 2000, pages: 938-949.

[16] Y. Muramoto, K. Yoshino, S. Kodama, Y. Hirota, H. Ito and T. Ishibashi, "100 and 160 Gbit/s operation of uni-travelling-

carrier photodiode module," Electron. Lett., 40 (6), 2004, pages: 378-379.

[17] D. Kuhl, F. Hieronymi, E. Holger Böttcher, T. Wolf, D. Bimberg, J. Kuhl, and M. Klingenstein, "Influence of Space Charges on the Impulse Response of InGaAs Metal-Semiconductor-Metal Photodetectors," J. Lightwave Technol, VOL. 10, NO. 6, June 1992, pages: 753-759.

[18] J. C. Campbell, S. Demiguel, F. Ma, A. Beck, X. Guo, S. Wang, X. Zheng, X. Li, J. D. Beck, M. A. Kinch, A. Huntington, L. A. Coldren, J. Decobert, and N. Tscherptner, "Recent Advances in Avalanche Photodiodes," IEEE J. Selected Topics Quantum Electronics, VOL. 10, NO. 4, July/August 2004, pages: 777-787.

[19] Y.-G. Wey, K. Giboney, J. Bowers, M. Rodwell, P. Silvestre, P. Thiagarajan, G. Robinson, "110-GHz GaInAs/InP Double Heterostructure p-i-n Photodetectors," J. Lightwave Technol., vol. 13, no. 7, July 1995, pages: 1490-1499.

[20] I. Kimukin, N. Biyikli, B. Butun, O. Aytur, S. M. nl, E. Ozbay, "InGaAs-Based High-Performance p-i-n Photodiodes," IEEE Photon. Technol. Lett., vol. 14, no. 3, March 2002, pages: 366-368.

[21] K. Kato, A. Kozen, Y. Maramoto, Y. Itaya, T. Nagatsuma, and M. Yaita, "110 GHz 50% efficiency mushroom mesa waveguide p-i-n photodiode for a 1.55 μm wavelength," IEEE Photon. Technol. Lett., vol. 6, no. 6, 1994, pages: 719-721.

[22] G. Unterbörsch, D. Trommer, A. Umbach, R. Ludwig, H.-G. Bach, "High-power performance of a high-speed photodetector," in Proc. 24th Eur. Conf. Optical Communication (ECOC 1998), pages: 67-68.

[23] S. Demiguel, N. Li, X. Li, X. Zheng, J. Kim, Joe C. Campbell, H. Lu, A. Anselm, "Very high-responsivity evanescently coupled photodiodes

integrating a short planar multimode waveguide for high-speed applications," IEEE Photon. Technol. Lett., vol. 15, no. 12, 2003, pages: 1761-1763.

[24] A. Umbach, D. Trommer, R. Steingrüber, S. Seeger, W. Ebert, G. Unterbörsch, "Ultrafast, high-power $1.55\,\mu m$ side-illuminated photodetector with integrated spot size converter," in Techn. Digest Optical Fiber Communication Conf. (OFC 2000), pages: 117-119.

[25] A. Beling, D. Schmidt, H.-G. Bach, G. G. Mekonnen, R. Ziegler, V. Eisner, M. Stollberg, G. Jacumeit, E. Gottwald, C.-J. Weiske, A. Umbach, "High power 1550 nm twin-photodetector modules with 45 GHz bandwidth based on InP," Tech. Digest Optical Fiber Commun. (OFC 2002) , March 17-22, 2002, Anaheim, CA, USA, paper WN4, pages: 274-275.

[26] A. Beling, H.-G. Bach, D. Schmidt, G.G. Mekonnen, R. Ludwig, S. Ferber, C. Schubert, C. Boerner, B. Schmauss, J. Berger, C. Schmidt, U. Troppenz and H.G. Weber, "Monolithically integrated balanced photodetector and its application in OTDM $160\,Gbit/s$ DPSK transmission," Electron. Lett., 2003, 39 (16), pages: 1204-1205.

[27] H. F. Taylor, O. Eknoyan, C. S. Park, K. N. Choi, and K. Chang, "Traveling wave photodetectors," Proc. SPIE-Int. Soc. Opt. Eng., vol. 1217, Optoelectronic Signal Processing for Phased Array Antennas II, 1990, pages: 59-63.

[28] K. S. Giboney, M. J. W. Rodwell, and J. E. Bowers, "Traveling-Wave Photodetectors," IEEE Photon. Technol. Lett., vol. 4, no. 12, December 1992, pages: 1363-1365.

[29] K. S. Giboney, R. L. Nagarajan, T. E. Reynolds, S. T. Allen, R. P. Mirin, M. J. W. Rodwell, and J. E. Bowers, "Travelling-Wave Photodetectors with 172-GHz Bandwidth and 76-GHz Bandwidth-Efficiency Product," IEEE Photon. Technol. Lett., vol. 7, no. 4, April 1995, pages: 412-414.

[30] Y.-J. Chiu, S. B. Fleischer, and J. E. Bowers, "High-Speed Low-Temperature-Grown GaAs p-i-n Traveling-Wave Photodetector," IEEE Photon. Technol. Lett., vol. 10, no. 7, July 1998, pages: 1012-1014.

[31] Y.-J. Chiu, S. Z. Zhang, S. B. Fleischer, J. E. Bowers, U. K. Mishra, "GaAs- based, 1.55 μm high speed, high saturation power, low-temperature grown GaAs pin photodetector," Electronics Letters, vol. 34, no. 12, June 1998, pages: 1253-1255.

[32] E. Dröge, E. H. Böttcher, St. Kollakowski, A. Strittmatter, O. Reimann, R. Steingrüber, A. Umbach, D. Bimberg, "Distributed MSM Photodetectors for Long-Wavelength Range," in Proc. 24th Eur. Conf. Optical Communication (ECOC 1998), pages: 57-58.

[33] M. S. Islam, T. Chau, S. Mathai, T. Itoh, M. C. Wu, D. L. Sivco, and A. Y. Cho, "Distributed Balanced Photodetectors for Broad-Band Noise Suppression," IEEE Trans. Microwave Theory Tech., vol. 47, pages: 1282-1287, July 1999.

[34] Y. Hirota, T. Ishibashi, H. Ito, "1.55 μm Wavelength Periodic Traveling-Wave Photodetector fabricated using Unitraveling-Carrier Photodiode Structures," J. Lightwave Technol., vol. 19, no.11, November 2001, pages: 1751-1758.

[35] S. Murthy, S.-J Kim, T. Jung, Z.-Z. Wang, W. Hsin, T. Itoh, M. C. Wu, "Backward-Wave Cancellation in Distributed Traveling-Wave Photodetectors," J. Lightwave Technol., Vol. 21, No. 12, December 2003, pages: 3071-3077.

[36] C. L. Goldsmith, G. A. Magel, R. J. Baca, "Principles and Performance of Travelling-Wave Photodetector Arrays," IEEE Trans. Microwave Theory Tech., vol. 45, no. 8, August 1997, pages: 1342-1349.

[37] S. Murthy, M. C. Wu, D. Sivco and A. Y. Cho, "Parallel feed travelling wave distributed pin photodetectors with integrated MMI couplers," Electronics Letters, vol. 38, no.2, 17th January 2002, pages: 78-80.

[38] S. Murthy, T. Jung, T. Chau, M. C. Wu, D. L. Sicvo, A. Y. Cho, "A Novel Monolithic Distributed Traveling-Wave Photodetector with Parallel Optical Feed," IEEE Photon. Techn. Letters, vol. 12, no. 6, June 2000, pages: 681-683.

[39] H. Ito, T. Furuta, S. Kodama, and T. Ishibashi, "InP/InGaAs uni-travelling-carrier photodiode with 310 GHz bandwidth," Electron. Lett., 36 (21), 2000, pages: 1809-1810.

[40] M. Achouche, V. Magnin, J. Harari, F. Lelarge, E. Derouin, C. Jany, D. Carpentier, F. Blache, and D. Decoster, "High Performance Evanescent Edge Coupled Waveguide Unitraveling-Carrier Photodiodes for $> 40 - Gb/s$ Optical Receivers," IEEE Photon. Technol. Lett., vol. 16, no. 2, Feb. 2004, pages: 584-586.

[41] L. Y. Lin, M. C. Wu, T. Itoh, T. A. Vang, R. R. Muller, D. L. Sivco, A. Y. Cho, "High-power high-speed photodetectors-design, analysis, and experimental demonstration," IEEE Trans. Microwave Theory and Techniques, Vol. 45, No. 8, August 1997, pages: 1320-1331.

[42] M. S. Islam, S. Murthy, T. Itoh, M. C. Wu, D. Novak, R. B. Waterhouse, D. L. Sivco, A. Y. Cho, "Velocity-matched distributed photodetectors and balanced photodetectors with p-i-n photodiodes," IEEE Trans. Microwave Theory and Techniques, Vol. 49, No. 10, August 2001, pages: 1314-1920.

[43] G. Unterbörsch, A. Umbach, D. Trommer, G. G. Mekonnen, "70 GHz Long-Wavelength Photodetector," Proceedings 23th European Conference on Optical Communication (ECOC 1997), September 22-25, 1997, Edinburgh, United Kingdom, pages: 25-28.

[44] H.-G. Bach, A. Beling, G. G. Mekonnen, R. Kunkel, D. Schmidt, W. Ebert, A. Seeger, M. Stollberg, and W. Schlaak, "InP-Based Waveguide-Integrated Photodetector with 100 GHz Bandwidth," IEEE

J. Selected Topics Quantum Electron., vol. 10, no.4, pages: 668-672, July/August 2004.

[45] M. J. N. Sibley and J. Bellon, "Transit-Time Limitations in p-i-n Photodiodes," Microwave and Optical Technology Letters, vol. 26, no. 5, September 2000, pages: 282-286.

[46] F. Effenberger, A. M. Joshi, "Ultrafast, Dual Depletion Region, InGaAs/InP p-i-n Detector, "J. Lightwave Technol, Vol. 14, No. 8, August 1996, pages: 1859-1864.

[47] "Taschenbuch der Physik," Herausgeber: H. Stöcker, Verlag Harri Deutsch, 1994.

[48] K. J. Ebeling, "Integrierte Optoelektronik," Springer Verlag, 1992.

[49] Photon Design, 34 Leopold St, Oxford, OX4 1TW, United Kingdom (www.photond.com/home.htm).

[50] A. S. Sudbø, "Numerically Stable Formulation of the Transverse Resonance Method for Vector Mode-Filed Calculations in Dielectric Waveguides," IEEE Photon. Techn. Letters, vol.5, no.3, March 1993, pages: 342-344.

[51] HP 8510XF Network Analyser Systems Operating and Service Manual, Hewlett-Packard Company Santa Rosa Systems Division 1400 Fountaingrove Parkway Santa Rosa, CA 95403-1799, U.S.A., March 10, 1998.

[52] A. Stöhr, R. Heinzelmann, A. Malcoci, and D. Jäger, "Optical Heterodyne Millimetre-Wave Generation using 1.55 μm Traveling-Wave Photodetectors," IEEE Trans. on Microwave Theory and Techniques, vol. 49, no. 10, October 2001, pages: 1926-1933.

[53] V. M. Hietala and K. S. Champlin, "Measurement of the Microwave Properties of Micron-Sized Coplanar Tranmission Lines," Journal of

Electromagnetic Waves and Applications, Vol.5, No.4/5, 1991, pages: 439-452.

[54] P. A. Rizzi, "Microwave Engineering Passive Circuits," Prentice-Hall, 1988.

[55] M. Y. Frankel, S. Gupta, J. A. Valdmanis, and G. A. Mourou, "Terahertz Attenuation and Dispersion Characteristics of Coplanar Transmission Lines," IEEE Trans. on Microwave Theory and Techniques, vol. 39, no. 6, June 1991, pages: 910-916.

[56] S. S. Bedair, I. Wolff, "Fast, Accurate and Simple Approximate Analytic Formulas for Calculating the Parameters of Supported Coplanar Waveguides for (M)MIC's," IEEE Trans. on Microwave Theory and Techniques, vol. 40, no. 1, January 1992, pages: 41-48.

[57] TXLine 2001, Applied Wave Research Inc., 1960 E. Grand Avenue, Suite 430, El Segundo, CA 90245, USA (http://web.appwave.com/).

[58] I. N. Bronstein, K. A. Semendjajew, G. Musiol, H. Mühlig, "Taschenbuch der Mathematik," Verlag Harri Deutsch, 1995.

[59] K. C. Gupta, R. Ramesh, I. Bahl, P. Bhartia, "Microstrip Lines and Slotlines," Artech House, 1996.

[60] H. -C. Chiu, M. -J. Hwu, S. -C. Yang, and Y. -J. Chan, "Enhanced Power Performance of Enhancement-Mode Al0:5Ga0:5As/In0:15Ga0:85As pHEMTs Using a Low-k BCB Passivation," IEEE Electron Device Lett., Vol. 23, No. 5, May 2002, pages: 243-245.

[61] M. J. W. Rodwell, S. T. Allen, R. Y. Yu, M. G. Case, U. Bhattacharya, M Reddy, E. Carman, M. Kamegawa, Y Konishi, J. Pusl, and R Pullela, "Active and Nonlinear Wave Propagation Devices in Ultrafast Electronics and Optoelectronics," Proc. of the IEEE, vol. 82, no. 7, July 1994, pages: 1037-1059.

[62] R. Kremer, S. Redlich, L. Brings, and D. Jäger, "Optically Controlled Coplanar Transmission Lines for Microwave Signal Processing," IEEE Trans. on Microwave Theory and Techniques, vol. 43, no. 9, September 1995, pages: 2408-2413.

[63] R. Deri, N. Yasuoka, M. Mkiuchi, O. Wada, A. Kuramata, H. Hamaguchi, R. J. Hawkins, "Integrated waveguide/photodiodes using vertical impedance matching," Appl. Phys. Lett., Vol. 56, No. 18, 30 April 1990, pages: 1737-1739.

[64] R. J. Deri, W. Döldissen, R. J. Hawkins, R. Bhat, J. B. D. Soole, L. M. Schiavone, M. Seto, N. Seto, N. Andreadakis, Y. Silberberg, and M. A. Koza, "Efficient vertical coupling of photodiodes to InGaAsP rib waveguides," Appl. Phys. Lett., Vol. 58, No. 24, 17 June 1991, pages: 2749-2751.

[65] S. Adachi, "GaAs, AlAs and AlGaAs: Material parameters for use in research and device applications," Journal of Applied Physics, Vol. 58, No. 3, August 1985, pages: R1-R29.

[66] J.-P. Weber, "Optimization of the Carrier-Induced Effective Index Change in InGaAsP Waveguides-Application to Tunable Bragg Filters," IEEE Journal of Quantum Electronics, Vol. 30, No. 8, August 1994, pages: 1801-1816.

[67] L. B. Soldana and E. C. M. Pennings, "Optical Multi-mode Interference Devices based on Self- Imaging: Principles and Applications," J. Lightwave Technol., Vol. 13, No.4, April 1995, pages: 615-627.

[68] Ansoft, 225 West Station Square Drive, Suite 200, Pittsburgh, PA 15219, USA (http://www.ansoft.com/).

[69] D. Trommer, D. Schmidt, A. Umbach, R. Steingrüber, W. Ebert, G. Unterbörsch, "Ultrafast, High-Power Waveguide Fed Photodetector with Integrated Spot Size Converter," Proc. 12th Conf. on In-

dium Phosphide and Related Materials (IPRM 2000), Williamsburg, VA, USA, WA2.6, pp. 462 - 465.

[70] N. R. Erickson, "A Fast and Sensitive Submillimeter Waveguide Power Meter," Proceedings of the Tenth International Space Terahertz Technology Symposium, University of Virginia, Charlottesville, Virginia, USA, March 1999, pages: 501-507.

[71] R. Kaiser, Dissertation, Fachbereich Physik, Technische Universität Berlin, Germany, 1991.

[72] A. M. Mangan, S. P. Voinigescu, M. Yang, and M. Tazlauanu, "De-Embedding Transmission Line Measurements for Accurate Modeling of IC Designs," IEEE Trans. Electron. Devices, VOL. 53, NO. 2, February 2006, pages: 235-241.

[73] K. Iiyama, J. Ashida, A. Takemoto, S. Takamiya, "Equivalent Circuit Model of InAsAs/InGaAs/InP Heterostructure Metal-Semiconductor-Metal Photodetectors," IEICE Trans. Electron., Vol. E86-C, No. 11, November 2003, pages: 2278-2282.

[74] P. D. Hale, T. S. Clement, K. J. Coakley, C. M. Wang, D. C. DeGroot, and A. P. Verdoni, "Estimating magnitude and phase response of a 50 GHz sampling oscilloscope using the 'nose-to-nose' method," in 55th ARFTG Conf. Dig., June 2000, pages: 335 - 342.

[75] A. Beling, "PIN Photodiode Modules for 80 Gbit/s and Beyond," Tech. Digest Optical Fiber Commun. (OFC 2006), Anaheim, CA, USA, March 05-10, 2006, paper OFI1.

[76] A. Beling, H.-G. Bach, G. G. Mekonnen, R. Kunkel, and D. Schmidt, "Miniaturized Waveguide-Integrated p-i-n Photodetector With 120-GHz Bandwidth and High Responsivity," IEEE Photonics Technology Letters, Vol. 17, No. 10, October 2005, pages: 2152-2154.

[77] G. G. Mekonnen, H.-G. Bach, A. Beling, D. Schmidt, A. Seeger , and M. Stollberg, "High-frequency electrical measurement and parameter extraction of InP-based photodetectors up to 100 GHz," Proceedings 33rd European Microwave Conference (EuMC 2003), October 7-9, 2003, Munich, Germany, vol. 3, pages: 1397-1399.

[78] A. Beling, H.-G. Bach, G. G. Mekonnen, T. Eckhardt, R. Kunkel, D. Schmidt, and C. Schubert, "Highly Efficient PIN Photodetector Module for 80 Gbit/s and Beyond," Tech. Digest Optical Fiber Commun. (OFC 2005) , Anaheim, CA, USA, March 06-11, 2005, paper OFM1.

[79] A. Beling, H.-G. Bach, G. G. Mekonnen, T. Eckhardt, R. Kunkel, G. Jacumeit, M. Kroh, and J. Berger, "Fully Packaged InP-based Photodetector for 80/85 Gbit/s RZ Systems," Proceedings 29th European Conference on Optical Communication (ECOC 2003), September 21-25, 2003, Rimini, Italy, vol.6, pp. 82-83.

[80] J. Berger, Q. Le, A. Wietfeld, S. Ferber, L. Grüner-Nielsen, B. Schmauss, H. G. Weber,"160 Gbit/s Transmission over Dispersion Managed Fibre Set," Proceedings 29th European Conference on Optical Communication (ECOC 2003), September 21-25, 2003, Rimini, Italy, vol.1, pp. 56-57.

[81] H.-G. Unger, "Elektromagnetische Wellen auf Leitungen," Hüthig Verlag Heidelberg, 1986.

A. List of publications

A. Beling, H.-G. Bach, G. G. Mekonnen, R. Kunkel, and D. Schmidt, "High-Speed Miniaturized Photodiodes and Parallel-fed Traveling Wave Photodetector based on InP," IEEE Journal of Selected Topics in Quantum Electronics, accepted for publication in 2007.

A. Beling, "PIN Photodiode Modules for 80 Gbit/s and Beyond," Tech. Digest Optical Fiber Commun. (OFC 2006), March 05-10, 2006, Anaheim, CA, USA, paper OFI1 (invited).

A. Beling, "InP-Based 1.55 mm Waveguide-Integrated Photodetectors for High-Speed Applications," Proc. SPIE, Vol. 6123, Photonics West 2006, January 21-26, 2006, San Jose, CA, USA (invited).

A. Beling, H.-G. Bach, G. G. Mekonnen, R. Kunkel, and D. Schmidt, "Miniaturized Waveguide-Integrated p-i-n Photodetector With 120-GHz Bandwidth and High Responsivity," IEEE Photonics Technology Letters, Vol. 17, No. 10, October 2005, pp. 2152-2154.

A. Beling, H.-G. Bach, R. Kunkel, G. G. Mekonnen, and D. Schmidt, "InP-Based $1.55\,\mu m$ High-Speed Photodetectors for 80 Gbit/s Systems and Beyond," Conference Proceedings 7th International Conference on Transparent Optical Networks (ICTON 2005), July 03-07, 2005, Barcelona, Spain, vol. 1, pp. 303-308 (invited).

A. Beling, H.-G. Bach, G. G. Mekonnen, T. Eckhardt, R. Kunkel, D. Schmidt, and C. Schubert, "Highly Efficient PIN Photodetector Module for 80 Gbit/s and Beyond," Tech. Digest Optical Fiber Commun. (OFC 2005), March 06-11, 2005, Anaheim, CA, USA, paper OFM1.

H. -G. Bach, A. Beling, G. G. Mekonnen, R. Kunkel, D. Schmidt, W. Ebert, A. Seeger, M. Stollberg, and W. Schlaak: "InP-Based Waveguide-Integrated Photodetector With

100-GHz Bandwidth," IEEE Journal of Selected Topics in Quantum Electronics, vol. 10, No. 4, July/August 2004, pp. 668-672.

D. O. Caplan, J. C. Gottschalk, R. J. Murphy, N. W. Spellmeyer, A. Beling, and M. L. Stevens, "Performance of high-rate high-sensitivity optical communications with forward error correction coding," Proceedings Conference on Lasers and Electro Optics (CLEO 2004), May 16-21, 2004, San Francisco, CA, USA, paper CPDD9.

A. Beling, H.-G. Bach, D. Schmidt, G. G. Mekonnen, T. Eckhardt, R. Kunkel, W. Ebert, A. Seeger, M. Stollberg, and W. Schlaak, "InP-Based Waveguide Integrated Photodetectors for High-Speed Optical Communication Systems," Proceedings Third Joint Symposium on Opto- and Microelectronic Devices and Circuits (SODC 2004), March 21-26, 2004, Wuhan, China, pp. 11-14 (invited).

A. Beling, H.-G. Bach, G. G. Mekonnen, R. Kunkel, D. Schmidt, R. Gibis, W. Ebert, A. Seeger, M. Stollberg, and W. Schlaak, "Monolithically Integrated Balanced Photoreceiver OEIC Comprising a Distributed Amplifier for 40 Gbit/s Applications," Tech. Digest Optical Fiber Commun. (OFC 2004), February 22-27, 2004, Los Angeles, CA, USA, paper TuM5.

G. G. Mekonnen, H.-G. Bach, A. Beling, D. Schmidt, A. Seeger , and M. Stollberg, "High-frequency electrical measurement and parameter extraction of InP-based photodetectors up to 100 GHz," Proceedings 33rd European Microwave Conference (EuMC 2003), October 7-9, 2003, Munich, Germany, vol. 3, pp. 1397-1399.

A. Beling, H.-G. Bach, G. G. Mekonnen, T. Eckhardt, R. Kunkel, G. Jacumeit, M. Kroh, and J. Berger, "Fully Packaged InP-based Photodetector for 80/85 Gbit/s RZ Systems," Proceedings 29th European Conference on Optical Communication (ECOC 2003), September 21-25, 2003, Rimini, Italy, vol.6, pp. 82-83.

A. Beling, H.-G. Bach, D. Schmidt, G.G. Mekonnen, R. Ludwig, S. Ferber, C. Schubert, C. Boerner, B. Schmauss, J. Berger, C. Schmidt, U. Troppenz and H.G . Weber,

"Monolithically integrated balanced photodetector and its application in OTDM 160 Gbit/s DPSK transmission," Electron. Lett., 2003, 39 (16), pp. 1204-1205.

A. Beling, H.-G. Bach, D. Schmidt, G. G.Mekonnen, M. Rohde, L. Molle, H. Ehlers, A. Umbach "High-Speed Balanced Photodetector Module with 20dB Broadband Common-Mode Rejection Ratio," Tech. Digest Optical Fiber Commun. (OFC 2003), March 23-28, 2003, Atlanta, GA, USA, vol. 1, paper WF4, pp. 339-340.

A. Beling, D. Schmidt, H.-G. Bach, G. G. Mekonnen, R. Ziegler, V. Eisner, M. Stollberg, G. Jacumeit, E. Gottwald, C.-J. Weiske, A. Umbach: "High power 1550 nm twin-photodetector modules with 45 GHz bandwidth based on InP," Tech. Digest Optical Fiber Commun. (OFC 2002), March 17-22, 2002, Anaheim, CA, USA, paper WN4, pp. 274-275.

B. Danksagung

Für die Betreuung meiner Arbeit und die abschließende Gutachtertätigkeit möchte ich Herrn Prof. Dr.-Ing. Klaus Petermann vom Institut für Hochfrequenztechnik der Technischen Universität Berlin sehr herzlich danken.
Herrn Prof. Dr. Dieter Jäger vom Zentrum für Halbleitertechnik und Optoelektronik der Universität Duisburg-Essen sei für die Übernahme des zweiten Gutachtens vielmals gedankt.
Die vorliegende Arbeit entstand im Rahmen meiner Tätigkeit als wissenschaftlicher Mitarbeiter am Fraunhofer-Institut für Nachrichtentechnik, Heinrich-Hertz-Institut (HHI), Berlin. Den Mitarbeitern der Detektorgruppe sowie den Bewohnern der dritten Etage sei für jegliche Hilfe und das angenehme Arbeitsklima gedankt. Ich danke Herrn Prof. Dr. Hans-Joachim Grallert, Dr. Herbert Venghaus und Dr. Martin Schell, die die Durchführung dieser Arbeit am HHI ermöglichten. Insbesondere bin ich all jenen zu Dank verpflichtet, die zum Gelingen dieser Arbeit beigetragen haben:
An erster Stelle sei Herrn Dr.-Ing. Heinz-Gunter Bach für die Themenstellung meiner Dissertation, die zahllosen Anregungen, hilfreichen Tips und ausführlichen Diskussionen besonders gedankt,
Herrn Giorgis Gebre Mekonnen für die Durchführung der S-Parameter Messungen und die hilfreiche Unterstützung bei der Parameter-Extraktion, Frau Angela Seeger, Ralf Steingrüber, Tom Gaertner und ganz besonders Detlef Schmidt, der die Prozeßentwicklung und die Herstellung der Detektoren durchführte, Dr.-Ing. Reinhard Kunkel für die Umsetzung der Layouts am CAD, den Herren Wolfgang Rehbein, Dr. Bernd Hüttl, Dr. Colja Schubert und Dr. Carsten Schmidt-Langhorst für das Bereitstellen von Meßgeräten und die Unterstützung bei der Durchführung der Systemexperimente, den Herren Daniel Tomecki, Özkan Karpuzi, Matthias Deuser, Carsten Patzelt und Ruiyong Zhang möchte ich für die fruchtbaren Fachgespräche sowie die vielfältige Unterstützung bei den diversen Messaufgaben danken, den Mitarbeitern der AVT und insbesondere Thomas Eckhardt danke ich für die Herstellung des TWPD-Moduls.
Zoë Cartledge, Christian Gläser und insbesondere Trish Gläser sei vielmals für das zügige Korrekturlesen dieser Arbeit gedankt.
Ich danke ganz besonders David und Minou.